Master Thesis on the Subject

Towards Dark-Field Spectroscopy for Measuring Photocharging of Single Nanoparticles

Alexandra Faber

Supervisor: Dr. Wouter Koopman and Prof. Dr. Matias Bargheer
First Reviewer: Dr. Wouter Koopman
Second Reviewer: Prof. Dr. Svetlana Santer

Ultrafast Dynamics in Condensed Matter
Institute of Physics and Astronomy
Faculty of Sciences
University of Potsdam

Potsdam, July 09, 2026

Abstract

Nobel metal nanostructures show great potential for photocatalytical applications due to their broadband plasmonic absorption across the visible spectrum. Chemical reactions taking place at surfaces can be accelerated by several effects, including charge transfer and local heating. The accumulation of charges on the particle during a reaction process, is expected to have a large influence on the charge transfer process. Accordingly, this work investigates charge transfer processes and the effect of photocharging on single nanoparticles.
An experimental setup to reliably record dark-field scattering spectra of single nanoparticles was established and employed in experimental studies. The measured particles were additionally verified as single gold nanorods (GNR) using electron microscopy. The influence of various charge transfer processes and electrostatic effects on single gold particles was investigated in separate experiments. Throughout, the energy position of the longitudinal surface plasmon resonance (LSPR) served as reference parameters, since it is sensitive to electrostatic interactions with the environment. Additionally, its linewidth was utilized as a comparison criteria, as it provides information on changes of the plasmon damping rate.
GNRs were measured on substrates with different electrical conductivities in order to detect direct charge transfer between the GNRs and the substrate. A significant broadening of the plasmon resonance was observed especially GaN, suggesting increased damping due to direct charge transfer to the substrate. Furthermore, the influence of an altered electrostatic environment on the optical response of GNRs was investigated by varying the pH value of the surrounding solution. An decrease in the pH value, which corresponds to an increasing concentration of H^+ ions, led to a slight blue shift and a broadening of the longitudinal plasmon resonance. However, both effects did not occur consistently throughout all the recordings. Lastly, in situ measurements of light-induced charging of gold nanoparticles were conducted. A resonance shift resulting from the charge accumulation, which was previously observed in ensemble measurements [1], was reproduced using single GNRs for the first time. Additionally, the behaviour of the resonance width was investigated and can be related to two predominant, competing and opposing effects. The results presented in this work provide new insights into the influence of photocharging on the optical properties of individual gold nanorods and highlight their potential for photocatalytic applications. However, further investigations are required to fully elucidate the underlying mechanisms.

Zusammenfassung

Metallische Nanostrukturen besitzen aufgrund ihrer breitbandigen plasmonischen Absorption im sichtbaren Spektralbereich ein großes Potenzial für photokatalytische Anwendungen. Chemische Reaktionen an ihrer Oberfläche können durch verschiedene Mechanismen wie Ladungstransferprozesse und lokales Erhitzen beschleunigt werden. Es wird erwartet, dass eine Anreicherung von Ladungen auf den Nanopartikeln während des Reaktionsprozesses einen positiven Einfluss auf den Ladungstransfer zwischen den Partikeln und ihrer Umgebung hat. Ziel dieser Arbeit war es daher, Ladungstransferprozesse und den Effekt der lichtinduzierten Aufladung an einzelnen Goldnanorods zu untersuchen.
Es wurde dafür ein experimenteller Aufbau entwickelt, mit dem die Dunkelfeld-Streuspektren einzelner Nanopartikel zuverlässig gemessen werden konnten. Zusätzlich wurden die untersuchten Partikel mittels Elektronenmikroskopie als einzelne Goldnanorods (GNR) verifiziert. Der Einfluss verschiedener Ladungstransferprozesse und elektrostatischer Effekte auf einzelne Goldpartikel wurde in separaten Experimenten untersucht. Als Vergleichsparameter diente dabei zum einen die energetische Lage der longitudinalen Oberflächenplasmonenresonanz, welche sensibel auf elektrostatische Wechselwirkungen mit der Umgebung reagiert. Zum anderen wurde deren Linienbreite beobachtet, da sie Informationen über Änderungen der Plasmonendämpfung liefert.
Zunächst wurden GNRs auf Substraten mit unterschiedlichen elektrischen Leitfähigkeiten gemessen, um Hinweise auf direkten Ladungstrasfer zu detektieren. Für leitfähigere Substrate, insbesondere für GaN, wurde eine deutliche Verbreiterung der Plasmonenresonanz beobachtet, was auf eine erhöhte Dämpfung durch direkte Ladungsübertragungsprozesse von den Partikeln auf das Substrat hindeutet. Des Weiteren wurde der Einfluss einer veränderten elektrostatische Umgebung auf die optische Reaktion der GNRs untersucht, indem der pH-Wert der umgebenden Lösung verändert wurde. Beim Absenken des pH-Wertes, wobei die Anzahl der H^+ ansteigt, konnte eine leichte Blau-Verschiebung und Verbreiterung der longitudinalen Plasmonenresonanz festgestellt werden. Allerdings traten beide Effekte nicht konsistent in aller aufgenommen Messungen auf. Anschließend wurden in situ Messungen zur lichtinduzierten Aufladung von einzelnen Goldnanopartikeln durchgeführt. Dabei konnte die für Ensemblemessungen nachgewiesene Resonanzverschiebungen infolge der Anreicherung von negativen Ladungen auf dem Partikel [1] erstmals an einzelnen GNRs reproduziert. Zusätzlich wurde das Verhalten der Resonanzbreite untersucht werden und dabei zwei vorherrschende, miteinander konkurrierende und entgegen gesetzte Effekte beobachtet. Die in dieser Arbeit vorgestellten Ergebnisse zeigen liefern neue Erkenntnisse zum Einfluss der Photoaufladung auf die optischen Eigenschaften einzelner Goldnanorods und verdeutlichen deren Potenzial für photokatalytische Anwendungen. Zur vollständigen Aufklärung der zugrunde liegenden Mechanismen sind jedoch weitere Untersuchungen erforderlich.

Contents

1 Introduction

Anthropogenic climate change is one of today's major global challenges and is strongly driven by greenhouse gas emissions associated with energy production [2]. Consequently, the development of sustainable technologies for harvesting and converting solar energy has become an important research objective. Nobel metal nanostructures have emerged as promising candidates for such applications due to their broadband plasmonic absorption across the visible spectrum and their coupling with adsorbed molecules or adjacent semiconductor materials [3, 4]. These properties can be exploited to enhance and drive chemical reactions, enabling applications such as renewable electricity, and photocatalysis for solar fuel generation and artificial photosynthesis [3]. The acceleration level of chemical reactions taking place at the surface of GNRs depends on several effects, including charge transfer and local heating [5]. Additionally, accumulated charges on the surface of the GNR are expected to have positive influence on charge transfer between the particle and attached materials. Due to an altered electrostatic interaction with the environment caused by charging the bandstructure of the GNRs can be shifted and consequently, tuned to match the energy levels of an adjacent material [1]. A previous study regarding this phenomenon has been only conducted on ensembles of particles [1]. However, ensemble measurements average over nanoparticles with different sizes, shapes, and local environments, leading to inhomogeneous spectral broadening resulting in a loss of information regarding the behaviour of individual particles [6]. Single particle spectroscopy overcomes these limitations and enables access to the optical properties of individual nanoparticles [7]. In particular, the localised surface plasmon resonance (LSPR) is sensitive to changes in the electrical near field environment of the particle. Its linewidth provides information regarding the decay ingrate of the plasmon determined by the number of contributing decay channels. Since interfacial charge transfer processes can contribute to plasmon damping [8], single particle spectroscopy offers a promising approach for investigating charge transfer phenomena that are difficult to disentangle in ensemble measurements.

The primary objective of this work is the development of an experimental optical setup capable of reliably measuring the scattering spectra of single nanoparticles. This setup was then employed to investigate various charge transfer related processes in plasmonic systems. First investigations were conducted regarding the observation of chemical interface damping (CID) as it may indicate direct charge transfer between nanoparticles an the substrate [8]. The aim was to determine whether the established setup is sensitive enough to reveal differences in the optical properties of nanoparticles when employing various substrates. Promising substrates were investigated for which direct charge transfer with GNRs is likely to occur, using a glass substrate as reference.

When GNRs are dispersed in solution, an electrical double layer forms around the particles [9]. The optical properties of nanostructures are not only sensitive to charge transfer but also to variations of the particle's electrostatic near field environment. It was therefore aimed to understand to which extend the optical response of GNRs can be influenced. In order to gain these insights, the amount of H^+ ions in solution was altered via varying

its pH value.
In addition, photo-induced charge accumulation was investigated in situ. It was aimed to reproduce the mentioned ensemble observations [1] at the single-particle level. Particular attention was given to the evolution of linewidth of the LSPR, as it provides insights into plasmon damping mechanisms, which cannot be determined using ensemble of particles, in order to achieve a better understanding of the underlying processes.

2 Theoretical Background

We introduce the physical concepts important for the understanding of the experiments and results. We start with the derivation of the general ideas and quantities, which apply in all of the conducted experiments. We start in Section 2.1 with the explanation of the dielectric function of metals following the ideas given by Novotny and Hecht in their book on nano-optics [10]. The dielectric function describes how matter reacts to an external electric field regarding its electronic properties. This physical quantity is important for describing the optical properties of a material as shown in Section 2.2. The most important expressions for the understanding of localised surface plasmons (LSP) are derived in the picture of a sphere in an external electric field. The argumentation roughly reproduces the ideas of Maier's book about plasmonics [11]. Since the measurements were exclusively performed on gold nanorods (GNR) the expressions valid for spheres are going to be adapted to nanorods in Section 2.3. Rods can be treated as ellipsoids with a long axis a and two shorter axis $b = c$ with sufficient accuracy. In a sphere all axis are assumed to be of the same lengths, hence the equations need adjusting for the more general case of a rod.
Central to this work is the investigation of transfer of charges between a GNR and its environment. In Section 2.4 and 2.5 two possible charge transfer processes are introduced. The former focusses on chemical interface damping (CID) including plasmon-induced direct charge transfer (PICT). There, plasmon decays by inserting excited charge carriers directly in an attached semiconductor or other adjacent materials [8]. The latter describes electron transfer to the nanoparticle and especially their accumulating during irradiation with a laser.
The last section in this chapter addresses the used measurement techniques and their operating principles. Dark-field microscopy is presented in Section 2.6.1. This optical technique was applied to record the scattering spectra of single particles. In Section 2.6.2 scanning electron microscopy (SEM) is introduced. Because of the limited resolution of optical microscopy due to the wavelength range of visible light, the shape of the nanoparticles is not visible in dark-field images. Furthermore, particles located close together cannot be distinguished. To get additional information regarding these, SEM techniques were used.

2.1 Dielectric Function

The dielectric function also known as permittivity describes the electronic response function of a material to an external electric field. In other words, it can be used to determine the electronic properties of a material. In metals we can distinguish two different situations for electrons. On one hand there are the quasi free conduction electrons, which can move freely as an electron cloud through the metal. On the other hand there are core electrons of the lower energy levels, which are bound stronger to the core of the atoms.
An external electric field $\vec{E}$ leads to a displacement of the electrons. We assume only

conduction electrons get displaced with $\vec{r}$ as their displacement. Because of the resulting charge separation in the metal a dipole moment $\vec{p} = e\vec{r}$ is induced for every electron with the elementary charge e. When considering the cumulative effect of all electrons a macroscopic dipole moment per unit volume $\vec{P}$, also known as polarisation, can be found as

$$\vec{P} = n\vec{p}. \tag{2.1}$$

Here, n is the number of free electrons per unit volume [10]. This is valid when assuming that all electrons have the same dipole moment [12]. In the case of a linear response of the material, the dipole moment can also be described via the relation between the electric susceptibility χ_e, the permittivity of the vacuum ε_0 and the external electric field $\vec{E}$ [10, 13] as

$$\vec{P} = \varepsilon_0 \chi_e \vec{E}. \tag{2.2}$$

The displacement leads not only to a dipole moment but also to an electric displacement field $\vec{D}$ which is defined as the sum of the external electric field and the polarisation [10, 12],

$$\vec{D}(\vec{r}, t) = \varepsilon_0 \vec{E}(\vec{r}, t) + \vec{P}(\vec{r}, t). \tag{2.3}$$

From the constitutive relations, which describe how the material behaves in an external field, we can find an additional expression for the amplitude of $\vec{D}(\vec{r}, t)$ of a linear medium to be

$$\vec{D}(\vec{k}, \omega) = \varepsilon_0 \varepsilon(\vec{k}, \omega) \vec{E}(\vec{k}, \omega). \tag{2.4}$$

Here, the permittivity of the matter ε is related with $\vec{E}$ [10]. Via comparing Equation 2.3 and 2.4 an expression for the ε can be derived

$$\vec{D}(\omega) = \varepsilon_0 \vec{E}(\omega) + \vec{P}(\omega) = \varepsilon_0 \varepsilon(\omega) \vec{E}(\omega). \tag{2.5}$$

ε has a general form of [13]

$$\varepsilon(\omega) = 1 + \chi_e(\omega) = 1 + \chi_{Drude}(\omega) + \chi_{int}(\omega). \tag{2.6}$$

Here, $\chi_e(\omega)$ describes the combined answer of all electrons. To determine $\varepsilon(\omega)$, $\chi_e(\omega)$ has to be split into two terms. The former, χ_{Drude}, applies for quasi free electrons, which can be described by the Drude-Sommerfeld model and are therefore also known as Drude electrons. The latter, $\chi_{int}(\omega)$, refers to the core electrons, which show interband transitions when absorbing energy of $\vec{E}$. Because of their various properties, both kind of electrons react differently to an incoming electric field.
First, we consider the Drude electrons and their permittivity ε_{Drude}. Since we are going to illuminate the metal particles with light, an electromagnetic wave, in later experiments $\vec{E}$ is not static but supposed to oscillate in time t with the frequency ω and the amplitude $\vec{E}_0$. For the Drude electrons we can use the classical equation of motion for the drift velocity of free charge carriers given as [14, 15]

$$m_e \frac{\partial^2 \vec{r}}{\partial t^2} + m_e \Gamma \frac{\partial \vec{r}}{\partial t} = \vec{E}_0 e^{-i\omega t}. \tag{2.7}$$

Here, m_e is the mass of the electrons and Γ a is damping constant. The damping appears via inelastic scattering of the electrons. Therefore, Γ depends on the Fermi velocity v_F and the mean free path of the electrons l. This is the average distance an electron can travel without scattering events [12]. Γ given as

$$\Gamma = \frac{v_F}{l}. \tag{2.8}$$

To determine an expression for ε_{Drude} Equation 2.7 has to be solved. We chose $\vec{r}(t) = \vec{r}_0 e^{-i\omega t}$ as ansatz and by inserting it in Equation 2.2 we get the contribution of ε_{Drude} [10]

$$\varepsilon_{Drude} = 1 - \frac{\omega_p^2}{\omega^2 + i\Gamma\omega}. \tag{2.9}$$

Here, ω_p denotes the plasma frequency, which is the resonance frequency of a bulk plasma with $\omega_p = \sqrt{ne^2/(m_e\varepsilon_0)}$. By rearranging Equation 2.9 the expressions for the real and the imaginary part of ε_{Drude} can be found to be

$$\mathrm{Re}\{\varepsilon_{Drude}\}(\omega) = 1 - \frac{\omega_p^2}{\omega^2 + \Gamma^2}, \tag{2.10a}$$

$$\mathrm{Im}\{\varepsilon_{Drude}\}(\omega) = \frac{\omega_p^2\Gamma}{\omega(\omega^2 + \Gamma^2)}. \tag{2.10b}$$

The contribution of the core electrons is derived analogously to those of the Drude electrons. As before, we start with the equation of motion given as

$$m\frac{\partial^2\vec{r}}{\partial t^2} + m\gamma\frac{\partial\vec{r}}{\partial t} + s\vec{r} = \vec{E}_0 e^{-i\omega t}. \tag{2.11}$$

γ is the damping constant and $m \neq m_e$ is the effective mass of the bound electrons. Damping appears here mainly via radiative processes. The main difference, however, is the additional restoring force described by $s\vec{r}$. This is due to the potential of the atomic nuclei, which attracts the electrons and causes a force opposite to their displacement. In the picture of a ball on a spring, s describes the spring constant of the process. The permittivity is determined in the same way as for the contribution of the Drude electrons and can be found as [10]

$$\varepsilon_{int}(\omega) = 1 + \frac{\tilde{\omega}_p^2}{(\omega_0^2 - \omega^2) - i\gamma\omega}. \tag{2.12}$$

Here, $\tilde{\omega}_p$ is defined similar to ω_p in the Drude electron picture as $\tilde{\omega}_p = \sqrt{\tilde{n}e^2/(m_e\varepsilon_0)}$, but it has another physical interpretation. $\tilde{n}$ denotes the density of the bound electrons and ω_0 is given as $\omega_0 = \sqrt{s/m}$. Equation 2.12 can also be divided in a real and an imaginary part [10], which results in

$$\mathrm{Re}\{\varepsilon_{int}\}(\omega) = 1 + \frac{\tilde{\omega}_p^2(\omega_0^2 - \omega^2)}{(\omega_0^2 - \omega^2) + \gamma^2\omega^2}, \tag{2.13a}$$

$$\mathrm{Im}\{\varepsilon_{int}\}(\omega) = \frac{\gamma\tilde{\omega}_p^2\omega}{(\omega_0^2 - \omega^2) + \gamma^2\omega^2}. \tag{2.13b}$$

This describes the behaviour of a single interband transition. For determine the permittivity of a real material numerous of these transitions have to be added [12].

2.2 Localised Surface Plasmon (LSP)

A plasmon is a resonant collective oscillation of conduction electrons inside a material and can only appear in matter with free carriers, such as metals. It can be excited by an external electric field, which exerts a force on the conduction electrons leading to a displacement of these with respect to the positively charged ion lattice. Due to a resulting restoring force an eigenfrequency can be determined for the system. When the frequency of the incoming electromagnetic wave matches the eigenfrequency of the electron system, a resonant behaviour is excited which is referred to as plasmon. Each individual electron carries only a small fraction of the energy of the plasmon. In the case of nanoparticles, the plasmon is restricted in all spacial dimensions and therefore referred to as localised [16]. A plasmon has a great impact on the electronic and optical properties of a nanoparticle and is highly sensitive to the permittivity of the environment and the shape and size of the particle.
We want to derive the optical properties of a nanoparticle represented by the scattering and absorption cross section utilizing the localised surface plasmon resonance (LSPR). Initially, we consider the most simple case of a spherical particle with the radius a in a homogenous electric field E_0. This is valid for particles much smaller than the wavelength of the incoming light as in this case the electromagnetic field can be assumed to be constant at all points of the volume of the particle (Figure 2.1). The derivation follows the argumentation of Maier in his book about plasmonics [11] and Stete in his dissertation on gold at the nanoscale [16].

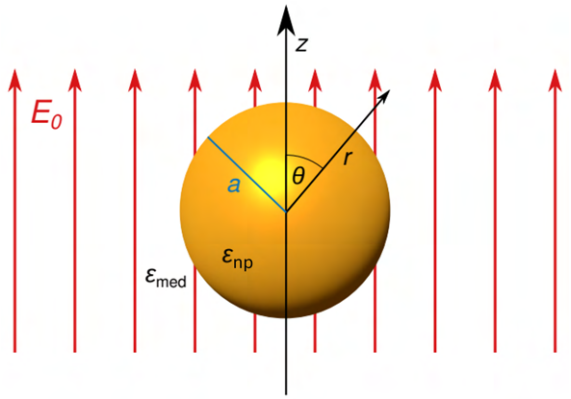

Figure 2.1: A spherical nanoparticle with radius a and a permittivity ε_{np} in an incoming electric field $\vec{E}_0$. The particle is located in the origin and surrounded by a medium with the permittivity ε_{med}.
This image was taken from Reference [16] and slightly adjusted.

To simplify the calculations the centre of the sphere is chosen to be located in the origin and the electric field $\vec{E}_0$ should point in z-direction. An illustration is shown in Figure 2.1. We separate the system in two different regions: (1) inside the sphere with $r < a$ and the permittivity ε_{np}, and (2) outside the sphere with $r > a$ and the permittivity of the surrounding medium ε_{med}. The electric field $\vec{E}$ depends on the electric potential Φ and is given as

$$\vec{E}_{1,2} = -\nabla\Phi_{1,2}. \tag{2.14}$$

At first, we consider only the spatial dependence and add the time evolution when the static electrical field is known. Therefore the Laplace equations for the potential inside

and outside the sphere are given by

$$\nabla^2\Phi_1 = 0, \tag{2.15a}$$
$$\nabla^2\Phi_2 = 0. \tag{2.15b}$$

In order to determine Φ_1 and Φ_2 the Laplace equation is converted into spherical coordinates which is convenient because of the spherical symmetry of the nanoparticle and can be written as

$$\frac{1}{r^2\sin\theta}\left[\sin\theta\frac{\partial}{\partial r}\left(r^2\frac{\partial}{\partial r}\right) + \frac{\partial}{\partial\theta}\left(\sin\theta\frac{\partial}{\partial\theta}\right) + \frac{1}{\sin\theta}\frac{\partial^2}{\partial\varphi^2}\right]\Phi(r,\theta,\varphi) = 0 \tag{2.16}$$

Here, r denotes the radial distance, θ the polar angle and φ the azimuth angle. Since the centre of the particle was chosen to align with the origin and due to the azimuthal symmetry of the system, the corresponding term in Equation 2.16 vanishes. General solutions for both regimes can then be found to be[16, 17]

$$\Phi_1 = \sum_{l=0}^{\infty}\left[A_l r^l + B_l r^{-(l+1)}\right]P_l(\cos\theta), \tag{2.17a}$$
$$\Phi_2 = \sum_{l=0}^{\infty}\left[C_l r^l + D_l r^{-(l+1)}\right]P_l(\cos\theta), \tag{2.17b}$$

with P_l the Legendre polynomials of the l-th order.
The coefficients A_l, B_l, C_l and D_l can be determine by considering the boundary conditions which arise from the design of the system. Four different conditions can be found.
1. There are no residual charges in the centre of the sphere therefore the potential has to be finite for $r \to 0$.
2. The influence of the nanosphere on the outer potential has to vanish in the far field limit.
3. and 4. At a metal interface, continuity is required for the tangential component of the electric field $\vec{E}$, as well as for the normal component of the electric displacement field $\vec{D} = \varepsilon\frac{\partial\Phi}{\partial r}$.
To summarise, they can be written as

$$1. \quad \lim_{r\to\infty}\Phi_1 = 0 \tag{2.18a}$$
$$2. \quad \lim_{r\to\infty}\Phi_2 = \Phi_0 = -E_0 r\cos\theta \tag{2.18b}$$
$$3. \quad \Phi_1|_{r=a} = \Phi_2|_{r=a} \tag{2.18c}$$
$$4. \quad \varepsilon_{np}\frac{\partial\Phi_1}{\partial r}\bigg|_{r=a} = \varepsilon_{med}\frac{\partial\Phi_2}{\partial r}\bigg|_{r=a}. \tag{2.18d}$$

We apply the boundary conditions one by one to derive the coefficients. From Equation 2.18a we know the second term in Equation 2.17a has to vanish because it would not diverge for $r \to 0$. This can be achieved for $B_l = 0$.
By applying Equation 2.18b on Equation 2.17b we get

$$D_l r^{-(l+1)} \xrightarrow{r\to\infty} 0$$
$$\sum_{l=0}^{\infty} C_l r^l P_l(\cos\theta)\big|_{r\to\infty} = \Phi_0 = -E_0 r\cos\theta \tag{2.19}$$

with Φ_0 as the potential uneffected by the nanosphere.
The general form of the Legendre polynomials is defined as

$$P_l(x) = \frac{1}{2^l(l!)}\frac{d^l}{dx^l}(x^2-1)^l \tag{2.20}$$

with $x = \cos\theta$ [17]. The Legendre polynomials form an orthonormal basis. Thus, every point can be described by exactly one combination of the basis vectors. The polynomial of the first order with $k = 1$ can be found to be $P_1(\cos\theta) = \cos\theta$. By inserting this in Equation 2.19 it follows that the expression for the far field limit can only be fulfilled for $l = 1$ due to the properties of an orthonormal basis. Thus, the polynomials for $k \neq 1$ have to vanish independently, which leads to

$$\begin{aligned} C_1 r^1 \cos\theta &= -E_0 r \cos\theta, \\ C_1 &= -E_0. \end{aligned} \tag{2.21}$$

Based on the first two boundary conditions, the potentials Φ_1 and Φ_2 can provisionally determined as

$$\Phi_1 = \sum_{l=0}^{\infty} A_l r^l P_l(\cos\theta), \tag{2.22a}$$

$$\Phi_2 = \Phi_0 + \sum_{l=0}^{\infty} D_l r^{-(l+1)} P_l(\cos\theta). \tag{2.22b}$$

The remaining coefficients A_l and D_l are going to be derived via the last two boundary conditions. Equation 2.22a and 2.22b can be implemented in the third boundary condition described by Equation 2.18c which leads to

$$\begin{aligned} &\frac{\partial}{\partial\theta}\sum_{l=0}^{\infty} A_l r^l P_l(\cos\theta)\bigg|_{r=a} = \frac{\partial}{\partial\theta}\left(\Phi_0 + \sum_{l=0}^{\infty} D_l r^{-(l+1)} P_l(\cos\theta)\right)\bigg|_{r=a} \\ \Rightarrow &\frac{\partial}{\partial\theta}\sum_{l=0}^{\infty}\left(A_l a^l - D_l a^{-(l+1)}\right) P_l(\cos\theta) = \frac{\partial}{\partial\theta}\Phi_0 = \frac{\partial}{\partial\theta}(-E_0 a\cos\theta). \end{aligned} \tag{2.23}$$

By using again the argument of the Legendre polynomials as an orthonormal basis with $P_1(\cos\theta) = \cos\theta$ different solutions can be found for $l \neq 0$ and $l = 0$

$$A_l a^l - D_l a^{-(l+1)} = 0 \quad \text{for } l \neq 0, \tag{2.24a}$$

$$A_1 - D_1 a^{-3} = -E_0 \quad \text{for } l = 0. \tag{2.24b}$$

Similarly, Equation 2.22a and 2.22b are also implemented in the fourth boundary condition described by Equation 2.18d leading to

$$\begin{aligned} &\varepsilon_{np}\frac{\partial}{\partial r}\sum_{l=0}^{\infty} A_l r^l P_l(\cos\theta)\bigg|_{r=a} = \varepsilon_{med}\frac{\partial}{\partial\theta}\left(\Phi_0 + \sum_{l=0}^{\infty} D_l r^{-(l+1)} P_l(\cos\theta)\right)\bigg|_{r=a} \\ \Rightarrow &\varepsilon_{np}\sum_{l=0}^{\infty} A_l a^{l-1} P_l(\cos\theta) = \varepsilon_{med}\left(-E_0\cos\theta + \sum_{l=0}^{\infty} D_l(l+1)a^{-(l+2)} P_l(\cos\theta)\right). \end{aligned} \tag{2.25}$$

The previous argument regarding the Legendre polynomials applies here as well and in analogy to the former presented step different results for $l \neq 0$ and $l = 0$ were obtained here too,

$$A_l a^{(l-1)} \cos\theta \varepsilon_{np} + D_l (l+1) a^{-(l+2)} \varepsilon_{med} = 0 \quad \text{for } l \neq 0, \tag{2.26a}$$

$$A_1 \varepsilon_{np} + 2 D_1 a^{-3} \varepsilon_{med} = -E_0 \varepsilon_{med} \quad \text{for } l = 0. \tag{2.26b}$$

This gives us a system of four equations which is solved in order to derive expressions for A_l, D_l, A_1 and D_1. By comparing Equation 2.24a and 2.26a it can be found, that both equations can only be satisfied simultaneously for $A_l = D_l = 0$. Instead for A_1 and D_1 solutions unequal to zero can be determined and result in

$$A_1 = -\frac{3\varepsilon_{med}}{\varepsilon_{np} + 2\varepsilon_{med}} E_0, \tag{2.27a}$$

$$D_1 = \frac{\varepsilon_{np} + \varepsilon_{med}}{\varepsilon_{np} + 2\varepsilon_{med}} E_0 a^3. \tag{2.27b}$$

By implementing these results for A and D in Equation 2.22a and 2.22b expressions for the potentials Φ_1 and Φ_2 can be obtained as

$$\Phi_1 = -E_0 r \cos\theta \frac{3\varepsilon_{med}}{\varepsilon_{np} + 2\varepsilon_{med}}, \tag{2.28a}$$

$$\Phi_2 = -E_0 r \cos\theta + E_0 a^3 \frac{\cos\theta}{r^2} \frac{\varepsilon_{np} + \varepsilon_{med}}{\varepsilon_{np} + 2\varepsilon_{med}}. \tag{2.28b}$$

The inner potential Φ_1 is similar to a potential uneffected by the particle. Meanwhile, the potential outside the nanosphere Φ_2 describes the superposition of an uneffected potential and the one of a dipole located in the origin [16, 6, 13]. It can be written as

$$\Phi_2 = \Phi_0 + \frac{p \cos\theta}{4\pi\varepsilon_0 r^2} \tag{2.29a}$$

$$= \Phi_0 + \frac{\vec{p} \cdot \vec{r}}{4\pi\varepsilon_0 r^3 \varepsilon_{med}}. \tag{2.29b}$$

$\vec{p}$ denotes an electric dipole moment with

$$\vec{p} = 4\pi\varepsilon_0 \varepsilon_{med} \vec{E_0} a^3 \frac{\varepsilon_{np} - \varepsilon_{med}}{\varepsilon_{np} + 2\varepsilon_{med}}. \tag{2.30}$$

Since the electric dipole is also defined as [13]

$$\vec{p} = \varepsilon_{med} \alpha \vec{E_0}, \tag{2.31}$$

we can obtain an expression for the polarizability α [16, 15]

$$\alpha = 4\pi\varepsilon_0 a^3 \frac{\varepsilon_{np} - \varepsilon_{med}}{\varepsilon_{np} + 2\varepsilon_{med}}. \tag{2.32}$$

The polarizability is highly relevant to determine the optical properties of the nanosphere especially regarding the resonance position and will be utilized for this purpose later in this chain of arguments. Before, we go back to the initial Equation 2.14. Via the derived

expressions for Φ_1 and Φ_2 in Equation 2.28a and 2.28b we obtain the electric field inside the nanosphere $\vec{E_1}$ and outside the particle $\vec{E_2}$ as

$$\vec{E_1} = \vec{E_0}\frac{3\varepsilon_{med}}{\varepsilon_{np} + 2\varepsilon_{med}}, \tag{2.33a}$$

$$\vec{E_2} = \vec{E_0} + \frac{\alpha}{4\pi\epsilon_0}\frac{3\hat{r}(\hat{r}\cdot\vec{E_0}) - \vec{E_0}}{r^3}. \tag{2.33b}$$

So far we have only considered the case of a static electric field $\vec{E}(\vec{r}) = \vec{E_0}(\vec{r})$. Since the nanosphere is supposed to be irradiated by light, which is an electromagnetic wave, the electric field has to oscillate with $\vec{E}(\vec{r},t) = \vec{E_0}(\vec{r})e^{i\omega t}$. Here, $\vec{E_0}$ denotes the amplitude of the field and ω the frequency. As we consider a particle much smaller than the wavelength of the incoming light, the particle can still be assumed to be in a homogenous electric field and dipole moments can be neglected. The permittivity of the nanosphere has the general form

$$\varepsilon_{np}(\omega) = \mathsf{Re}\{\varepsilon_{np}(\omega)\} + i\ \mathsf{Im}\{\varepsilon_{np}(\omega)\}. \tag{2.34}$$

It is an complex quantity as it was derived in Section 2.1. Additionally, it depends on the frequency of the incoming electric field. Therefore, the polarizability α is also frequency dependent and can show resonant behaviour. α becomes maximal when the denominator vanishes in Equation 2.32. For dielectric materials the imaginary part is usually negligible $\varepsilon_{med} = \mathsf{Re}\{\varepsilon_{med}(\omega)\}$. Thus, for a small or only weakly dispersive imaginary part $\mathsf{Im}\{\varepsilon_{np}(\omega)\}$ of the nanosphere's permittivity, the resonance condition can be found to be

$$\mathsf{Re}\{\varepsilon_{np}(\omega)\} = -2\varepsilon_{med}, \tag{2.35}$$

which is also known as Fröhlich condition [18]. These resonant oscillation modes which occur in the free electrons of a metal nanosphere are the localised surface plasmons (LSP) [16].

We further want to derive the optical properties represented by the scattering and absorption cross section. These physical quantities serve to describe the optical response of the gold nanosphere during interaction with light. First, we focus on the scattering cross section as the more important quantity in this work. Afterwards, we consider the derivation of the absorption cross section.

Scattering Cross Section. The scattering cross section σ_{scatt} is defined as the quotient of the radiated power P and the energy density of the exciting electromagnetic wave ρ [10],

$$\sigma_{scatt} = \frac{P}{\rho}. \tag{2.36}$$

The latter is given as

$$\rho = \frac{\varepsilon_0 c}{2n}E_0^2\varepsilon_{med}. \tag{2.37}$$

Here, c is the speed of light and n is the refractive index in the medium. To determine P, we utilise the Pointing vector $\vec{S}$ which describes the average power per unit area of a point dipole as which a small nanosphere can be treated. $\vec{S}$ is defined as [17]

$$\vec{S} = \vec{E} \times \vec{H}. \tag{2.38}$$

The electric field $\vec{E}$ of a point dipole has the form [17]

$$\vec{E} = \frac{1}{4\pi\varepsilon_0\varepsilon_{med}} \left[k^2(\hat{r} \times \vec{p}) \times \hat{r}\frac{e^{ikr}}{r} + [3\hat{r}(\hat{r} \cdot \vec{p}) - \vec{p}] \left(\frac{1}{r^3} - \frac{ik}{r^2}e^{ikr} \right) \right]. \tag{2.39}$$

The corresponding magnetic field $\vec{H}$ is given as [17]

$$\vec{H} = \frac{ck^2}{4\pi}(\hat{r} \times \vec{p})\frac{e^{ikr}}{r} \left(1 - \frac{1}{ikr} \right) \tag{2.40}$$

Here, k denotes the light's angular wavenumber with $k = \frac{\lambda}{2\pi}$. The power P of the point dipole can be determined by integrating $\vec{S}$ over all spacial angles [17] and results in

$$\begin{aligned} P &= \frac{w^4}{12\pi\varepsilon_0\varepsilon_{med}}|\vec{p}| \\ &= \frac{ck^4}{12n\pi\varepsilon_0\varepsilon_{med}}|\alpha|^2|E_0|. \end{aligned} \tag{2.41}$$

This expression for P is inserted in Equation 2.36 together with Equation 2.37. Thus, we obtain an expression of the scattering cross section of the nanosphere as

$$\sigma_{scatt} = \frac{k^4}{6\pi\varepsilon_0^2}|\alpha|^2 \tag{2.42a}$$

$$= \frac{8\pi k^4 a^6}{3} \left| \frac{\varepsilon_{np} - \varepsilon_{med}}{\varepsilon_{np} + 2\varepsilon_{med}} \right|^2. \tag{2.42b}$$

Absorption Cross Section. The absorption cross section σ_{abs} is defined similar to the scattering cross section with the difference that the total dissipated power P_{diss} is used instead of the radiated power P. Thus, σ_{abs} is defined as

$$\sigma_{abs} = \frac{P_{diss}}{\rho}. \tag{2.43}$$

P_{diss} is given by the Pointing theorem as [10]

$$P_{diss} = \frac{kc}{2n}\mathrm{Im}\{\vec{p} \cdot \vec{E_0}^*\}. \tag{2.44}$$

Here, $\vec{E_0}^*$ denotes the complex conjugated amplitude of the excitation field. We again utilise the expression of ρ in Equation 2.37 and together with Equation 2.44 we can derive an expression for the absorption cross section σ_{abs},

$$\sigma_{abs} = \frac{k}{\varepsilon_0}\mathrm{Im}\{\alpha\} \tag{2.45a}$$

$$= 4\pi k a^3 \mathrm{Im}\left\{ \frac{\varepsilon_{np} - \varepsilon_{med}}{\varepsilon_{np} + 2\varepsilon_{med}} \right\}. \tag{2.45b}$$

The extinction cross section σ_{ext} of the plasmonic nanosphere is defined as the sum of the scattering and absorption cross section [16] and reads as

$$\sigma_{ext} = \sigma_{scatt} + \sigma_{abs} \ , \tag{2.46}$$

with σ_{scatt} and σ_{abs} are proportional to $|\alpha|^2$ respectively Im$\{\alpha\}$. Therefore, the Fröhlich condition in Equation 2.35 applies on both. However, because of the square σ_{scatt} appears more dominant for an increasing radius.

2.3 Nanorod

We have only considered nanospheres so far. In the following experiments we are going to examine nearly ellipsoidal nanoparticles, so-called nanorods. In contrast to spheres, rods have three semiaxes of different lengths. We define a to be the longest and $b = c$ as the shorter semiaxes. Thus, we obtain two different symmetry axes. We consider a similar picture as for the nanosphere of a nanorod irradiated by an external electromagnetic wave. Since the rods is small compared to the wavelength of the wave it can be treated as in a homogenous electric field (Figure 2.2).

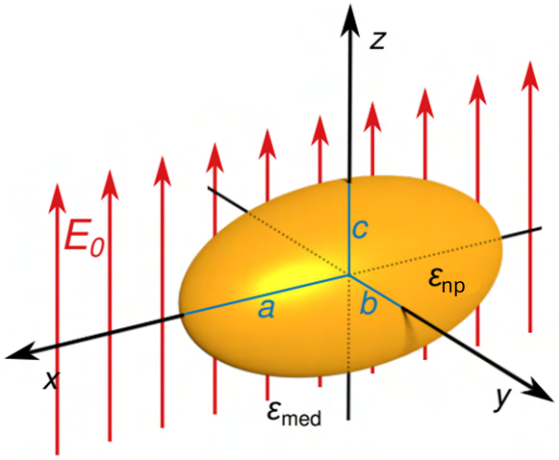

Figure 2.2: A nanorod has three principal semiaxes, denoted a, b, and c. While all three are oriented along different directions, the b and c semiaxes have equal lengths.
This image was taken from Reference [16] and was slightly adjusted.

We are again interested in the optical features of the nanoparticle represented by the scattering and absorption cross section. The derivation follows similar ideas as elaborated for spherical particles. Therefore, only the main concepts will be shown here. The comprehensive derivation can be found with further details in the book of Bohren and Huffman and is briefly outlined here by following their arguments [19].
When considering a sphere we started with the Laplace equation in spherical coordinates and we proceed analogously for an ellipsoidal particle. At first we define ellipsoidal

coordinates for describing the problem,

$$\frac{x^2}{a^2+\xi}+\frac{y^2}{b^2+\xi}+\frac{z^2}{c^2+\xi}=1\ ; \quad -c^2<\xi<\infty, \tag{2.47a}$$

$$\frac{x^2}{a^2+\eta}+\frac{y^2}{b^2+\eta}+\frac{z^2}{c^2+\eta}=1\ ; \quad -b^2<\eta<-c^2, \tag{2.47b}$$

$$\frac{x^2}{a^2+\zeta}+\frac{y^2}{b^2+\zeta}+\frac{z^2}{c^2+\zeta}=1\ ; \quad -a^2<\zeta<-b^2. \tag{2.47c}$$

Thus, we can determine an expression for the Laplace equation in ellipsoidal coordinates as

$$\begin{aligned}\nabla^2\Phi =&(\eta-\zeta)f(\xi)\frac{\partial}{\partial\xi}\left[f(\xi)\frac{\partial\Phi}{\partial\xi}\right]\\ &+(\zeta-\xi)f(\eta)\frac{\partial}{\partial\eta}\left[f(\eta)\frac{\partial\Phi}{\partial\eta}\right]\\ &+(\xi-\eta)f(\zeta)\frac{\partial}{\partial\zeta}\left[f(\zeta)\frac{\partial\Phi}{\partial\zeta}\right]=0\end{aligned} \tag{2.48}$$

with $f(q)=\left[(q+a^2)(q+b^2)(q+c^2)\right]^{1/2}$. Since the system has not changed except of the shape of the nanoparticle, the same boundary conditions have to apply as we found for the sphere. Utilizing Equation 2.18a - 2.18d we obtain expressions for the potential inside and outside of the rod. It is exemplarily shown for semiaxis c:

$$\Phi_1=\Phi_0\frac{1}{1+\frac{L_c(\varepsilon_{np}-\varepsilon_{med})}{\varepsilon_{med}}}, \tag{2.49a}$$

$$\Phi_2=\Phi_0+\Phi_0\frac{\frac{abc}{2}\int_\xi^\infty\frac{dq}{(q+c^2)f(q)}}{1+\frac{L_c(\varepsilon_{np}-\varepsilon_{med})}{\varepsilon_{med}}}. \tag{2.49b}$$

L_c is a geometrical factor of the form

$$L_c=\frac{abc}{2}\int_0^\infty\frac{dq}{(d+c^2)f(q)}. \tag{2.50}$$

It depends on the dimension of the rod in a, b and c. In analogy to the polarizability of a nanosphere we derive the polarizability of a nanorod along c via Equation 2.31 and 2.49b:

$$\alpha_c=4\pi\varepsilon_0 abc\frac{\varepsilon_{np}-\varepsilon_{med}}{3\varepsilon_{med}+3L_c(\varepsilon_{np}-\varepsilon_{med})}. \tag{2.51}$$

Equation 2.50 and 2.51 can be easily converted into a general expression of the polarizability along the main axes of the nanorod with the form

$$\alpha_i=4\pi\varepsilon_0 abc\frac{\varepsilon_{np}-\varepsilon_{med}}{3\varepsilon_{med}+3L_i(\varepsilon_{np}-\varepsilon_{med})} \tag{2.52a}$$

with

$$L_i=\frac{abc}{2}\int_0^\infty\frac{dq}{(d+s_i^2)f(q)}. \tag{2.52b}$$

Via the polarizability we obtain the optical properties of a nanorod. To this end, Equation 2.52a is inserted in the expressions we derived for σ_{scatt}, Equation 2.42a, and in the expression of σ_{abs}, Equation 2.45a.

$$\begin{aligned}\sigma_{scatt} &= \frac{k^4}{6\pi\varepsilon_0^2}|\alpha_i|^2 \\ &= \frac{8\pi k^4 (abc)^2}{3}\frac{\varepsilon_{np}-\varepsilon_{med}}{3\varepsilon_{med}+3L_i(\varepsilon_{np}-\varepsilon_{med})}, \qquad (2.53a)\\ \sigma_{abs} &= \frac{k}{\varepsilon_0}\mathrm{Im}\{\alpha\} \\ &= 4\pi kabc\mathrm{Im}\left\{\frac{\varepsilon_{np}-\varepsilon_{med}}{3\varepsilon_{med}+3L_i(\varepsilon_{np}-\varepsilon_{med})}\right\} \qquad (2.53b)\end{aligned}$$

Here, L_i is a geometrical factor which depends on the polarisation of the exciting electromagnetic wave. Due to the symmetry of a nanorod we obtain different solutions for the semiaxes. Only that part of the electric field which propagates along the considered axis contributes to a response in that direction. Since b and c have the same length they show a similar response. Thus, the different geometrical factors can be found to be

$$L_a = \frac{1-e^2}{e^2}\left[\frac{1}{2e}ln\left(\frac{1+e}{1-e}\right)-1\right] \qquad (2.54a)$$

and

$$L_{b,c} = \frac{1-L_a}{2} \qquad (2.54b)$$

with e as the eccentricity with $e = (1-b^2/a^2)^{1/2}$.
Via Equation 2.53a and 2.53b we can again derive the resonance condition for nanorods which results in

$$\mathrm{Re}\{\varepsilon_{np}\} = (1-\frac{1}{L_i})\varepsilon_{med}. \qquad (2.55)$$

Due to the dependence on the geometrical factor the Fröhlich condition for nanorods can be fulfilled for two resonance frequencies. The resonance of the longest semiaxis a is the so-called longitudinal resonance, while the resonance of b and c is referred to as transversal.

2.4 Chemical Interface Damping (CID)

Plasmons decay via different mechanisms which can be classified into three groups [20, 21]:

$$\Gamma_{total} = \gamma + \Gamma_{rad} + \Gamma_{surf}.$$

Here, Γ_{total} denotes the sum of all damping processes including damping via interband and intraband transitions γ, via radiative processes Γ_{rad} and via surface damping Γ_{surf}. γ depends on the properties of the bulk material of the nanoparticle and can be described by its dielectric function ε [22, 23]. The plasmon decays via generating excited electron-hole pairs with electrons either from the 5d band or the conduction band. In

a second step the excited carriers can be injected into the environment of the particle, which is also known as indirect or sequential charge transfer. Γ_{rad} describes radiative decay, whereby a plasmon is damped by the emission of a photon. This process increases with the size and is negligible for particles smaller than approximate 20 nm [22].
Surface damping covers two different mechanisms. On one hand, it includes the scattering of plasmons with the surface of the particle. This occurs if the dimension of the particle is below the mean free path of the electrons. On the other hand, it encompasses the so-called CID, which depends on the interaction of the nanoparticle with its environment [24, 25, 26]. Different processes are combined under CID such as dipole scattering, plasmon-induced direct charge transfer (PICT) and resonance energy transfer [8]. In this work PICT is the mainly desired effect because of its positive influence on the efficiency of charge transfer in photoelectric and photocatalytic systems [27, 28]. The density of electronic states of the particle and an attached material couple leading to a hybridized surface state. It has contributions of both materials but it is located mainly in the electron-acceptor participant. By exciting an electron via plasmon decay from the nanoparticle to this state it is directly injected in the attached material [28, 29]. Thus, the generated electron cannot be damped before injection due to their direct transfer and the entire energy of the plasmon is transferred. Additionally, the recombination of the electron-hole pair is suppressed due to their separation, which increases the efficiency of charge transfer [8]. PICT occurs mainly at metal-molecule and metal-semiconductor interfaces [8, 27]. CID including PICT acts as an additional decay channel and leads therefore to a damping of the LSP which is visible in a broadening of the plasmon resonance peak [28, 30].

2.5 Photocharging

The so-called photocharging process describes the accumulation of additional negative charges on the nanoparticle during irradiation with a laser. It is schematically illustrated in Figure 2.3. The image was taken from the paper of Stete, Bargheer and Koopman regarding photocharging ensemble of GNRs [1]. The explanation given here follows their arguments.

Qualitative Description. We consider a gold nanorod surrounded by a solution containing ethanol. The latter is an active reducing agent since it readily undergoes oxidation itself and is therefore called a hole scavenger [31, 32, 33]. At the beginning the system is in an equilibrium state. Thus, the chemical potential of the holes μ_h^* is equal to the particle's Fermi energy E_F and aligned with the chemical potential of the solution μ_{sol}. When the nanorod is irradiated with a laser the particles absorb photons either via direct interband transitions or via plasmonic absorption. The energy of the photon stored in the plasmon can be employed to excite a core electron from the 5d-band to the Fermi level E_F when the plasmon decays. Thus, both cases result in the generation of excited holes in the 5d-band [31], which leads to a decrease of μ_h^*. The resulting potential difference between μ_h^* and the redox potential of ethanol μ_{sol} causes a corresponding voltage U_{photo}, which acts as a driving force for a charge transfer. The holes as positive charges move to the solution and get exchanged by electrons via oxidizing ethanol. Thus, the electronic states at lower energies become fully occupied and suppress the radiative or non-radiative decay of the excited electrons. Furthermore, additional negative charges

were transferred to the particle. These excess electrons accumulate on the surface of the nanoparticle because of repulsion forces between equal charges.
To stabilize the system an electric double layer is formed around the particle. Positive charges of the solution accumulate on the surface of the particle leaving an electric neutral layer from a global point of view. The potential difference between these two accumulated opposite charges generates a voltage U_{charge} between the nanorod and the surrounding solution, which lifts the band structure of the gold particle. The system approaches equilibrium for $\mu_h^* = \mu_{sol}$ [1]. Because of the elevation of the energy levels and its influence of ε_{np}, this effect is visible in a shift to higher energies for the LSPR.

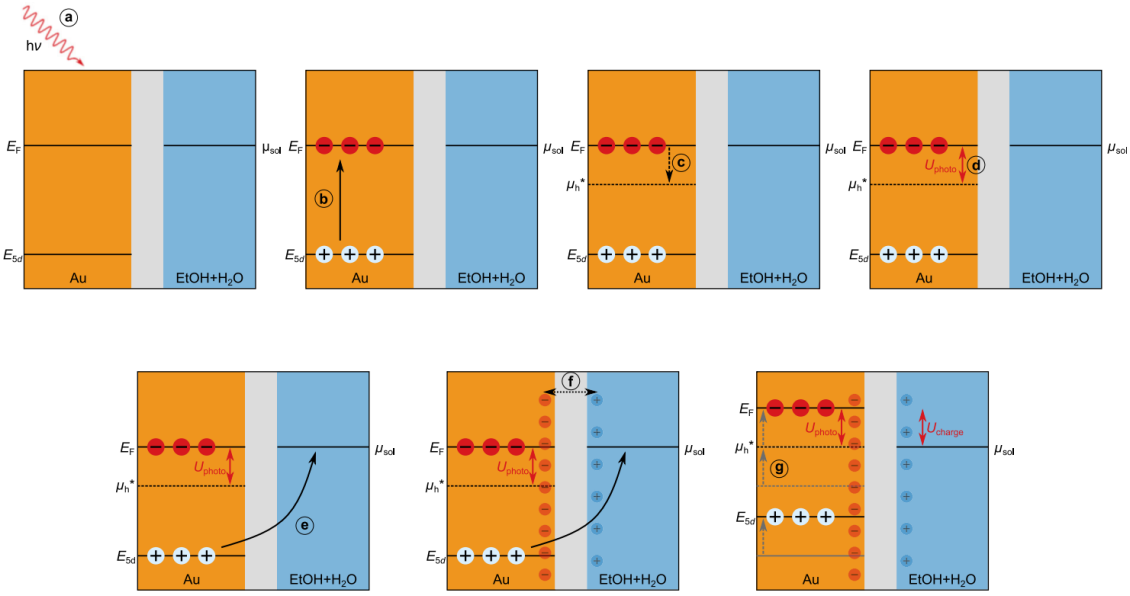

Figure 2.3: **a)** A photon is absorbed and **b)** its energy is used to excite electrons of the 5d-band to the Fermi level. **c)** The excited holes reduce μ_h^* **d)** leading to a potential difference between μ_h^* and μ_{sol}. **e)** The resulting U_{photo} drives the transfer of electrons from ethanol to the GNR via oxidation of the ethanol molecules. **f)** Excess electrons accumulate on the surface of the GNR and the system stabilizes by forming an electric double layer around the particle. **g)** The potential difference between both layers leads to an elevation of the GNR's bandstructure until $\mu_h^* = \mu_{sol}$. This figure is taken from Reference [1] where this concept was established.

Mathematical Description. The process can also by described mathematically following again the arguments of Reference [1]. The nanoparticle is considered as a nanoscale capacitor which is charged by a voltage U_{Photo} with electrons from solution. After a certain time it approaches a saturation with a maximum charge Q_{max} which is accumulated on the GNR with $Q_{max} = q_e \Delta N_e$. Here, q_e is the charge of an electron and ΔN_e denotes the number of excess surface charges. With these physical quantities an expression for the capacitance of the nanoparticle can be found to be

$$C = -q_e \Delta N_{e,max} / U_{Photo}. \tag{2.56}$$

Additionally, in the picture of the capacitor we obtain an expression of the time resolved behaviour regarding the number of charges stored on the particle during the charging process:

$$N_e = N_{e,0} + \Delta N_{e,max}(1 - e^{-\frac{t}{\tau}}). \tag{2.57}$$

Here, $N_{e,\,0}$ corresponds to the number of bulk electrons, t denotes the time from the start of the irradiation and τ is the charging time constant which can be interpreted as a transfer rate of the holes from the nanoparticle to ethanol. By assuming only a small shift of the relative LSPR, $\Delta\omega/\omega_0$ can be considered proportional to $\Delta N_e/N_{e,0}$. This is valid because the relative shift is expected to be below 1% [1]. Thus, a time dependent expression for the shift of the LSPR can be derived to be

$$\omega(t) = \omega_0 + \Delta\omega_{max}(1 - e^{-\frac{t}{\tau}}) \tag{2.58}$$

with $\Delta\omega_{max}$ as the maximum shift of the resonance frequency.
To fully understand this equation an expression for τ has to be determined. To this end, an interpretation of the limitation of the transition rate of holes from the GNR to the ethanol has to be found. The most simple model introduces an energetic activation barrier E_A. The origin of this barrier is not known but could possibly be similar to a Schottky barrier on the interface of gold and ethanol [34]. However, the barrier has to be dependent on the irradiation intensity I and by considering the LSPR it also depends on μ_h^*. An expression can be found as

$$\begin{aligned} E_A(I) &= E_A' - \mu_h^*(I) \\ &= \beta + k_B T ln(I) \end{aligned} \tag{2.59}$$

with E_A' and β as constants independent of I.
From this we can determine the expression for the time constant

$$\begin{aligned} \tau = \frac{1}{k} &= \left(k_0 + e^{\frac{E_A}{k_B T}}\right)^{-1} \\ &= \left(k_0 + I e^{\frac{\beta}{k_B T}}\right)^{-1}. \end{aligned} \tag{2.60}$$

Here, k_B denotes the Boltzmann constant, k_0 a dark rate, which describes a charging reaction without illumination and T denotes the temperature.

2.6 Measurement Techniques

2.6.1 Dark-Field Microscopy

Common microscopy uses bright-field imaging to depict objects. The transmitted light is recorded and objects appear due to their extinction properties as dark structures. This method is not suitable for nanostructures. Because of their small size, the contrast of their extinction cross section compared to the bright background is too small. A solution is dark-field microscopy. In contrast to bright-field imaging only the light scattered by the sample is recorded. Thus, the background appears dark and objects are visible as bright spots. The contrast is enhanced and small objects up to nanoparticles become visible.
The differences between a bright-field and a dark-field image can be seen in Figure 2.4a

and 2.4b. Both images were taken of the same field of view but nanoparticles are only visible in the dark-field image on the right hand. They appear as colourful dots. The bigger structure which is visible in both images corresponds to a scratch on the surface of the glass substrate.

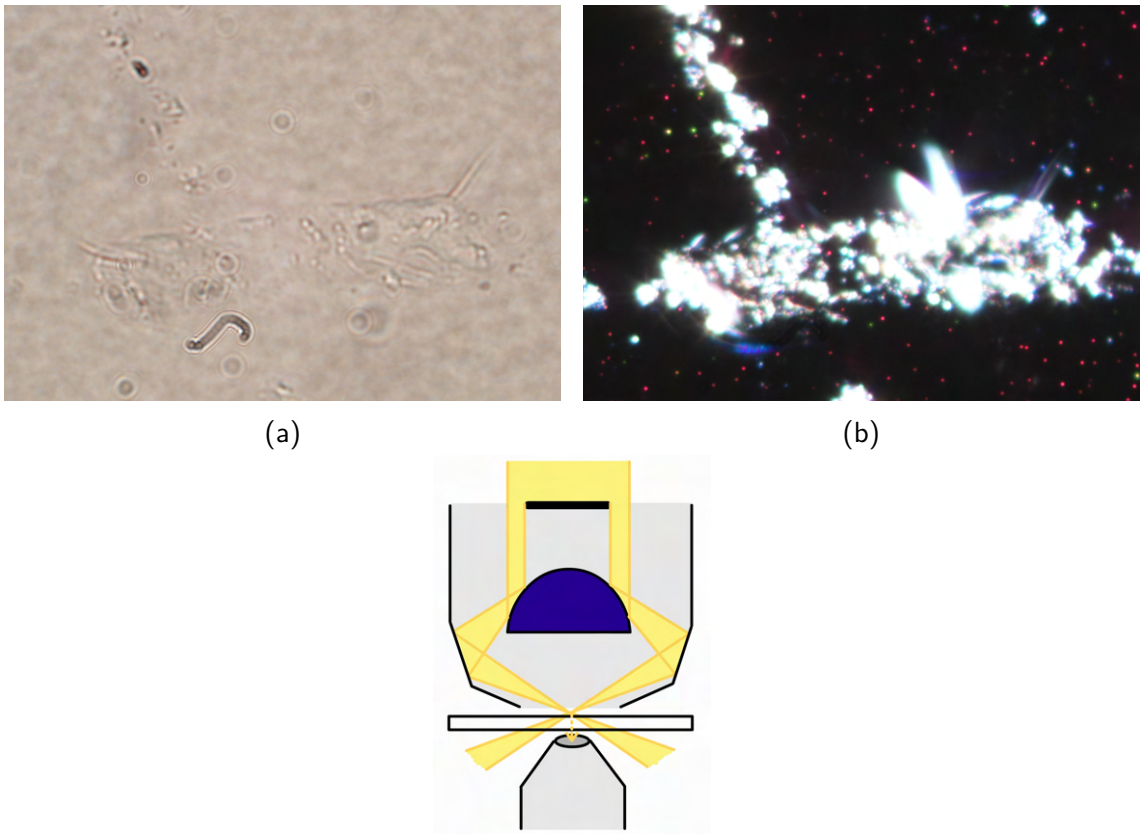

(a) (b)

(c)

Figure 2.4: **(a)** Bright-field image and **(b)** dark-field image of the same field of view. Nanoparticles are visible in the dark-field image as colourful dots, but they disappear in the bright-field image. **(c)** Schematic image of a dark-field oil immersion condenser. Only the scattered light depicted by the dashed arrow reaches the objective.

There are different technical methods and devices to enable dark-field. In this experiment a dark-field condenser was used [35]. The schematic structure of this device is shown in Figure 2.4c. First, the centre of the incoming light beam is blocked. The remaining light is reflected inside the condenser in such a way that it reaches the sample at an angle greater than the aperture angle of the objective. The light beam is focused on the surface of the sample but it maintains its angle unless it is scattered by an obstacle. Thus, a dark spot occurs beyond the sample position. By placing the objective in this dark spot only the forward scattered light reaches the detector [35].

Limitation. The resolution of an optical microscope is fundamentally limited by diffraction, as described by the Abbe limit. When light passes through or is scattered by small structures, it forms diffraction patterns rather than ideal point images. Thus, adjacent details overlap. Consequently, two points can only be distinguished as separate if their

distance d is $d \geqslant \Delta x_{min}$ with [13]

$$\Delta x_{min} = 0.61 \frac{\lambda}{NA} \tag{2.61}$$

Here, λ denotes the wavelength of the illuminating light and NA the numerical aperture of the objective. For an irradiation wavelength of λ =600 nm and an 100x oil objective with a numerical aperture of $0.5 \leqslant NA \leqslant 1.3$ as it was used during the measurements, Δx_{min} ranges from 732 nm to 281.5 nm . Consequently, small objects such as nanoparticles may be visible by the dark-field microscopy but all information regarding their shape and size get lost. Accordingly, they only appear as bright spots on the recorded image. Additionally, if two nanoparticles are located closely together or clumped, they can not be distinguished from a single nanoparticle using dark-field microscopy.

2.6.2 Scanning Electron Microscopy (SEM)

In order to distinguish single nanoparticles from clumped GNRs an electron microscope was used complementary. Electrons can show wave-like behaviour when interacting with other objects as it was discovered by Louis de Broglie. The corresponding de Broglie wavelength of an electron is given as [6]

$$\lambda_{dB} = \frac{h}{p_e} \tag{2.62}$$

with h denoting the Planck constant and p_e the impulse of the electron.
Inside the scanning electron microscope (SEM), electrons are emitted by a hot cathode and become accelerated via a perforated anode. Thus, an electron beam is generated, the so-called primary beam, which is focused on the sample. At the sample's surface the electrons interact with atoms and electrons of the sample via elastic and inelastic collusions. Due to their high energy the incoming electrons eject surface electrons via inelastic scattering from the material. These are referred to as secondary electrons which can be utilized to gain information regarding the topography of the surface. Additionally, Bremsstrahlung and Röntgen scattering occur, which can be employed for material analysis. For imaging the surface an Inlens detector was used, which measures the secondary electrons. By scanning the surface row by row a spatial resolution can be obtained [36]. The wavelength of electrons is much smaller than the visible range and can be enhanced by the acceleration of the electrons before reaching the sample surface. λ_{dB} can be determined via the energy ansatz at a given acceleration voltage U_a [6]:

$$\begin{aligned} E_{el} &= E_{kin} \\ \Rightarrow q_e U_a &= \frac{1}{2} m_e v^2 \\ \Rightarrow v &= \sqrt{2 U_a \frac{q_e}{m_e}}. \end{aligned} \tag{2.63}$$

Here, q_e is the charge of an electron, m_e its mass and v its velocity. By including this in Equation 2.62 an expression for the de Broglie wavelength can be found as

$$\lambda_{dB} = \frac{h}{\sqrt{2 U_a q_e m_e}}. \tag{2.64}$$

For an acceleration voltage of U_a=2 kV the wavelength of the electrons results in 0.0274 nm. This resolution enables the visualization of nanoparticles.

3 Methods

This chapter introduces the experimental setup used for recording single particle scattering spectra and the employed experimental procedures for sample preparation and data acquisition. Using this setup various experiments regarding charge transfer processes on the single-particle level were conducted.
Three different experiments were performed in order to investigate various aspects of interfacial charge transfer and the interaction of GNRs with their environment. First, in experiment A, three kinds of nanoparticles were measured on different substrates with various conductivity properties in order to detect and investigate CID. In the second experiment B, the electrostatic properties of the environment around the particles was altered by changing the pH value, consequently, variating the number of H^+ ions in the surrounding solution. The aim was to measure the same individual particles for all different pH values to eliminate average or cumulative effects. The third and most central experiment C dealt with photo-induced charging of single GNRs. The transfer and accumulation of electrons on a nanoparticle were investigated via recording the behaviour of the LSP.All experiments were prepared and recorded using largely the same procedure and setup up to slight differences. In each section the general procedure is introduced at first and optionally supplemented by paragraphs with information regarding a specific experiment.
The investigated nanoparticles are presented in Section 3.1 and the substrates used in Section 3.2. This is followed by the sample preparation in Section 3.3 which includes different steps of cleaning as well as distributing and attaching the GNRs on the substrates. In Section 3.4.1 the setup for the single particle dark-field recording is shown and explained in detail followed by the experimental procedure carried out on this setup in Section 3.4.2. Lastly, in Section 3.4.3 the procedures for co-localization of particles measured with dark-field microscopy using an SEM is presented. The relevance of an verification via SEM images is discussed and emphasised by comparing the appearance of single and clumped GNRs in the dark-field and SEM image.

3.1 Different Nanorod Types

In this work only nanorods were investigated. Their longitudinal resonance is enhanced compared to the resonance of spherical gold particles. Due to the higher dipole moment of GNRs the longitudinal resonance is shifted in the energetic region were the imaginary part of gold is negligible and only Drude electrons interact with the incoming light. On one hand this increases the scattering intensity of the nanoparticles making them easier to observe on the single-particle level. On the other hand the plasmon damping via interband transitions is suppressed. Thus, the contribution of surface effects is increased which enhances the visibility of the optical response of the nanoparticles to the phenomena to be investigated. Additionally, the separation in two resonances enables to excite the transversal resonance while parallel observing the longitudinal resonance. This was utilized during the photocharging experiment C.

Experiment A. Measurements of nanorods with three different sizes and aspect ratios were taken. All of the nanorods consisted of pure gold and were coated with cetyltrimethylammonium bromide (CTAB). This ligand causes mainly a steric repulsion but additionally imparts a positive charge of the GNR which leads to a electrostatic repulsion as well. Both processes are important to prevent the GNRs from forming clumps. An overview of the different kinds of nanoparticles and their most important parameters is given in Table 3.1.

Name	Diameter [nm]	Length [nm]	transversal LSPR [nm]	longitudinal LSPR [nm]
DH16	28.15 $\pm$ 2.27	81.57 $\pm$ 7.62	515 (527)	727 (694)
DH15	40.90 $\pm$ 2.35	100.5 $\pm$ 6.16	522 (528)	705 (652)
MS07	29.00 $\pm$ 1.76	77.50 $\pm$ 6.07	515 (527)	739 (672)

Table 3.1: Overview of the important parameters of the GNRs used for measurements on different substrates. The rods consist of gold and were coated with CTAB. They were produced by Shivani Kesarwani. The resonance positions were measured in an aqueous solution using a UV/VIS spectrometer (and calculated for a glass environment).

Nanoparticles of these sizes were chosen to simplify the measuring of single particles as they are large enough to be clearly visible using a dark-field microscope. The scattering cross-section is proportional to $(abc)^2$, thus, the scattering intensity increases significantly for larger particles.

Experiment B and C. For investigating the influence of a decreased pH value and photocharging on the LSPR smaller particles compared to experiment A were used. Both phenomena have mainly an impact on the behaviour at the surface of the GNRs. Since smaller particles have a higher surface to volume ratio the contribution of the surface to the spectra of the particle is increased and surface effects become more significant.

Name	Diameter [nm]	Length [nm]	transversal LSPR [nm]	longitudinal LSPR [nm]
A12-25-700	25.00	75.00	516 (527)	690 (704)

Table 3.2: Overview of the important parameters of the GNRs used for measurements regarding different pH values and photocharging. The rods consist of gold and were coated with PVP. They were produced by Nanopartz [37]. The values for the resonance positions were measured in an aqueous solution using a UV/VIS spectrometer (and calculated for an glass environment).

Only one kind of GNRs was used for measuring the LSPR behaviour with a decreasing pH value and during photocharging (Table 3.2). These particles consisted also of gold but were coated with polyvinylpyrrolidone (PVP). It causes mainly a steric stabilization and is an only weakly reactive molecule. Thus, on one hand, observed effects will be most likely caused by the gold particles and not significantly affected by a reaction of the ligand. On the other hand the system is probably not going to be damaged during the

experiments. Another advantage of this ligand is that it leaves sufficiently large pores to allow the acid ions and the ethanol molecules to reach the surface of the particle. Especially for the photocharging measurements it is also important that PVP has a high dielectric constant of approximate $\varepsilon_{PVP} = 7.7$ [38, 39], which could enhance the capacity of a nanoparticle [40]. An overview of the most important parameters regarding the GNRs is given in Table 3.2.

3.2 Different Substrate Types

For measuring single particles, the GNRs were deposited on a substrate. During this work different materials were used especially to examine the interaction between the substrate and the GNRs regarding CID in experiment A. Therefore, materials with different conductivity properties were used. However, it is important that all of them are transparent for wavelengths in the visible range especially in the red area to be able to record the single GNR scattering spectra with an optical microscope. The materials used are listed below.

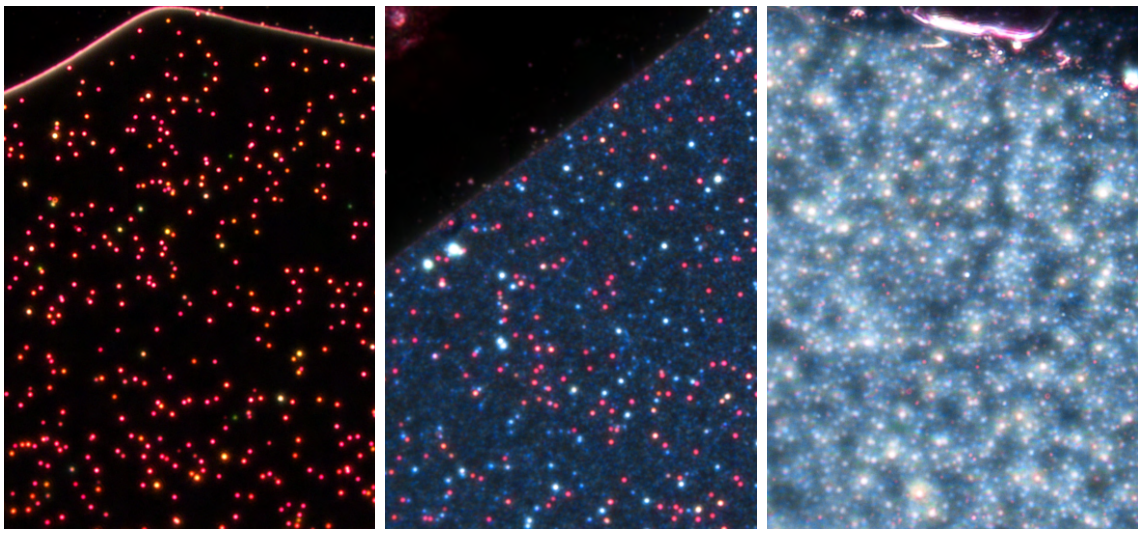

(a) (b) (c)

Figure 3.1: The substrates appear different when examined with the dark-field microscope. In all cases, the GNRs are visible as red dots: **a)** MS07 on glass, **b)** DH15 on glass and **c)** MS07 on GaN.

Glass (Figure 3.1a)
Glass is an insulating material which shows a high transparency in the visible spectrum. It was used both as a substrate with a thickness of 0.556 mm (#5) and as coverslips in all experiments with a thickness of 0.13-0.16 mm (#1), which were produced by the company "Menzel-Gläser".

ITO (Figure 3.1b)
Indium tin oxide (ITO) is a compound material. With an optimal Sn-doping concentration, a high transparency in the visible and near infrared range and a low resistivity can be achieved [41]. ITO is applied as a thin layer with a thickness of approx. 10 nm on a glass substrate. The surface has a low roughness and a resistance of 15 Ohm/square.

This object carrier was fabricated by the company "Automatic Research".

GaN (Figure 3.1c)
Gallium nitride (GaN) is a semiconductor with a wide bandgap of 3.452±0.001 eV at room temperature. It is highly transparent for photon energies below this bandgap [42]. The substrate consist of three components. A double side polished sapphire substrate with a thickness of 430±25 µm serves as base. The first layer consists of an undoped GaN buffer with a width of approx. 25 nm. It was applied to increases the quality of the layer of undoped GaN, which is placed on top with a thickness of 4.5±0.5 µm. The substrate was fabricated by the company "Nanowin".

The glass and ITO substrates were squares with a size of 24 x 24 mm. These small dimensions were necessary because of the limited space in the SEM. The GaN substrate was a waver with a diameter of 50.8 ± 0.2 mm which is exactly the size of the SEM sample holder.

Scattering of Substrates. As one can see in Figure 3.1 glass appears perfectly black in the dark-field image due to no scattering occurring in the substrate. GaN and ITO on the other hand show point-like scattering. The scattering of ITO appears more blueish with intermediate intensity, whereby GaN shows a high intense white scattering. On the ITO substrate this effect is probably caused by a rough surface since it shows visible structures in the SEM. GaN instead appears flat in the SEM and the scattering is presumably a result of dislocations in the thin layer. Since the coating grows not perfectly on the substrate, individual crystal planes can be shifted against each other. These dislocations behave like microcracks and show a strong scattering of the incoming light. Because of their small size they appear similar to nanoparticles but with less defined shapes and become visible as white dots.

3.3 Sample Preparation

All of the substrates and coverslips were cleaned using the same procedure to avoid any different outcomes caused by varied preparation processes. The substrates and coverslips were cleaned in an ultrasonic bath with different solvents. They stayed in each liquid for 10 min in the following order: First in micropore water with a resistivity of approximately 20 μOhm, then in acetone, afterwards in isopropanol and at last again in micropore water. Before the last step, they were rinsed with micropore water. A relative short duration of 10 min for each step was chosen to prevent a detachment of the ITO layer from the glass substrate and was kept for the other materials for better comparison. The cleaned substrates and coverslips were stored in micropore water until used to avoid any dust contamination. Shortly before the experiment, they were removed from the storage water and dried with nitrogen. Subsequently, the substrates and coverslips were treated with an ozone plasma and ultra violet (UV) light in a plasma oven for 30 min at 70°C.

Plasma Cleaning. Plasma cleaning is an effective method to remove remaining organic surface contaminants and to activate the surface of the substrate. The plasma oven chamber is illuminated by an UV light source with two dominant emission peaks at 185 nm and 254 nm. Since oxygen shows a strong absorption of radiation below

200 nm the light of the first emission peak is used to break the double bonds of oxygen molecules from the atmosphere leaving oxygen free radicals (O·) as a product. These highly reactive ions form immediately ozone (O_3) with additional oxygen molecules. The second dominant radiation at 254 nm gets absorbed by the organic contaminants at the surface and brings these molecules in an excited energetic state. These excited organic species can be oxidised fairly easy by ozone and oxygen free radicals. The results of this chemical reaction are volatile compounds such as water (H_2O) and carbon dioxide (CO_2). These compounds desorb from the surface and can be easily removed from the chamber [43, 44].
In addition to the cleaning effect the plasma treatment can also temporarily alter the surface energy. This happens due to two different processes. First, the removal of low surface energy contaminants during the cleaning process exposes the underlying surface, which often exhibits a higher surface energy. Second, the UV light may break down water molecules close to the surface. The resulting hydroxyl free radicals (OH·) bound to the surface via forming a functional group with a high bonding energy. These polar functional groups increase the surface energy further [43] which improves the deposition and attachment of nanoparticles [45]. Both methods are only temporary because new contaminants will bind to the exposed surface and the polar functional groups vanish through so-called hydrophobic recovery [46].

In the meantime the nanoparticles were prepared. All particles were stored in an aqueous solution. For experiment A GNRs of kind DH16, DH15 and MS07 were washed with micropore water one time before using. While for experiment B and C A12-25-700 particles were used immediately. To be able to record single nanoparticles the distance between them has to measure several micrometers. In order to achieve this distribution their concentration has to be sufficient low. The GNR solutions were therefore diluted with micropore water. DH16, DH15 and MS07 were diluted 1:7, however, as their origin concentration is not known a specific concentrations can not be provided. The used concentrations of A12-25-700 are provided in the corresponding experimental designs below.
After plasma cleaning the nanoparticles were distributed on the substrate via static spin coating, which means the solution was applied before the sample was rotated. Because of the fast rotation the particles were evenly distributed over the whole substrate. This had to be performed subsequently since the altered surface energy decreases with time. In all samples, the nanoparticles were applied within 10 min after plasma cleaning. 40 µl of GNR solution was dropped onto the substrate and subsequently rotated with 5000 rpm for 2 min. This amount of solution was found to cover the whole substrate with GNRs when spin coated. After 2 min rotation the solution was fully dried.

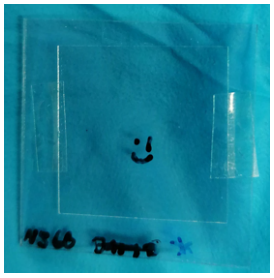

Figure 3.2: Photo of a prepared sample with a smiley as marker and protected by a coverslip.

A marker was added on the sample, either in form of a smiley drawn with a permanent pen or as a cross scratched with a glass cutter. The first one was used for experiment A while the second one was done in experiment b and C, where the substrate was employed in combination with acid or ethanol to prevent a dissolving of the marker. Lastly, a clean coverslip was added on top and was secured with adhesive tape.

ITO Substrates. Since only one side of the substrate was coated with ITO, when using these substrates, the surface resistance of both sides was measured with a multimeter before plasma cleaning. Due to the difference in conductivity and therefore surface resistance of ITO and glass, the side with the ITO coating was easily identified. This side was than placed upwards during the plasma cleaning and spin coating.

Experiment B. The behaviour of the scattering properties of GNRs in respect of the pH value were investigated. For this experiment A12-25-700 GNRs on glass were used. The particle solution was diluted 1:8 with micropore water, which corresponds to a nanoparticle concentration of $9.67 \cdot 10^9$ per ml.
The various pH values were achieved by using citric acid in different concentrations. It is a weak organic acid with the chemical formula $C_6H_8O_7$. A weak acid has only a limited tendency to donate protons and therefore remains partially protonated in solution rather than dissociating completely. Thus, an equilibrium is formed between citric acid (Citr H), and citrate and hydrogen ions ($Citr^- + H^+$) with

$$AH \rightleftharpoons A^- + H^+$$

Citric acid has three carboxyl groups (-COOH) and one hydroxyl group (-OH). Since every carboxyl groups can donate one H^+ this results in a yield of three H^+ in total. It is therefore called a tripotic acid. The donation of H^+ is carried out stepwise dependent on the pH value of the solution. In a neutral to alkaline solutions above pH 6 citric acid exists in its fully deprotonated form Cit^{3-}. For a decreasing pH value the equilibrium shifts towards the reactants. Thus, for an intermediate pH value of 3-6 less H^+ dissolve and the citric acid is predominantly present as H_2Cit^- and $HCit^{2-}$. In acidic solutions below pH 3 most of the citric acid is fully protonated (H_3Cit) [47].
The solutions were produced by mixing micropore water with citric acid powder with a purity of $\geqslant 99.5$ %. The pH value of water was chosen as base value and was reduced bit by bit. When approaching the desired pH value a part of the solution was taken out and stored for later.
Since the experiment was done two times and the acid was freshly prepared on both days, solutions with different pH values were obtained. The exact pH values are provided in Table 3.3.

dataset 1	5.93		4.51		3.57	
dataset 2	5.97	5.04		4.09	3.56	3.05

Table 3.3: Overview of the pH values used in both datasets.

The micropore water had already a lower pH due to its filtration. Therefore the measurements start with a slightly sour value. Additionally, it had been experienced that the pH value shifts to lower numbers over time probably due to chemical reactions of atmospheric carbon dioxide with water from the solution. The pH values were only

measured at the beginning of the day and therefore may differ slightly from the actual value during the experiment.
The pH value depends on the number of H^+ ions with pH$= -\log(\#\mathrm{H}^+)$ [48]. This implies stronger variations for solutions with a higher pH value when exposed to air for the same time. Since the solutions were used in descending order for the experiments, stronger differences could be avoided as solutions with a higher pH value were used first. Additionally, the solutions were stored in closed glass bottles, which contained only a small amount of air available for reactions.

Experiment C. For measuring the photocharging effect the nanoparticle solution was applied undiluted on a glass substrate. After spin coating the samples were ultrasonicated again in micropore water for 10 min. During this treatment weakly attached particles fall of and only particles that stick firmly stay on the substrate. This aims to prevent washing particles of when applying ethanol on the sample.
For measuring photocharging effects, the GNRs have to be surrounded by ethanol as a hole scavenger and ideally in an oxygen free environment, since it has the opposite effect and oxidises the particles [1]. Finding a practical sample setup was challenging due to the different requirements and constraints. The initial idea was to built a small chamber, which could contain ethanol. However, any chamber increased the distance between the surface of the sample with the GNRs and the objective above its working distance, making it impossible to bring the nanoparticles into focus. As a result, a thin film of ethanol between an object carrier and a coverslip was considered to be sufficient. The sample had to be sealed securely, since such a small amount of ethanol may evaporate fast.
Pure and undenatured ethanol (purity of $\geqslant 99.8\%$) was used to avoid any unwanted side effects due to additional chemicals. It was not diluted as according to Reference [1] there is a tendency of an increased maximum peak shift for higher ethanol concentrations. Before the ethanol was employed in the setup it was bubbled with nitrogen for approximately 30 min to remove the oxygen.

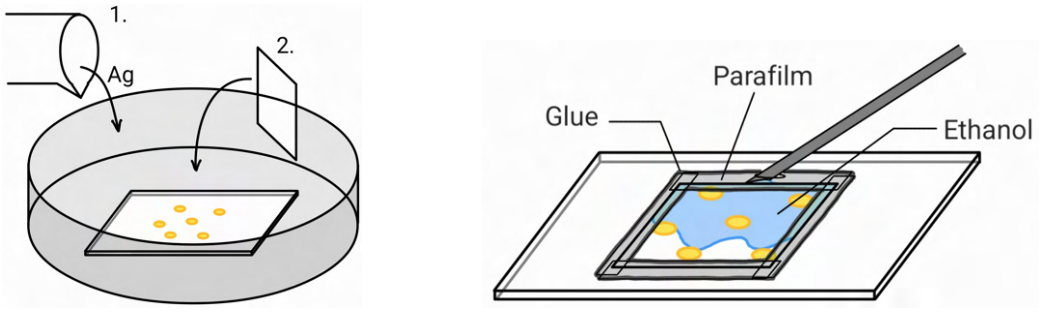

(a) (b)

Figure 3.3: **a)** The sample had been placed in a petri dish, which was then filled with argon gas. Thereafter it was closed with a coverslip.
b) The edges of the coverslip were secured with parafilm which was then sealed from the top with glue. The ethanol was injected with a syringe through the parafilm under the coverslip.

The whole setup should not contain oxygen. Therefore, the substrate coated with the GNRs was placed in a petri dish, which was then filled with argon (Figure 3.3a). Since

argon is heavier than oxygen it is intended to displace the oxygen from the bottom of the petri dish. The sample was closed carefully and slowly with a coverslip to avoid bringing new oxygen to the bottom of the petri dish via turbulences caused by fast movements. The edges of the coverslip were sealed with parafilm and additionally secured with glue. This double sealing was necessary because parafilm sticks only to dry surfaces and would detach when getting in contact with ethanol. Additionally, the glue would dissolve when getting in direct contact with ethanol as it is a solvent. Thus the parafilm is secured by glue whereby the glue is prevented from directly touching ethanol by the parafilm. With these two fastening mechanisms it was possible to attach the coverslip and close the setup to prevent further exchange with air and oxygen and to avoid evaporation of the ethanol. In a next step, the ethanol was injected with a syringe from the side through the parafilm until the space beneath the coverslip was completely filled (Figure 3.3b).

3.4 Experimental Procedure

3.4.1 Experimental Setup

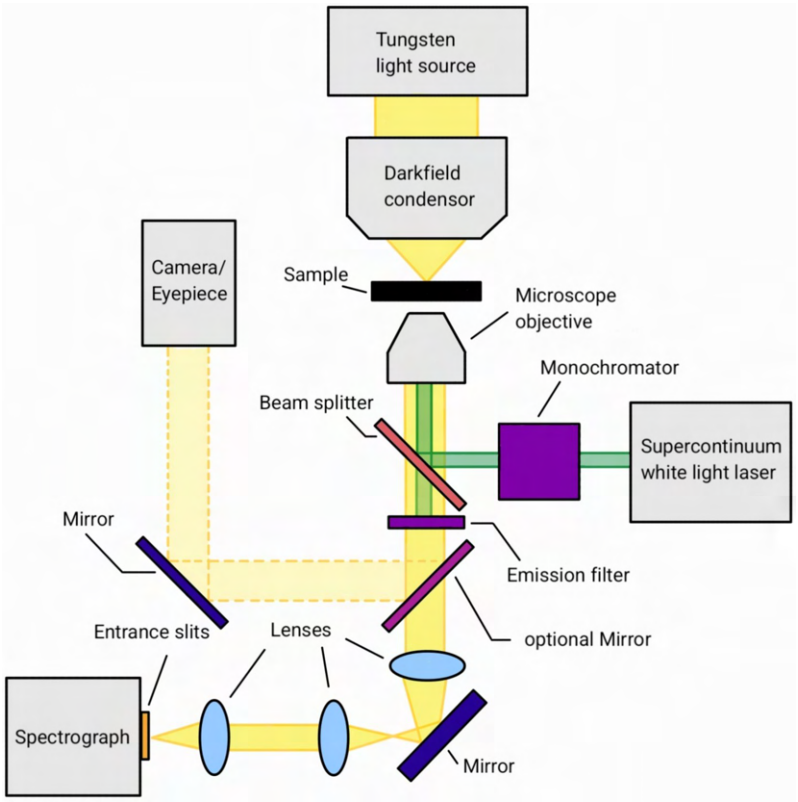

Figure 3.4: Schematic dark-field setup with an inverted Nikon TE-2000 microscope and an Andor Kymera 193i spectrograph with an iXon Ultra 888 detector.

For recording the dark-field spectra an inverted Nikon TE-2000 microscope with an oil dark-field condenser was used. In Figure 3.4 a schematic image of this setup is shown. The sample is illuminated by a tungsten lamp from the top. This light source produces white light with a maximum similar to the scattering maxima of the GNRs. Right above

the sample, a condenser was installed to enable dark-field observations. The sample holder was placed on a motorized XY stage. Because of the small dimensions of the sample, which were necessary for the SEM measurements, it could not be fastened properly by the sample holder. To prevent the sample from slipping while moving the stage, it was secured with adhesive tape to the holder.
The objective is located right beneath the sample holder. For an initial overview, a dry condenser and a dry objective (magnification 60x) were chosen, while for proper measurements an oil condenser was used together with a Nikon oil objective (magnification 100x). The second combination maximizes the amount of scattered light, which is captured by the objective and therefore increase the recorded scattering intensity of the nanoparticles. For both the objective as well as the condenser immersion oil by the company Olympus was used.
A disadvantage of the 100x oil objective is its small working distance. The sample had to be placed upside down on the sample holder since the coverslip is thinner than the object carrier and the objective was unable to bring objects at a distance of the thickness of the object carrier into focus.
The previously mentioned marker, the smiley or the scratch, was used for focusing on the sample. Since it is visible in bright-field as well as in dark-field, the surface of the sample could be brought into focus by changing the objective position before the dark-field condenser was included in the setup. Focusing both independently in sequence significantly simplifies the process.
A super continuum white light laser, a SuperK Fianium FIU-15 fabricated by NKT Photonics, was routed through the objective in order to excite the nanoparticles from below. Via a monochromator produced by the same company the excitation laser wavelength could be adjusted continuously. The laser light is not supposed to be recorded to avoid a saturation and possible damage of the detector. Therefore, an emission filter could get inserted, which blocks light below a wavelength of 530 nm. The laser was only employed in experiment(C).
In the following two different light pathways were possible. The light could either be led to the eyepiece and the Nikon camera via the optional mirror in Figure 3.4 or it reaches the spectrograph when the mirror was not included. The eyepiece was used for focusing and quick checks. The Nikon camera is able to take colour images which was important for identifying single GNRs as it is going to be discussed in the next section. The second path was enabled for recoding the scattering spectra. They were measured by an Andor Kymera 193i spectrograph with an iXon Ultra 888 detector. An entrance slid was placed in front of the spectrograph to control the incoming light. Thus, the field of view can be cropped in x-direction.

3.4.2 Data Acquisition - Dark-Field Spectra

The dark-field scattering spectra were recorded before the SEM images were taken as the high energetic electron beam, which is used in SEM, can cause variations in the scattering spectra. This was confirmed experimentally and is discussed in Section 7.1.
Particles located close to the marker were chosen to be measured, since it enables us to rediscover the GNR using both microscopes. Accordingly, in all images in Figure 3.1 a dark area can be seen, which is due to the permanent pen marker.
Nanoparticles were identified and selected by eye based on their colour in the dark-field image of the Nikon camera (Figure 3.5a). Dots with a dark red colour were preferred,

because experience has shown that these were most likely individual particles. A spectrograph can be used to show either an image with spacial resolution or to record the intensity profile depending on the wavelength. At first we use the spatially resolved image to locate the particles to be measured (Figure 3.5b). This image is only monochromatic but by comparing it with the colour image recorded by the Nikon camera the selected particles can be rediscovered.
The entrance slit width was set to 100 nm (Figure 3.5c) and additionally, the image was split horizontally with the software in segments with a chosen constant height of 50 rows around the selected single particles (Figure 3.5d). The unit of 1 row is an intrinsic unit of the software and was used to define an acquisition window of identical size for all spectra. This division into multiple compartments enabled simultaneous recording of several particles, if they were vertically aligned, as the entrance slit restricted the image only along that axis. The number of measured segments and their distance between each other depended on the number and position of particles of interest. As a result of measuring multiple particles at the same time their scattering intensity fluctuates, since some of the recorded particles may not align perfectly with the slit and appear therefore with a lower intensity. Every recorded spectrum consists of 100 accumulations. Exposure times varying between the different experiments and can be found in the following paragraphs. The measured wavelengths increase in steps of 0.424 nm whereby the range and centre were chosen differently for different experiments.

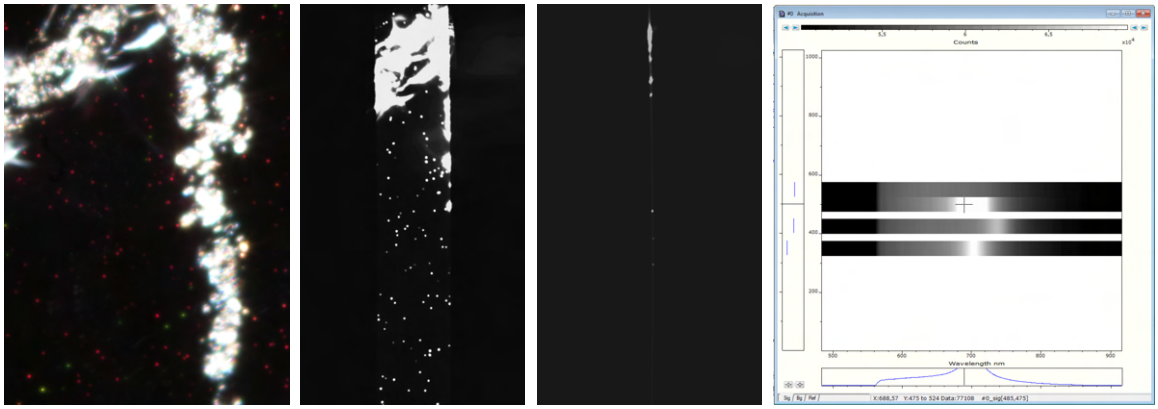

(a) (b) (c) (d)

Figure 3.5: **a)** By using the Nikon camera, a coloured dark-field image could be taken of the area of interest. The GNRs can be identified by their red colour. **b)** The image shown by the spectrograph is monochromatic, but the selected particles can be rediscovered by comparing both images. **c)** The chosen GNRs were placed in the middle of the field of view, which was then cropped via closing the entrance slit of the spectrograph to a width of 100 nm. **d)** Additionally, the image was split in horizontal segments with a height of 50 rows each around the selected GNRs. The measurement parameters were changed from space dimensions to wavelength and the corresponding scattering intensity was measured for the segments simultaneously but independent from the others.

After taking the particles' scattering spectra background and reference spectra were recorded as well. The background includes all light sources present in the laboratory

except of the tungsten lamp like passive light from the computer screen or small lights from other devices. The reference spectrum refers to the emission spectrum of the tungsten light source, which was recorded with the 100x objective but without the condenser and without a sample. Both spectra were taken with the same settings as the spectra of the GNRs regarding the entrance slit and the wavelength range but with a shorter exposure time to prevent saturation. The image was divided into 205 sections in y-direction, each with a height of 5 rows, using the Andor Solis software of the spectrograph. Later on the particle spectra were matched with the background and reference segments. Thus, the influence of potentially defective detector pixels could be reduced.

Experiment A. The scattering intensity of particles on different substrates were recorded for wavelengths between 382 nm and 816 nm, centred around 600 nm. All data with the same settings regarding the kind of particles and the material of the substrate were recorded on the same sample. Thus five different samples were used for data acquisition. The sample of DH15 particles on ITO was additionally measured twice for investigating the effect of a SEM observation on the optical properties of the GNRs. In Tabular 3.4 an overview of the important parameters is given.

Name	**Substrate**	**Date**	**Exposure time [s]**	**Number of measured GNRs**
DH16	glass	18. &. 19.09.25	0.1	20
DH15	glass	09.12.25	0.5	14
DH15	ITO	03.07.25	0.01	11
DH15 (after 1x SEM)	ITO	11.09.25	0.01	10
DH15 (after 2x SEM)	ITO	24.09.25	0.1	14
MS07	glass	11.11.25	0.5	51
MS07	GaN	18.11.25	2.0	12

Table 3.4: Overview of the dates of the recordings, the number of single GNRs measured per sample and the exposure times. Further combinations were not examined due to the limited scope of this report.

On most samples several particles were recorded simultaneously. Only when measuring the scattering behaviour of MS07 GNRs on GaN the spectra were taken exclusively one at each time. The particle of interest was located in the centre of the uncropped image.

Experiment B. The spectra during pH dependent measurements were take for a wavelength range of 483 nm to 916 nm, centred around 700 nm. Only one particle was measured at the same time and it was located at the centre of the uncropped image. Additional to this particle the segments above and underneath were recorded as empty reference measurements without a GNR. First, the solution with the highest pH value was dropped on the substrate and then replaced by the solution with the next lower value. After each measurement the sample was taken out and the coverslip was removed. The substrate with the GNRs on top was rinsed with a few drops of micropore water to neutralize the sample. It was dried as far as possible by soaking up the water drops with

a paper tissue. Since the area of interest with the GNRs should not be touched, it was not possible to dry the whole sample and the last remaining water had to evaporate. When the sample was dry, a drop of the next acid solution was added and the sample was closed with a new and clean coverslip. This was done to reduce the sources for dirt contamination. During these measurements it was not possible to use adhesive tape to secure the coverslip since it detaches when getting in contact with a wet surface. In addition, the setup had to be opened several times to exchange the pH value solution. Therefore, sealing it properly was impracticable. Instead a coverslip was employed with the same dimensions as the substrate and both were pinned with a cardboard frame wrapped in parafilm to the sample holder. The number of particles measured per pH value as well as the exposure time can be found in Table 3.5.

Name	**Date**	**Exposure time [s]**	**Number of particles per pH Value**					
			5.93/5.97	5.04	4.51	4.09	3.57/3.56	3.05
dataset 1	26.11.25	1.0	10		9		14	
dataset 2	27.11.25	1.0	9	10		8	2	1

Table 3.5: Overview of the number of single particles measured per pH value.

Experiment C. For measuring the photocharging spectra the same wavelength range as during the pH dependent measurement was chosen, 483 nm to 916 and 700 nm as the centre. Here, the methods of the first two experiments were combined. In each measurement one particle was located in the centre of the uncropped image which is also the centre of the incoming laser beam, but multiple particles were recorded simultaneously. At the same time the spectra of an additional empty segment was taken.

Name	**Date**	**Exposure time [s]**	**Excitation wavelength**	**Laser power**	**Distance to centre**	**Runtime [min]**
data 1	11.12.25	0.1	480 nm	0.28 mW	0 rows	29.59
data 2	12.12.25	0.5	480 nm	0.43 mW	0 rows	89.15
data 3	12.12.25	0.5	480 nm	0.43 mW	50 rows	89.15
data 4	12.12.25	0.27	520 nm	1.11 mW	0 rows	59.66

Table 3.6: Overview of the recorded photocharging data regarding the respective settings of the recordings. The distance to centre refers to deviation in y-direction compared to the centre of the image. The laser focus was aligned with the image centre. The runtime refers to the duration of the time-resolve measurement.

Since measuring the photocharging of single particles was a challenging procedure, the effect was successfully measured only for four particles. The respective settings can be found in Table 3.6. The sample setup was fragile and on several days it was not possible to prevent the ethanol from evaporation, which results in an air bubble forming under the coverslip. This disturbs the measurement active at that moment and contaminates the sample with oxygen. In order to compensate the evaporation of ethanol a small amount of fresh ethanol was added with a syringe after each measurement. The ethanol was stored in this syringe during the experiment. Since a syringe is not a closed system, oxygen of the air could dissolve in the ethanol. However, since the thin needle on top

of the syringe allows only a small contact area, we assume that the amount of oxygen resolved in the ethanol is negligible. Additionally, to reduce contamination, the first drops were wasted before adding ethanol to the sample setup. Ethanol was injected using a bent needle while the sample was kept in place on the sample holder.
Two different excitation wavelengths were used. Both of these selected wavelengths can drive interband transitions in gold and their excitation is enhanced by the transverse LSPR. While a larger number of interband transitions is accessible at 480 nm, the enhancement provided by the transverse plasmon resonance is stronger at 520 nm.
The measurements were started immediately after the laser was turned on. Since non of the presented data corresponds to the first recording of the day, the nanoparticles have been surrounded by ethanol already for more than an hour before the measurement started. Data 2, 3 and 4 were recorded on the same sample and data 2 and 3 were even measured simultaneously. On the second day of recordings an additional spectrum was taken of each particle after its time-resolved photocharging measurement. The particles were continuously irradiated by the laser from the start of the time-resolved measurements up to the recording of this additional spectrum. Before it was taken, the nanoparticle was brought again into focus. This refocussing was necessary because the aperture continuously defocused during the time-resolved measurement. The refocused datapoint was recorded using the same settings as for the time-resolved data. The time difference between the start of the time-resolved measurements and the corresponding refocused data can be found in Table 3.7.

Name	corresponds to	Time [min]
datapoint 2	data 2	105.5
datapoint 3	data 3	105.5
datapoint 4	data 4	98.3

Table 3.7: Overview of the refocused datapoints.

3.4.3 Data Acquisition - SEM Images

After recording the dark-field spectra images of the same particles were taken using a SEM. The samples had to be cleaned first because of the contamination with immersion oil. Electron microscopy has to be performed in a high vacuum chamber to not disturb the electron beam by interaction with air molecules. The oil would evaporate in the vacuum chamber from the sample and would therefore cause a contamination of the SEM. Additionally, the coverslip was removed since the SEM can only show the structure of the surface and can not pass through glass.
Thereafter the samples were installed on the sample holder. During the imaging the sample is irradiated with an electron beam as explained in Section 2.6.2. A lot of electrons are absorbed by the surface of the substrate. A charging of the examined area decreases the quality of the image and could even lead to repulsion effects between the charged surface and the electron beam. These are visible in a drift of the image. For the best results it is necessary to prevent charging of the observed spot during SEM imaging. While using conductive substrates ITO and GaN this problem can be easily solved by connecting the surface with the metallic sample holder using a conductive adhesive tape. The sample holder works as a grounding. Even though the glass substrates were connected in the same way with the sample holder this was not enough to prevent them

from charging and it was necessary to decrease the charging time by working fast on glass samples.

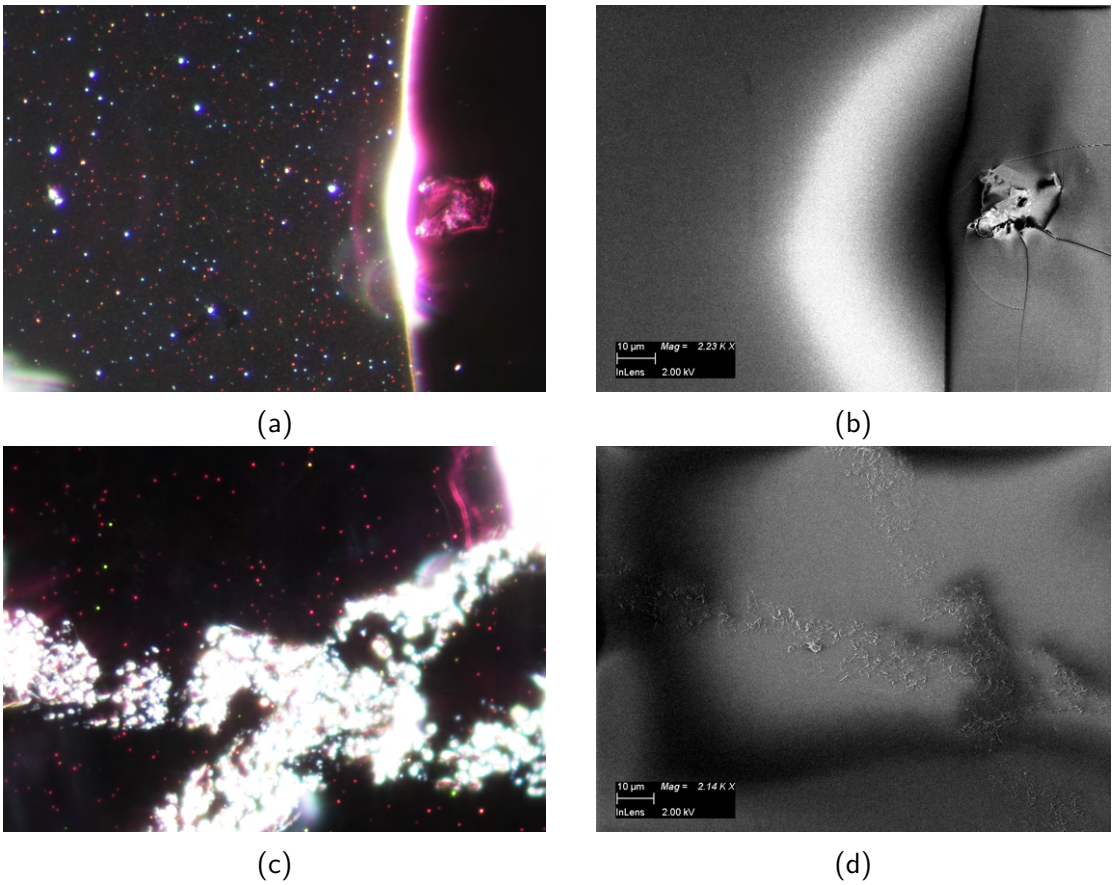

(a) (b)

(c) (d)

Figure 3.6: **a)** Dark-field image of an impurity in the permanent pen marker on an ITO substrate and **b)** the SEM image of the same spot. **c)** Dark-field image of a scratch on a glass substrate and **d)** the corresponding SEM image. The latter is a slightly rotated compare to the dark-field image. Both markers are clearly visible with both techniques and can therefore be used to rediscover the same spot. Additionally, in **d)** there are charging effects of the substrate visible as shadows.

The marker was important to rediscover the exact same nanoparticles using both microscopes. In Figure 3.6 both the smiley-marker drawn with the permanent pen and the scratch are shown. The dark-field images taken with the Nikon camera are on the left hand side together with the corresponding SEM images one the right hand side. The SEM images are slightly rotated compared to the other pictures. Nevertheless, the similarity is easy to recognize. Especially impurities in the marker (Figure 3.6a and 3.6b) or the intersection of to scratches (Figure 3.6c and 3.6d) were ideal to find the same spot with both microscopes quickly.
All images were taken with an acceleration voltage of 2 kV by using the InLens detector. The voltage is relatively low compared to the maximum possible acceleration voltage of 30 kV [49] to minimize charging of the glass substrate. Nevertheless, the resulting resolution is sufficient to identify the nanoparticles and display their shape. Still, surface charging effects appear when investigating glass substrates with the SEM and they cause

shadow-like artefacts visible in Figure 3.6d. On the ITO substrate in Figure 3.6b there are also some charging effects, but even though they seem to be significant with this magnification, problems like the repulsion of the electron beam did not occur during the investigation of single GNRs on an ITO substrate.
In Figure 3.7 images of single particles on all of the three different substrates are shown. The resolution of the GNR on glass is lower than the resolution on other substrates and a slight shadow appears around the nanoparticle because of charging of the surface. Nevertheless, all particles could be clearly visualised. ITO appears as a structured background in the SEM image which implies a higher surface roughness compared to the other two substrates used (Figure 3.7b). Additionally, weak artefacts due to charging are visible. GaN looks perfectly smooth when examined with SEM (3.7c). The absence of visual artefacts and shadows suggests excellent conductivity.

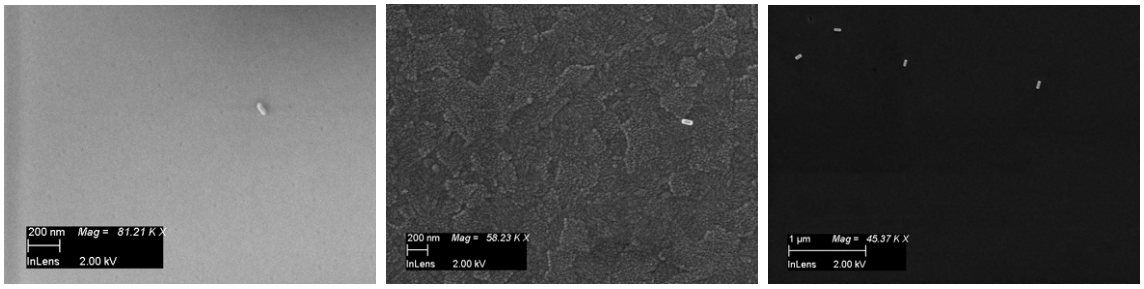

(a) (b) (c)

Figure 3.7: Exemplary SEM images of single GNRs on different substrates: **a)** A12-25-700 on glass, **b)** DH15 on ITO and **c)** MS07 on GaN.

All particles measured with dark-field were verified to be single with SEM as well. Exemplary images of particles on different substrates are shown in Figure 3.7.

Importance of SEM Images. In Figure 3.8a and 3.8b dark-field images are shown overlaid by the SEM image of the same field of view. Thus, the objects which causes the scattering structures visible in the dark-field image can be easily identified. Gold nanorods are recognizable in the SEM image due to their characteristic shape. As discussed in Section 3.4.2, the particles to be measured were selected by colour. This approach is not reliable, because GNRs from the same kind still differ in their shape and size, which causes slight variations in colours (Figure 3.8c). Similar differences can also be achieved due to clumping of particles (Figure 3.8d). Due to the Abbe limit it is not possible to distinguish single particles from clumped particles with an optical microscope [6] but the differences are clearly visible in the SEM image. Therefore was necessary to double check all of the particles measured in dark-field by using the SEM to ensure only single nanorods were analysed.

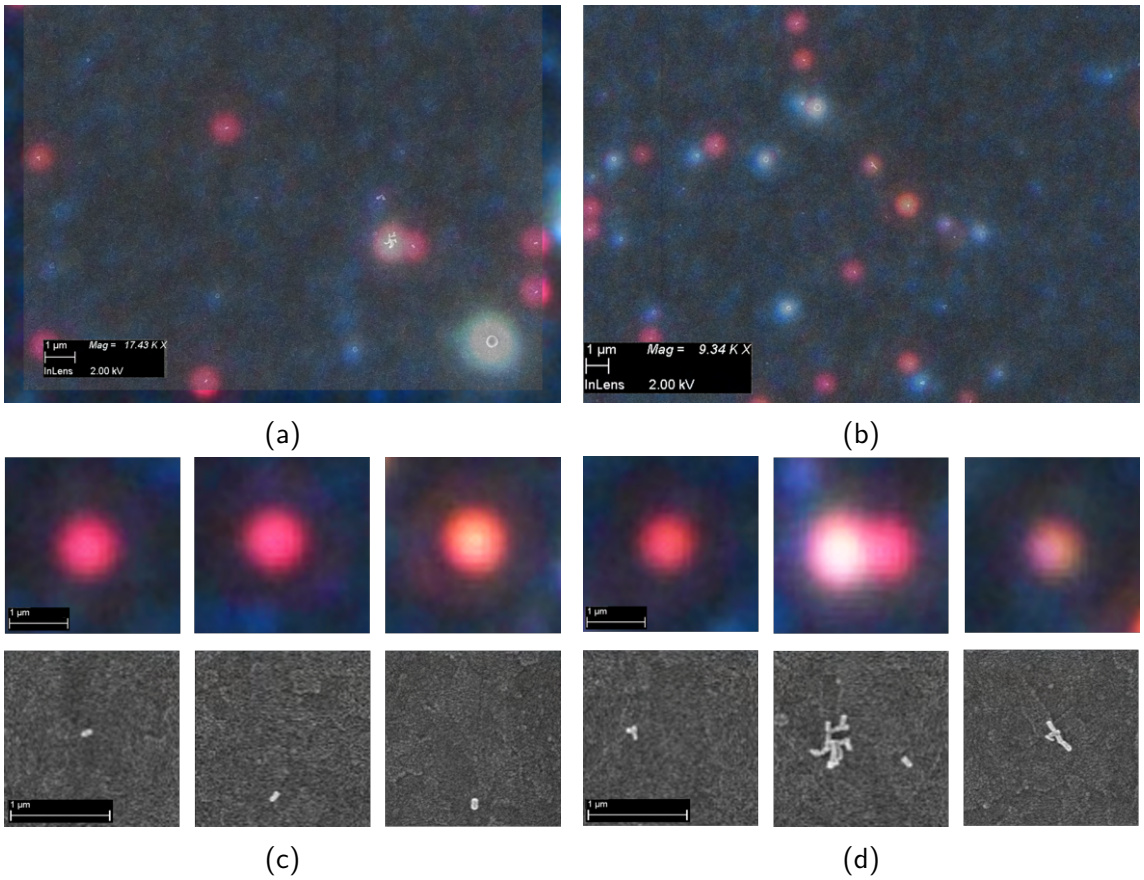

Figure 3.8: **a)** and **b)** show a dark-field image of DH15 GNRs on ITO, which is overlaid by the corresponding SEM recording for comparing the colour with the appearance of the scattering object. **c)** Dark-field and SEM images of single GNRs from the pictures above. All dark-field respectively SEM images have the same magnification. **d)** Dark-field and SEM images of GNRs clumped together also from the pictures above. Changes in colour could either be cause by variations of the shape of single particles or by clumping.

4 Data Analysis

To analyse and compare the recorded data, they had to be corrected first. In this processes background effects and artefacts were minimized and suppressed. The corresponding methods are presented in Section 4.1 including additional correction processes for some of the data to further reduce edge artefacts.
For investigating possible charge transfer comparison criteria in form of physical quantities are necessary. For this purpose the energetic position of the longitudinal localised surface plasmon resonance (LSPR) and the full width at half maximum (FWHM) were chosen. The longitudinal LSPR is in the following only referred to as LSPR. To determine these quantities the data were fitted with a Lorentzian function. The details regarding this procedure are discussed in Section 4.2. Since the data of GNRs on GaN were particularly difficult to process because of a bad signal to noise ratio there is with Section 4.3 a separate chapter showing the corresponding correction procedure. The evolution of the LSPR energy during the photocharging was not only detected but should also be compared with the expectations from literature. Therefore the capacitor model introduced in Section 2.5 was applied. The fitting is discussed in Section 4.4 together with further corrections of microscope artefacts. Lastly, a statistical test, the Mann–Whitney U test, is introduced in Section 4.5 to test on the similarities between two different distributions.

4.1 Correcting

Background and Reference Correction. At first, the scattering spectra of the single GNRs $data_{raw}$ (Figure 4.1a) were corrected using the background Bg (Figure 4.1b) and reference spectra Ref (Figure 4.1c):

$$data_{corr} = \frac{data_{raw} - Bg}{Ref - Bg}. \tag{4.1}$$

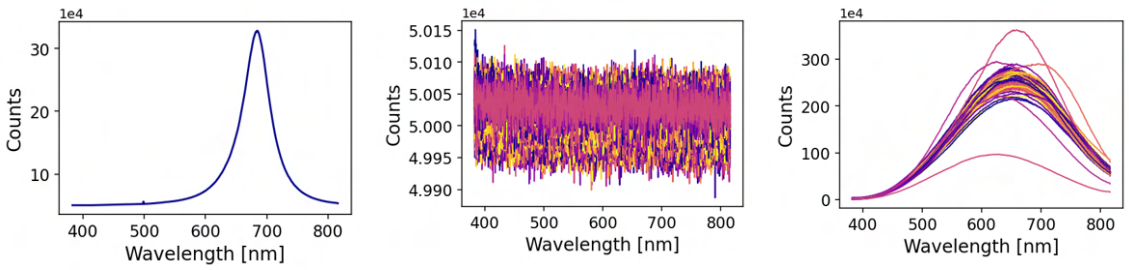

(a) (b) (c)

Figure 4.1: The **a)** raw data were corrected by **b)** the background and **c)** the reference spectra.

As explained in Section 3.4 the single particle spectra were recorded with a horizontal height of 50 rows, while the segments for the background and reference measurements include just 5 rows. Therefore, the segments corresponding to the individual particle spectra must be identified and gathered. This was done for every single particle spectrum. The individual adjusted background and reference spectra are employed for correction. In order to correct the DH16 data reference and background spectra of DH15 on ITO "after 2x SEM" were used and for correcting of DH15 on ITO "after 1x SEM" the spectra of DH15 on ITO "before SEM" utilised. Since the reference spectra show a similar behaviour in every dataset, it can be assumed, that the DH16 and DH15 on ITO "after 1x SEM" data were not distorted significantly by using another background and reference spectrum.

Empty Measurement Correction. Since during experiment B and C an additional spectrum of an empty spot was recorded together with each measured nanoparticle, the corresponding particle data $data_{corr_{GNR}}$ were also corrected by the empty spectra $data_{corr_{empty}}$ to further reduce the influence of background effects following

$$data_{corr2} = data_{corr_{GNR}} - data_{corr_{empty}}. \tag{4.2}$$

The benefit and result of this correction is visualized in Figure 4.2. The applied method reduces significantly edge artefacts and corrects the base line.

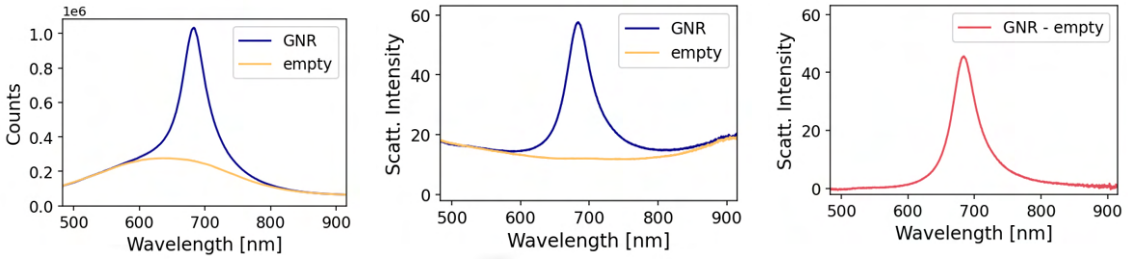

(a) (b) (c)

Figure 4.2: **a)** Raw data of the scattering spectrum of a GNR and the empty substrate. **b)** Both spectra were corrected using the background and the reference spectra but there are still visible edge artefacts. **c)** These were removed by subtracting the empty spectrum from the GNR's data.

4.2 Fitting

3 The data are going to be analysed regarding environment and charge dependent modifications of the LSPR energy and the FWHM. These parameters can only be determined imprecisely directly from the data, as the data were recorded for discrete wavelengths. Therefore the data were fitted and the parameters were obtained from the fit. To improve the conditions for fitting, the data were cropped around the plasmon resonance maxima to get rid of edge artefacts and to centre the maximum.
A localised surface plasmon is an collective oscillation of the conduction electrons relative to the positively charged ionic cores. This displacement of charges creates a restoring force acting in the opposite direction. Therefore the LSP can be interpreted as a damped

harmonic oscillator with an equation of motion of the contributing electrons similar to the equation of the core electrons (Equation 2.11) [13, 50]. Thus, we find the polarisation α to be proportional to

$$\alpha \propto \frac{1}{(\omega^2 - \omega_0^2)^2 + \gamma^2 \omega_0^2}, \tag{4.3}$$

which is similar to the Lorentzian function. Since this model is based on a frequency dependence the x-axis was converted from wavelength [nm] to photon energy [eV]. To correct remaining background effects a linear term was fitted in addition to the Lorentzian model.

Lorentzian function:

$$f_{lor}(x) = \frac{A}{\pi} \frac{\sigma}{(x-\mu)^2 + \sigma^2} \tag{4.4}$$

with $x = \omega$, A as the amplitude, $\mu = \omega_0$ as the centre and $\sigma = \gamma/2$ as the half width at half maximum [51].

Linear function:

$$f_{lin}(x) = mx + b \tag{4.5}$$

with m as the slope and b as the intercept [51].

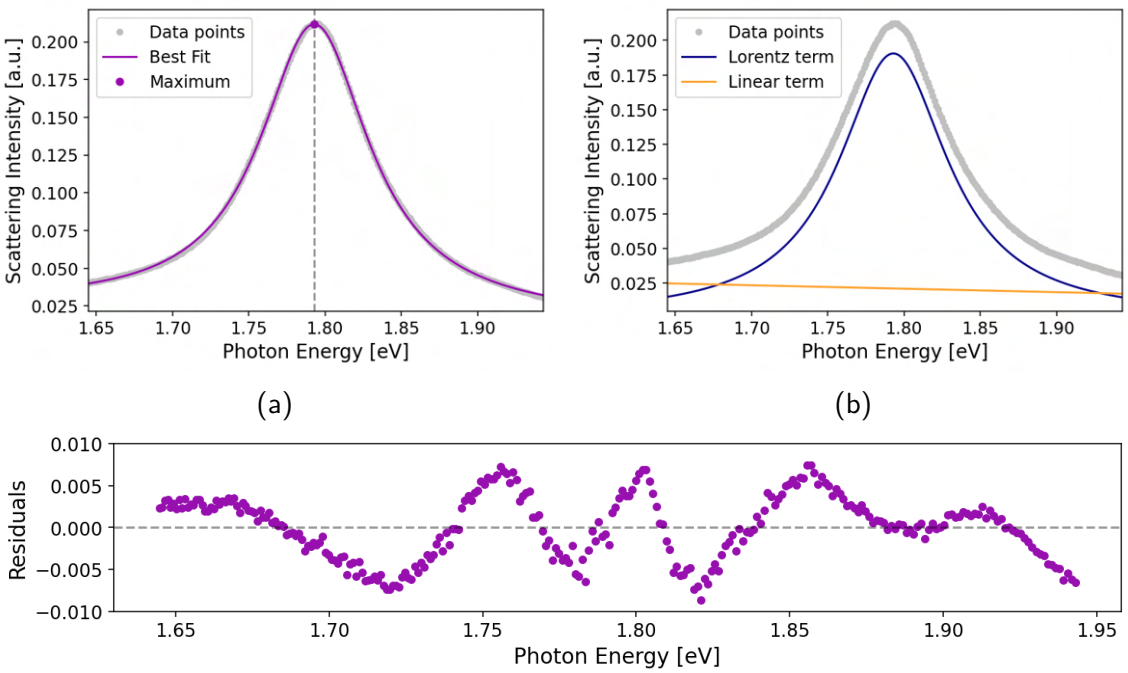

Figure 4.3: An exemplary scattering spectrum of a single MS07 GNR on glass was chosen to show **a)** the best fit, **b)** the corresponding linear and Lorentzian terms and **c)** the calculated residuals. The small pattern can be neglected, since its intensity is less then 1% of the resonance maximum.

A best fit and the corresponding individual terms can be exemplary seen in Figure 4.3a and 4.3b. From this best fit the maximum position corresponding to the LSPR energy,

and the FWHM could be determined. To evaluate the quality of the fits, the normalised residuals were calculated using

$$res = (data_{corr} - fit)/data_{corr_{max}}. \tag{4.6}$$

An example is show in Figure 4.3c. Ideally, the residuals should not display any patterns, as they would highlight a systematic shift of the fit compared to the real data.

4.3 Kernel Smoothing

A direct fitting of the single particle data of MS70 GNRs on GaN was not insightful due to the bright background and additional intensity oscillations of the signal.

Interference in Thin Films. GaN as well as ITO were applied as a layer with a thickness in the range of nanometres on a substrate. Thus, they can be referred to as thin films and because of their small dimension in z-direction they show characteristic optical features. When a thin layer is irradiated, a fraction of the incoming light is reflected by the upper surface, while the remaining part is transmitted. When this transmitted light approaches the lower interface both effects happening again. The unique aspect is, that light reflected at the lower surface interferes with the beam reflected at the upper interface. Depending on the thickness of the film and therefore of the difference in phase, and on the wavelength, this interference can either be constructive or destructive [52, 53, 54].
This reflection is not limited to one time at each surface. Instead the incoming light can be reflected multiple times at both interfaces. This causes visible interference on both sides of the thin film [53, 54]. In the transmission spectra this effect occurs as oscillations in the intensity of the signal depending on the wavelength (Figure 4.4).

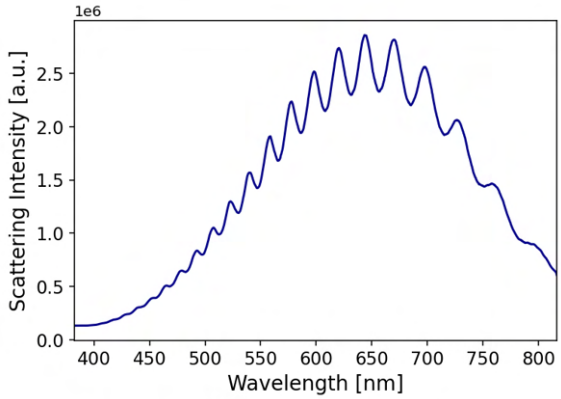

Figure 4.4: Thin film interferences result in wavelength-dependent oscillations in the transmission spectra. These data were recorded on an ITO-substrate.

These oscillations due to interference in the GaN layer are visible in the recorded dark-field data. Due to the high background scattering, the relative intensity of the LSPR peak of a nanoparticle compared to the background is low and appears in similar magnitude as the interferences. If the data are fitted directly, the resulting function is highly affected

by the thin film oscillations (Figure 4.5a). This can influence both the position of the maximum as well as the whole shape of the fit and, consequently, the FWHM.

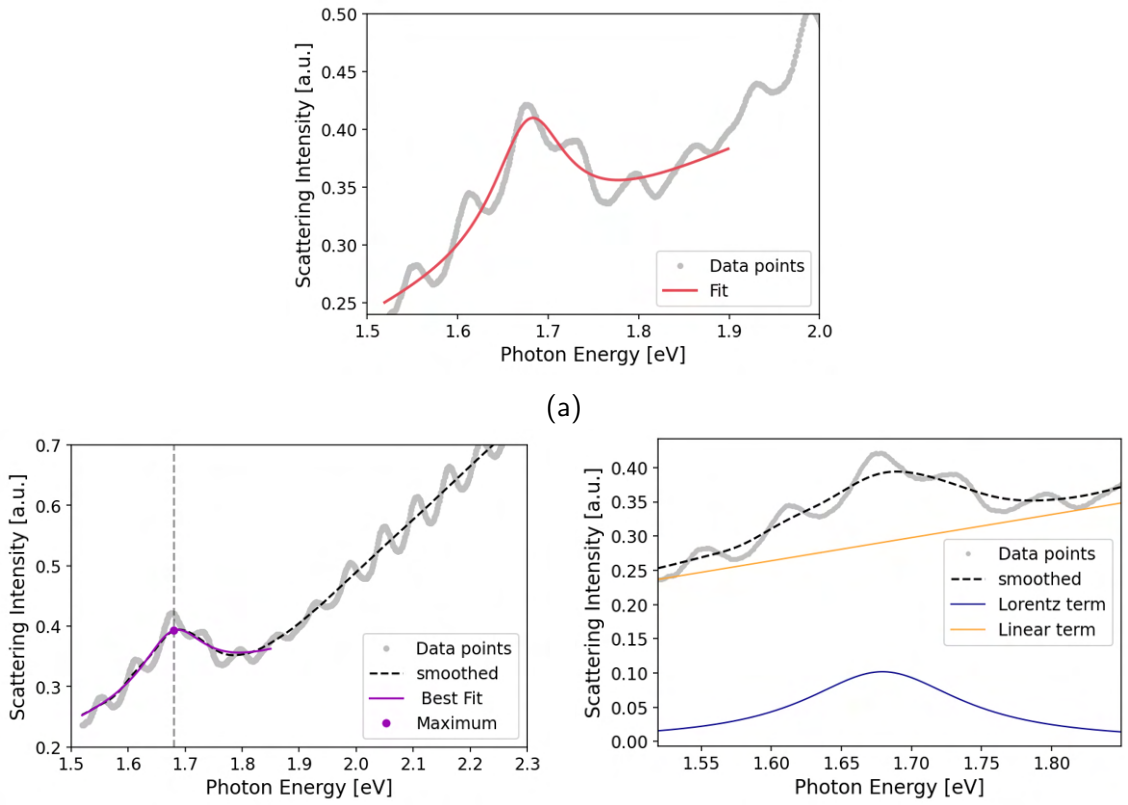

Figure 4.5: The data of MS07 on GaN need to be smoothed before fitting. An exemplary scattering spectrum of a single MS07 GNR on GaN was chosen to show the effect of the smoothing. **a)** One can see the original data fitted directly compared to **b)** the smoothed graph and its best fit. In **c)** the corresponding linear and Lorentzian fit components are presented.

To reduce the influence of the interferences in thin films so-called kernel smoothing was applied before fitting. This is a moving average smoothing technique in which the observations are locally averaged using a weighting function, the kernel. In our case a Gaussian kernel was used, which can be described by

$$K(x^*, x_i) = \exp\left(-\frac{(x^* - x_i)^2}{2 \cdot \sigma^2}\right). \tag{4.7}$$

Here, x_i refers to centre of the of the Gaussian normal distribution and the datapoint which is going to be adjusted. For smoothing the whole graph, x_i is moving through all datapoints [55]. The smoothing parameter σ is the bandwidth of the weight function [55]. It was chosen in a way, that the resulting values balance between the maxima and minima of the oscillations. $\sigma = 25$ was found to be a reliable choice to correspond to the phase of the oscillations. Afterwards the smoothed data were fitted (Figure 4.5b and 4.5c).

4.4 Capacitive Charging Fit

Correction and Fit of LSPR Shift. To better visualise and analyse the time evolution of the LSPR energy it was plotted as resonance shift over time. The shift is defined as the difference between the time-resolved data and its first measured datapoint. The time recording starts with the measurement of the first spectra. The evolution of the LSPR energy is exemplarily shown for data 2 in Figure 4.6a in blue.

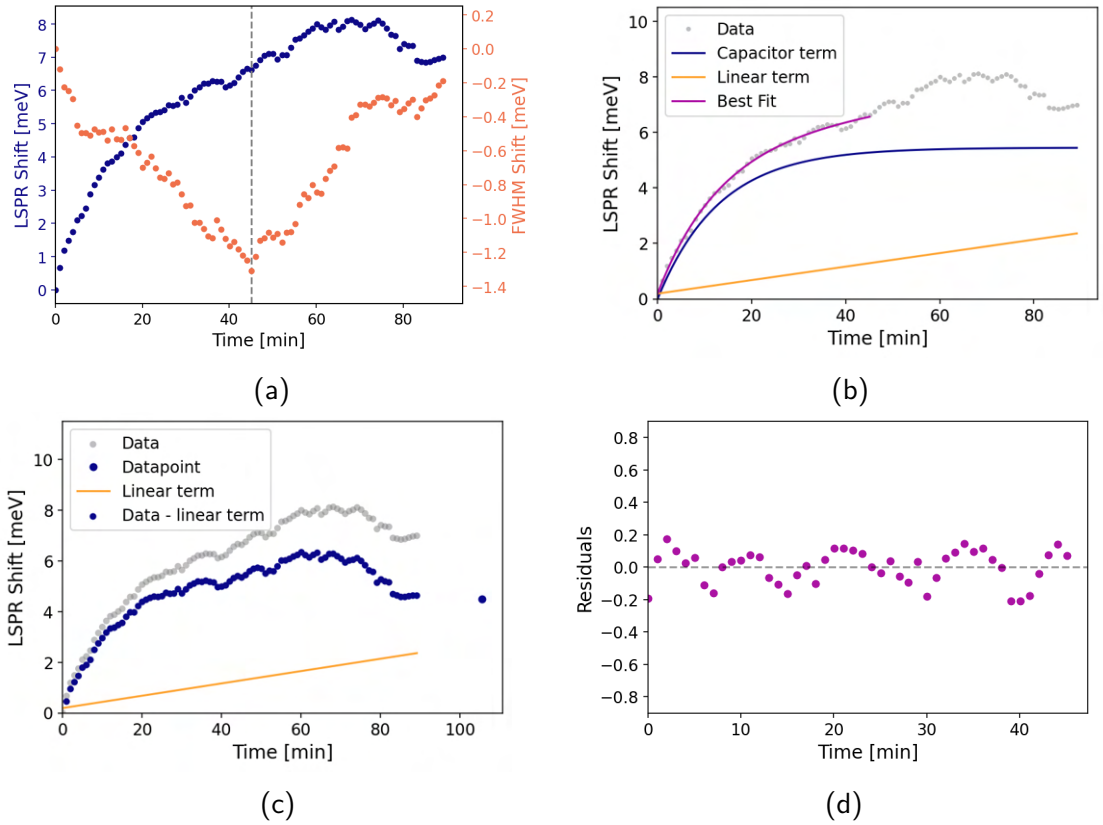

Figure 4.6: **a)** The LSPR energy as well as the FWHM shift over time. The FWHM shift shows a change point highlighted by a dashed line. **b)** The shift of the LSPR energy follows the sum of a capacitor and a linear term. Only the first half of the data was fitted to reduce the influence of later appearing artefacts. It was interrupted by the time where the FWHM shift changes. **c)** The background correction via the linear term resulting from the best fit is validated using the refocused datapoint. After the correction, the last point of the time-resolved data aligns with the refocused datapoint. **d)** The best fit is reviewed using its residuals.

This resonance shift can be interpreted as a capacitive charging of the nanoparticle as it was discussed in Section 2.5 [1]. Additionally, a linear background could be identified. It was attributed to the continuous defocussing of the nanoparticles which was already mentioned in Section 3.4.2. The underlying cause of this phenomenon could not be fully identified, but it may be due to thermal expansion of the setup or the sample whilst illuminated. Thus, the charging process was fitted as the sum of a linear term (Equation 4.5) and a capacitor component (Equation 2.58). Figure 4.6b shows the data as gray

dots together with their best fit in purple and both fitting components in blue and yellow. The linear background was verified utilizing the refocused datapoint which was measured after the time-resolved data. We assume this datapoint to show the real data as the influence of the defocussing was neglected via refocussing. As it is shown in Figure 4.6c the LSPR shift evolution aligns perfectly with the refocused datapoint after the linear correction was subtracted. Since no refocussed datapoint was recorded for particle 1, the correction of its dataset can not by verified.
In addition to the linear background other deviations appeared after a certain time, which did not suit the capacitive charging and distorted the fitting. Since they could not be described by a simple model as a linear fit, they were excluded from fitting. Consequently, the best fit appears interrupted in Figure 4.6b. In order to determine the optimal stopping point in time the shift of the FWHM was considered. Its evolution is plotted in Figure 4.6a as orange dots. It shows a striking behaviour. At first the FWHM narrows approximate linear in time before it suddenly broadens again. This change point between the two linear behaviours is considered as the stopping point for the charging fit. It is highlighted in Figure 4.6a with a gray dashed line. The small residuals in Figure 4.6d support the procedure for fitting.
Data 3 shows strong deviations from the expected behaviour, and no clear change point could be identified in the FWHM data. The linear function was therefore first calculated separately, in the sense that the last point of the time-resolved measurement was forced to align with the refocused point. After this, the capacitive behaviour was fitted to the already corrected data. The graphs of the other data including the fitted curves and the corresponding residuals, similar to those shown in Figure 4.6, can be found in the appendix in Figure 7.11.

Correction of FWHM Shift. It has to be assumed that the defocussing had not only an impact on the resonance position but also on the FWHM. Since we have no reference for an expected behaviour we can only utilize the recorded data. We consider the refocused datapoint as reliable in analogy to the correction of the LSPR energy. Since no such datapoint was recorded for particle 1 the corresponding FWHM shifts can not be corrected.
The FWHM shifts of data 2 and 4 show a similar behaviour and were therefore corrected using the same procedure. The FWHM shifts seem to consist of two linear functions with the slopes m_1 and m_2. We want to determine a linear correction function similar to the focus correction of the resonance position. By equating the last datapoint of the time-resolved measurement with the refocused datapoint as it applied for the LSPR shift we obtain a behaviour that appears inauthentic. Therefore equation to determine the slope of the correction function $m_{c_{2,4}}$ was found to be

$$m_{c_{2,4}} = (p_3 - p_1 - m_2 * (T_3 - T_1))/T_3 \tag{4.8}$$

with

$$m_2 = \frac{p_2 - p_1}{T_2 - T_1}.$$

Here, $(p_1|T_1)$ determines the change point, $(p_2|T_2)$ the last point of the time-resolved data and $(p_3|T_3)$ describes the refocused datapoint. The procedure is illustrated in Figure 4.7a utilizing data 2.

The FWHM shift of data 3 appears similar to a single linear function and was therefore treated as such. To determine the real slope without the influence of the changing focus a correction function has to be found with the slope m_{c_3}. Utilizing the last datapoint of the time-resolved data $(p_1|T_1)$ and the refocused datapoint $(p_2|T_2)$ the expression for determine m_{c_3} results in

$$m_{c_3} = \frac{p_2}{T_2} - \frac{p_1}{T_1}. \tag{4.9}$$

This is illustrated in Figure 4.7b.

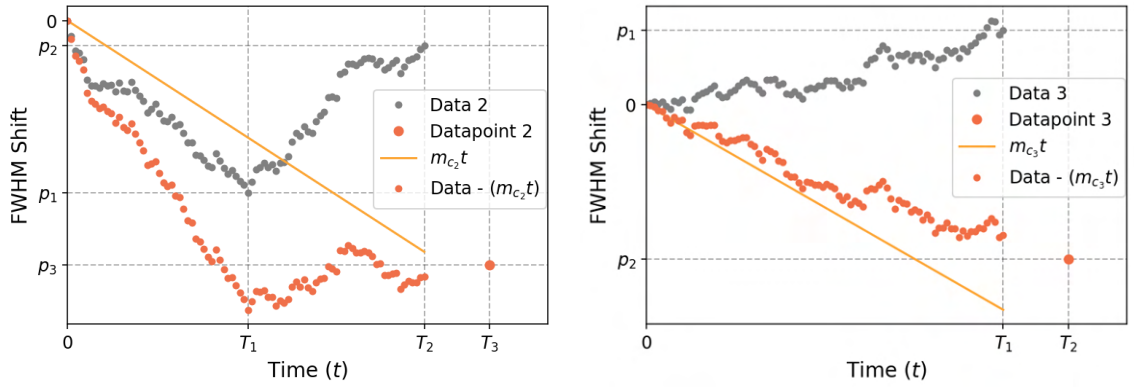

(a) (b)

Figure 4.7: Illustration of the FWHM shift correction with a linear function **a)** of data 2 and 4, exemplarily shown for data 2, and **b)** of data 3.

4.5 Mann–Whitney U Test

For a better evaluation between two datasets we want to statistically test for differences in data distributions. For this purpose, the Mann–Whitney U test is to be introduced here. It is a nonparametric statistical test whether a null hypothesis needs to be kept or rejected in place of an alternative hypothesis. The null hypothesis assumes that two different datasets origin from the same distribution while the alternative hypothesis assumes that they were not produced by the same data generating mechanism. As a crucial quantity we compute the p-value $p \in [0, 1]$ of the test. As threshold for an acceptable false rejection of the null hypothesis we chose $\alpha = 0.1$, also known as the α-error error of the first kind. For $p > 0.1$ the null hypothesis can not be rejected and it has to be assumed true, whereby for $p \leqslant 0.1$ the null hypothesis has to be rejected and the alternative hypothesis needs to be assumed [56].

5 Results and Discussion

This work focuses mainly on the interaction of gold nanoparticles with their environment with a major interest in the transfer of charges. For this purpose the optical response of the GNRs is analysed utilising the LSPR energy, which is sensitive to charge accumulation and changes in the electrostatic environment, and the FWHM as an indicator for damping effects. As already introduced three different experiments were performed. The corresponding data and results are going to be presented, analysed and discussed in this chapter.
At fist, the interaction between GNRs with their substrate is investigated in Section 5.1. Three different kind of nanoparticles were used and first measured on a glass substrate. Two of them were afterwards also recorded on an ITO respectively GaN substrate to compare the influence of this conductive and semiconductive materials to glass as an dielectric material. This experiment was performed in order to detect CID, which is an indication that PICT could occur as well.
Thereafter in a second experiment the electrostatical environment of the particles was modified by changing the pH value of the surrounding media. It was of interest to understand how the optical response of the GNRs is influenced by alterations in the electrostatic interaction with the environment. In this context, the behaviour of the same individual particles at different pH values was to be investigated. Since the experimental procedure for measuring the evolution of single nanoparticles was challenging not only the development of the LSPR and FWHM per nanoparticle was analysed but also the behaviour of several particles per pH value.
The last Section 5.3 discusses the accumulation of negative charges on single nanoparticles during irradiation with a laser. This experiment was successfully performed on four single GNRs under slightly variating conditions. Therefore, the charging behaviour is discussed in general and, in particular, regarding the differences between the recorded datasets. The obtained results were additionally compared with the expected behaviour known from literature [1]. All data presented and analysed within this chapter were preprocessed using the techniques which were introduced in the former section.

5.1 GNRs on Different Substrates

5.1.1 GNRs on Glass

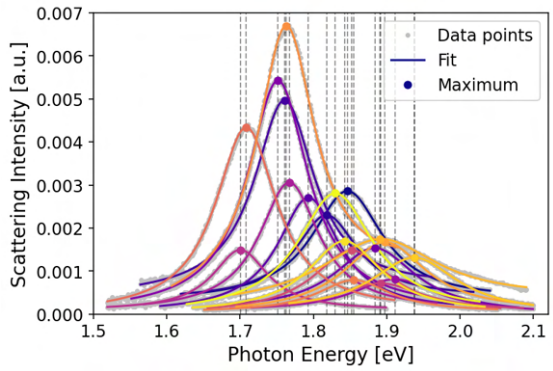

(a) **DH16** Best Fits

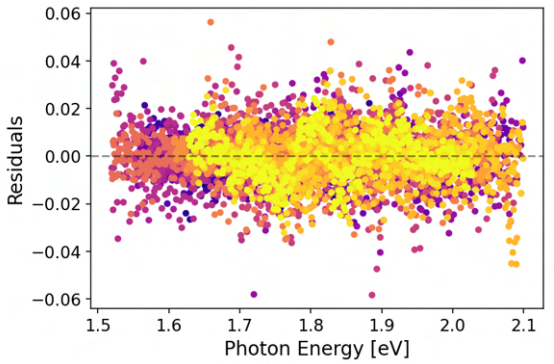

(b) **DH16** Residuals

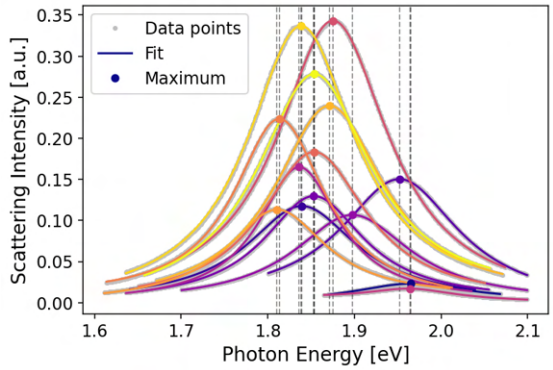

(c) **DH15** Best Fits

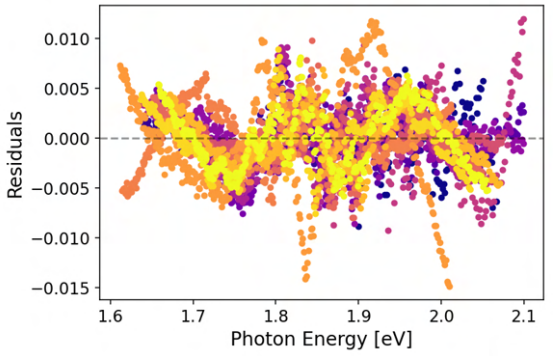

(d) **DH15** Residuals

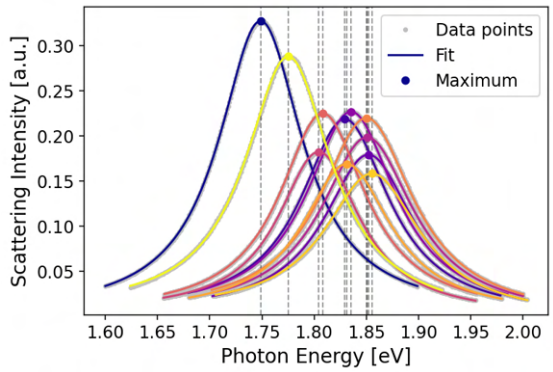

(e) **MS07** Best Fits

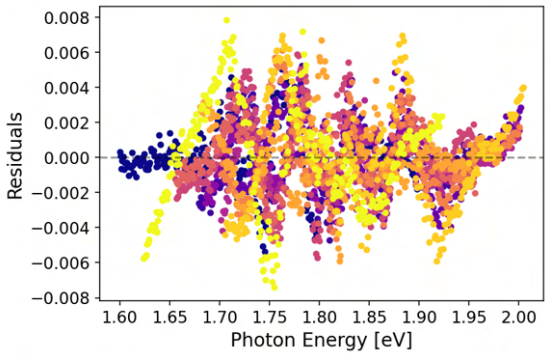

(f) **MS07** Residuals

Figure 5.1: **a), c), e)** The single nanorod scattering spectra can be fitted with the Lorentzian model. **b), d), f)** The corresponding residuals help to quantify the quality. The scattering intensity of all particles on glass is high compared to the background, therefore the fitting works well.

The GNRs were measured first on a glass substrate. Since no scattering occurs in this substrate, the background appears black and the scattering intensity of the GNRs is high compared to the background (Figure 3.1a). Thus, all of the data show a clear and high intense signal of the longitudinal plasmon resonance which makes them easy to correct

and fit. In Figure 5.1 the recorded and corrected data can be seen together with their Lorentz-fits in the same plot and the corresponding residuals in the plot on the right hand side. It is already visible by eye that the Lorentzian model is a good expression for the behaviour of the plasmon resonance. The residuals are small and only minor patterns remaining, which are negligible since they are less than 1% of the resonance maxima.
Using these fits the energetic position of the LSPR and its FWHM can be determined. Although we could express the peak height as well, this parameter is not comparable because not all data were recorded under the same and optimal conditions as explained in Section 3.4.2. Nevertheless, this should have neither an impact on the position of the maximum nor on the FWHM.

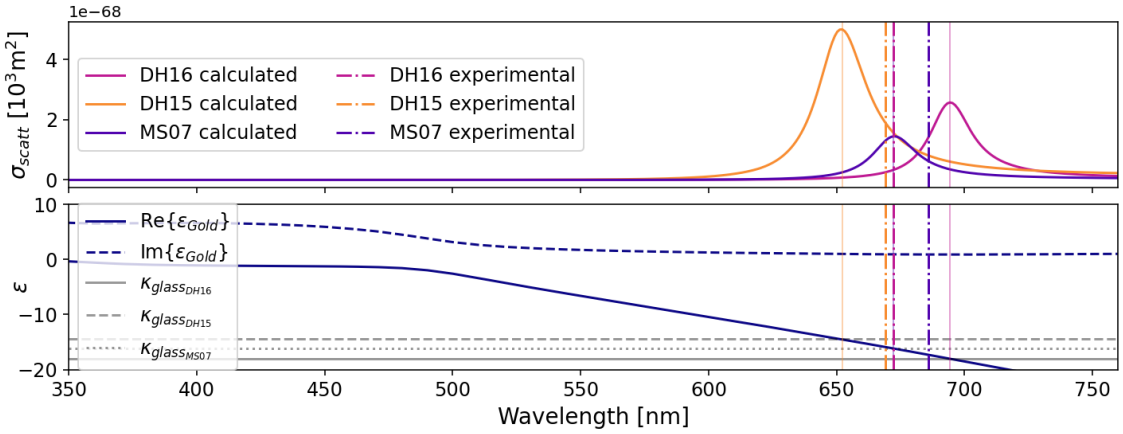

Figure 5.2: The theoretical scattering spectra can be calculated with help of Re$\{\varepsilon_{Gold}\}$ and the permittivity of the surrounding medium. The position of the longitudinal LSPR maxima is determined by the intersection of Re$\{\varepsilon_{Gold}\}$ and $\kappa_{glass} = (1 - 1/L_a)\varepsilon_{glass}$, with $\varepsilon_{glass} = 2.3$ [16] and the size of the GNRs from Tabular 3.1. The intensity of the transversal LSPRs are two orders of magnitude smaller then the longitudinal LSPRs and are therefore not visible. The data for Re$\{\varepsilon_{Gold}\}$ and Im$\{\varepsilon_{Gold}\}$ were taken from Reference [57] and linear interpolated. The medians of the experimental datasets differ slightly from the calculated LSPR energies.

We will first consider the LSPR energy and compare it to the theory which was derived in Section 2.3. The LSPR can be described by the scattering cross-section. It was theoretically calculated via Equations 2.53a and 2.54a. Furthermore, the LSPR energy can be determined by the Fröhlich condition (Equation 2.55) and depends on the permittivity of the surrounding medium and the aspect ration of the GNR. This relation is illustrated in Figure 5.2. The lower plot shows the real part Re$\{\varepsilon_{Gold}\}$ and the imaginary part Im$\{\varepsilon_{Gold}\}$ of gold. We know from the Fröhlich condition that the position of the plasmon peak is determined by the interface of the real part of gold with $(1 - \frac{1}{L_a})\varepsilon_{med}$, whereby L_a depends on the aspect ratio.
We are considering the particles as enclosed by glass with $\varepsilon_{glass} = 2.3$ [16]. This is only an approximation because the GNRs were placed on a glass substrate and covered with a glass coverslip but parts of the particles were still exposed to air. Nevertheless, this model appears to work sufficiently well as we will show by comparing it with the experimental data.

Using Re$\{\varepsilon_{Gold}\}$ and Im$\{\varepsilon_{Gold}\}$ taken from Reference [57] the theoretical trajectory of the LSPs were calculated and presented in the upper plot of Figure 5.2. Because all kinds of GNRs used have a different aspect ratio σ_{scatt} has to be calculated for each individually. By comparing the positions of the maxima with the intersections in the lower plot one can see that they align perfectly.
For comparing the calculated values with the measured results, the medians of the experimental datasets are presented in the figure as dashdotted lines. The median is used since it is more reliable for small sample sizes than the average. The maxima of both the calculated and experimental data are located in the same range regarding the wavelength while they should be shifted to lower wavelengths when assuming air as the surrounding medium. Thus, the assumption of $\varepsilon_{med} = \varepsilon_{glass}$ can be considered valid.
Nevertheless, there are visible differences between the calculated and experimental maxima. The experimental medians of DH15 and MS07 are shifted to larger wavelengths, whereas the experimental median of DH16 is moved to a smaller wavelength. Consequently, they are located closer together than theory predicts. This is probably due to a bias during the selection of the particles to be measured. Within one kind of particles there are still variations regarding the size and expansions. This leads to small deviations in the colour, which are similar to variations due to clumping of particles. The GNRs to be measured were chosen by colour and since experience on DH15 samples has shown which shade of red corresponds mostly to single particles, GNRs with a similar colour were preferred on the DH16 sample as well. During the measurements of MS07 a dark red colour was favoured since this corresponds most likely to single GNRs. This bias led to a visible shift compared to the theoretical data.

In Figure 5.3a the LSPR energies of the datasets for GNRs on glass are presented as a box plot with the calculated maxima of Figure 5.2 as dashed lines. Additional to the position of the medians, we get information regarding the distribution of the data. The box is defined to contain the centred 50% of the data and the median, represented by the horizontal line inside the box, divides the data into two halves with the same amount of datapoints. The whiskers have a maximal length of 1.5 times the box's length and extend to the furthest data point, which is still within this interval. Data points outside this range are presented as dots [58]. An elongated box and longer whiskers show stronger deviations from the median.
There are stronger discrepancies for DH16 to lower energies compared to the variations to higher energies while it is the opposite for DH15. This is probably due to the real distributions of the size GNRs. Following the theory there are supposed to be more DH16 GNRs with a LSPR energy below the measured median, respectively more DH15 GNRs with a LSPR energy above the experimental median. Overall, the largest variations appear within the DH16 dataset visible by the most expanded box. Whereby the MS07 dataset shows only weak deviations.
Additional to the LSPR energy the FWHM was examined (Figure 5.3b). The data of the different kind of particles are presented as a box plots to do both show the median and give an idea of the distribution. Even though the datasets may overlap, they differ significantly in position and size of the box. The median of DH16 is located in between the other two medians and this dataset shows again the strongest deviations. Especially the variations within the MS07 dataset are only weak.

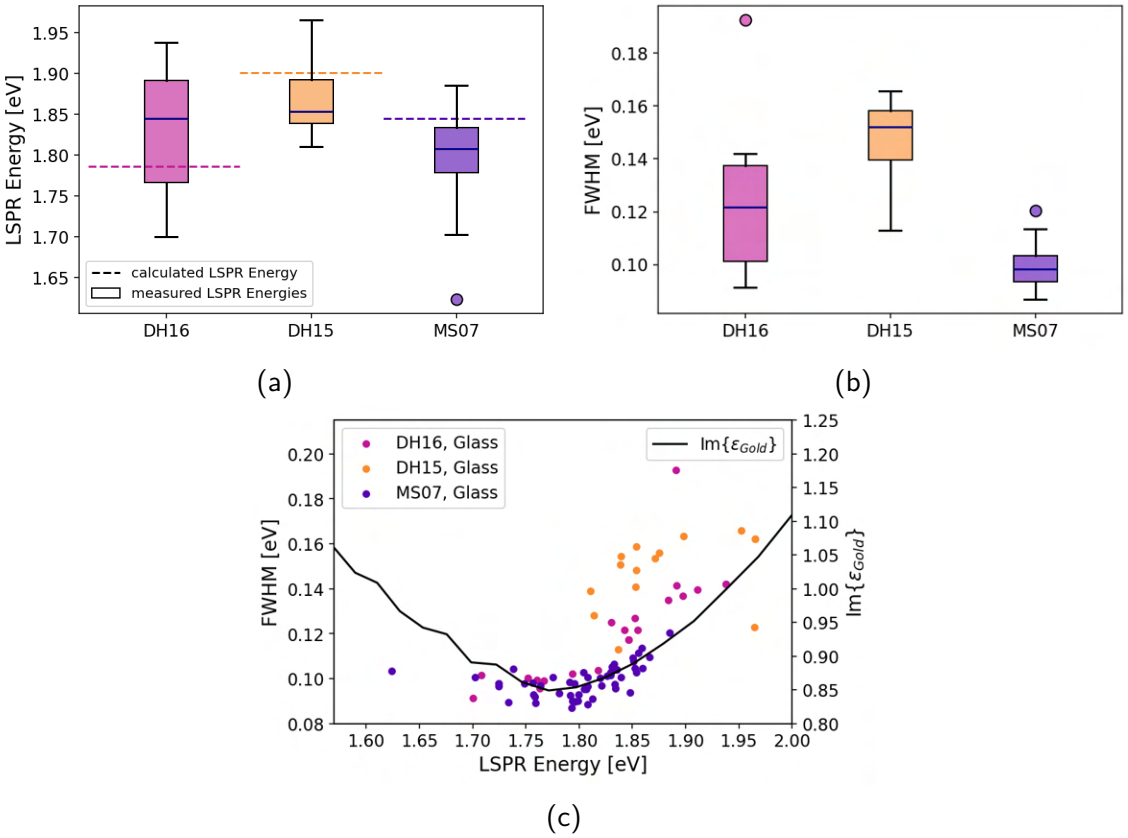

Figure 5.3: **a)** Box plot of the experimental LSPR energies of GNRs on glass. The theoretical LSPR energies from Figure 5.2 are presented as dashed lines with matching colours for the same kind of GNRs. **b)** Box plot of the experimental FWHM of GNRs on glass. **c)** The FWHM is plotted against the LSPR energy together with $Im_{\varepsilon_{Gold}}$, which represents the influence of intraband and interband transitions in gold.

An explanation can be found by considering Figure 5.3c. The FWHM is plotted against the LSPR energy. Additionally, Im$\{\varepsilon_{Gold}\}$is presented in this figure for illustration. This physical quantity displays the influence of intraband and interband transitions in gold depending on the photon energy [10]. The FWHM is a measure of the damping of the plasmon, which can be, among other things, due to interband transitions.
The figure shows that the experimental data of MS07 particles are located precisely at the minimum between Drude and interband damping. This explains both the small FWHM and the low deviations. For DH16, the energetic positions of the peaks are more widely dispersed and, in terms of energy, located at the increasing influence of interband transitions visible by the slope of Im$\{\varepsilon_{Gold}\}$. This leads to a significant rise of the FWHM within the dataset. Although the data of the DH15 particles are similar to those of DH16 in terms of LSPR energy, the GNRs have a significantly larger volume than DH16 and MS07 GNRs. With growing volume the absorption cross section increases as well, which amplifies the damping effect via interband transitions. This results in a larger FWHM at the same LSPR energy. Due to the similar volumes of DH16 and MS07, the increase in the influence of interband transitions has a similar effect. Therefore both datasets complement each other well and also exhibit a similar FWHM for particles with a similar LSPR energy.

5.1.2 GNRs on ITO

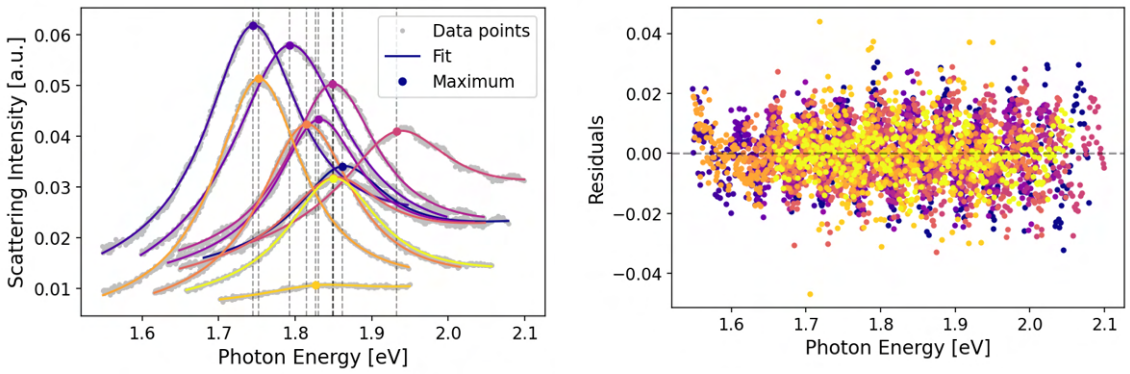

(a) (b)

Figure 5.4: **a)** The scattering intensity of DH15 on ITO compared to the background is still significant and the LSPR peaks can be fitted well using a Lorentzian model. **b)** In the residuals is the pattern of thin film resonances visible but no strong structure regarding the relevant fit.

The background scattering due to the ITO layer is significant, but there is still a high contrast compared to the GNRs' signal. Also the light scattered by ITO appears in the dark-field image manly blue, whereby the scattering maxima of the GNRs is red. This shift in the wavelength helps to distinguished the nanoparticles from background scattering. Nevertheless the scattering spectra are influenced by the ITO substrate, which leads to a reduced intensity. The corrected spectra are shown together with the corresponding fits and residuals in Figure 5.4.

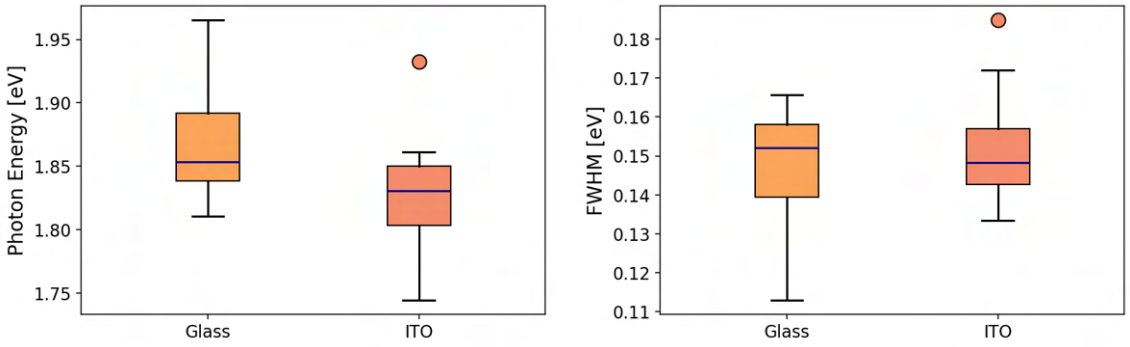

(a) (b)

Figure 5.5: DH15 on glass and ITO: **a)** LSPR energy and **b)** FWHM.

In the residuals is an oscillating structure visible. This is not due to an insufficient fit but because of thin film interference in the ITO substrate, due to the small thickness of the applied ITO layer. Since the influence on the determination of the LSPR energy and FWHM is not significant, it was not necessary to correct these intensity oscillations. In Figure 5.5a the LSPR energy is shown as a box plot for both DH15 particles on glass and ITO. Despite the medians appear to be relatively similar, the deviations are stronger in opposite energy directions. By comparing this with the experiences from

Figure 5.3a this apparent similarity could be due to the selection bias, whilst the real distributions differ more than the experimental data imply. Even without this assumption we need to assume that the two datasets originate from different distributions, because of the Mann–Whitney U test result of p = 0.0457. In opposition to this the FWHMs of both datasets, shown in Figure 5.5b, appear to have similar values and there could no statistically significant difference be shown between these distributions (p = 0.805).

5.1.3 MS07 on GaN

The GaN substrate showed a high intense scattering as discussed in Section 3.2. Due to this bright background, it was difficult to identify nanoparticles during the measuring process and it was challenging as well to extract the plasmon resonance whilst correcting the data. The related peak has a low contrast compared to the background scattering. Additionally, the measured data show again an oscillating structure similar to the data in Section 5.1.2 on the ITO substrate. Here, the interferences in thin GaN film appear much more dominant compared to the low intense LSPR than on ITO. Both effects cause a hardly identifiable plasmon peak. Furthermore, due to the nearly invisible GNRs in the dark-field image it was difficult to rediscover the same particles using the SEM. Consequently, not all particles could be verified as singe. The collages of the SEM and dark-field images are shown in Figure 7.5.

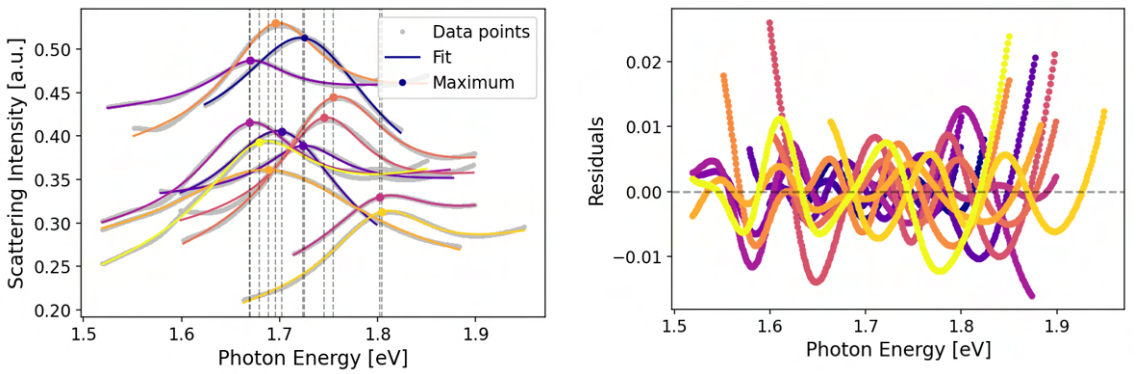

(a) (b)

Figure 5.6: **a)** The scattering intensity of MS07 on GaN compared to the background and thin film interferences is low and the trajectories of the scattering cross-section can only be fitted after smoothing the data. **b)** The residuals show significant deviations and patterns.

Due to the additional preprocessing, which was described in Section 4, it was possible to achieve a useful fit with the Lorentzian model (Figure 5.6a). Nevertheless, it is indicated by the high residuals relative to the maximum of the peak that the fit is not optimal (Figure 5.6b). The fitting parameters, which are going to be used in the analysis serve therefore merely to identify trends and not to draw qualitative conclusions.
Similarly to the previous section, the differences of the MS07 GNRs on glass and GaN are to be evaluated regarding the LSPR energy and the FWHM (Figure 5.1.3). In both cases the datasets show statistically significant differences (LSPR energy: $p < 0.001$, FWHM: $p < 0.001$). The LSPR energy of GNRs on GaN is shifted to lower energies whilst the FWHM on GaN is on average slightly above the values of GNRs on glass.

The shift of the LSPR energy is not surprising and a result of the different permittivity of GaN compared to glass. The variation of the FWHM is more interesting because it indicates an enhanced damping of the LSP due to CID.

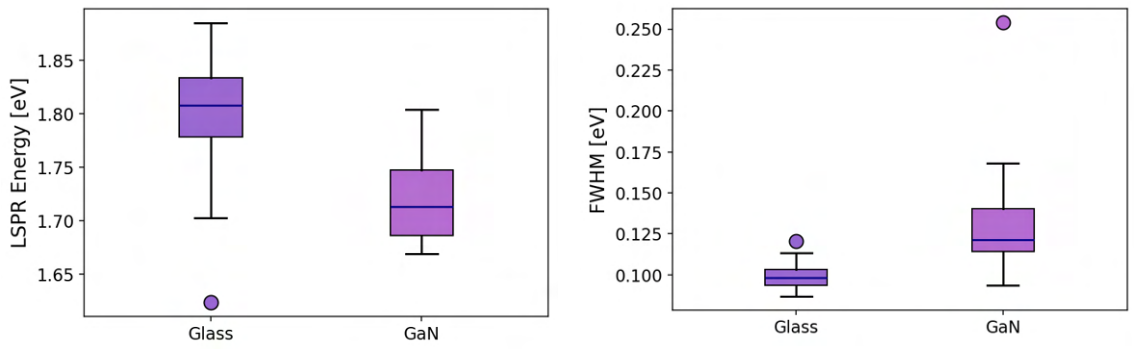

(a) (b)

Figure 5.7: DH16 on glass and GaN: **a)** LSPR energy and **b)** FWHM.

5.1.4 Combined Discussion.

For further investigation and explanation the graph in Figure 5.3c was expanded by adding the datasets for GNRs on ITO and GaN and is displayed in Figure 5.8. These new data are represented by cross-shaped markers.

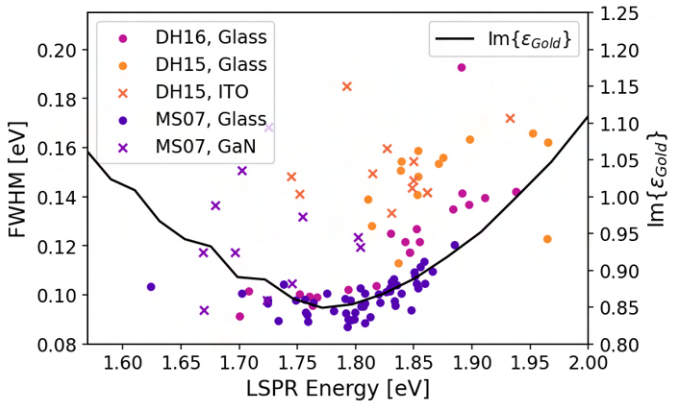

Figure 5.8: Figure 5.3c has been supplemented by the datasets for GNRs on ITO and GaN, represented by cross-shaped markers.

It is noticeable that the non-glass data do not follow Im$\{\varepsilon_{Gold}\}$ closely. They tend to be larger than the data recorded on glass. Especially for MS07 this effect is clearly visible. For DH15 particles the FWHM on ITO and glass is comparable. However, the shift in the LSPR energies takes on a new relevance here. Due to this difference in the resonance energies, the datapoints of the particles on ITO are located in the range of the minimum of Im$\{\varepsilon_{Gold}\}$. Thus, the interband transitions, which cause a broadening of the FWHM of DH15 on glass, are less relevant here. Instead, other damping mechanisms such as CID have an impact here. For particles on GaN there is a clear difference of the FWHM of GNRs with a comparable LSPR energy. This implies that further effects, such as CID appear to be contributing here as well.

5.2 GNRs at Different pH Values

We investigate the behaviour of the LSPR of a GNR regarding changing electrostatic interactions with the environment due to an increasing concentration of H^+ ions in solution. This is represented by a decreasing pH value of the surrounding solution. The plots of the scattering spectra together with the corresponding fits and residuals can be found in the appendix in Figure 7.6 and 7.7.

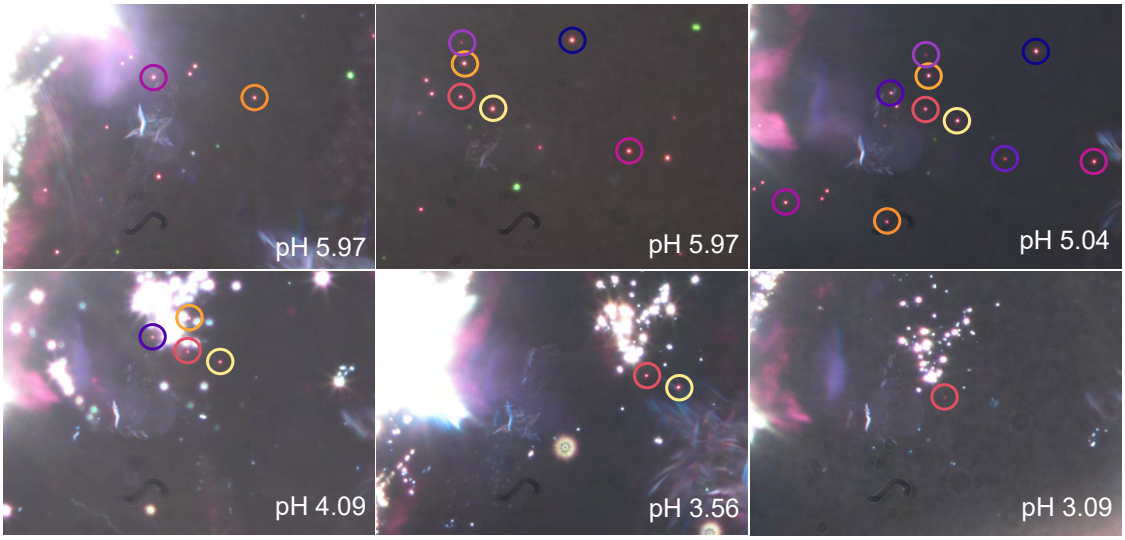

Figure 5.9: One can see exemplarily the evolution of sample 2 during changing the pH value. Same particles are marked with the same colour. The corresponding pH value can be found in each image whereby the first two images in the first row show two spots close to each other with the same pH value. The third image covers all particles from the first two pictures.

A central challenge of the experiment and recording the data was to observe the same particles for all different considered acidic solutions as the rinsing of the substrate in between measurements was likely too invasive. While most GNRs could be located again after the first washing, many seemed to detach after the second one. The development of dataset 2 for an decreasing pH value is shown in Figure 5.9. A similar image series for dataset 1 can be found in the appendix in Figure 7.8. The detachment of particles is not only a problem during the attempt to measure the complete evolution of an individual particle but makes it also impossible to record confirming SEM images afterwards. Thus, most of the GNRs analysed in this section were not verified to be single particles. This experiment was carried out towards the end of experimental phase of this work and, based on experience, single particles were most time reliably identified using the dark-field image. Accordingly, the GNRs measured were treated as if they were single although it could not be confirmed for all of them. Another problem is the accumulation of dirt on the sample such as dust particles which was caused by the repeatedly opening of the sample. This is clearly visible in Figure 5.9. Especially between pH 5.04 and 4.09 a significant amount of white scattering dirt particles appeared on the sample.

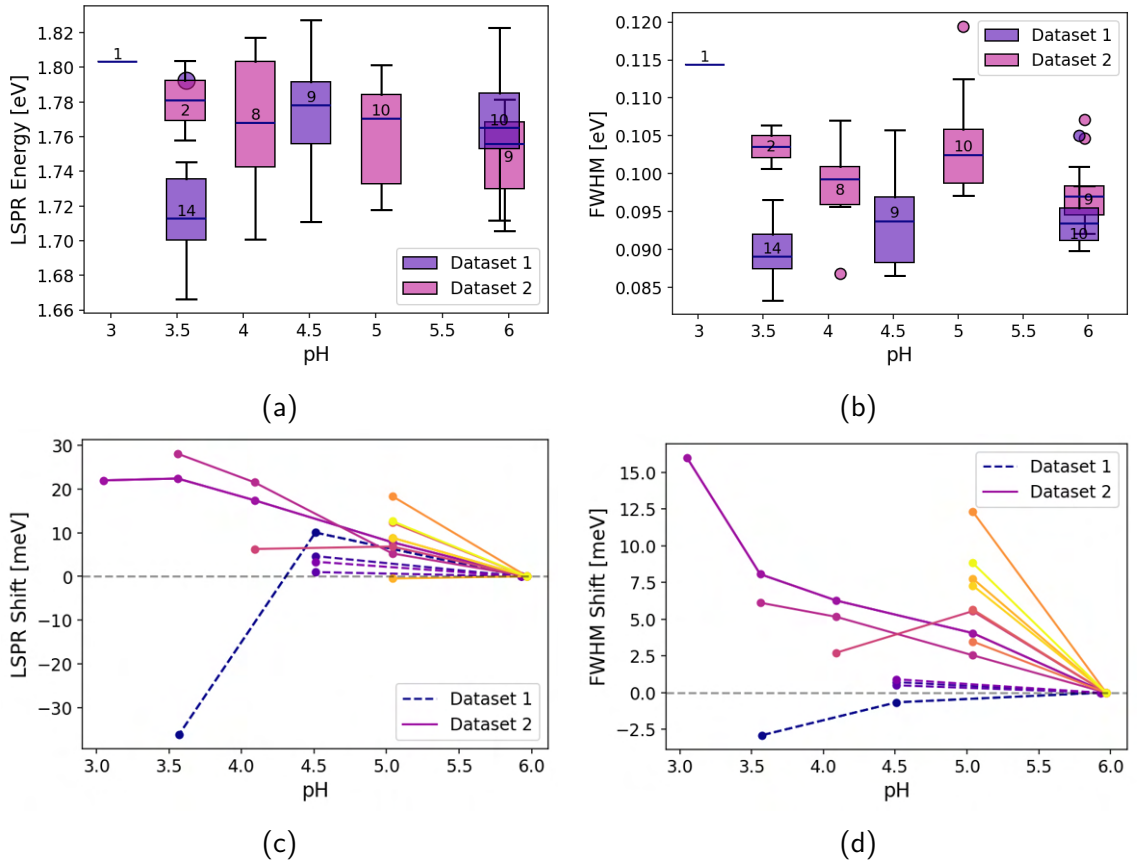

Figure 5.10: Several single GNRs were measured per pH value within two datasets. **a)** The LSPR energy of the particles is ordered per pH value presented as a boxplot. The number particles measured varies and is noted in the respective box. **b)** The corresponding FWHM is plotted as well. **c)** Additionally, individual GNRs were studied for decreasing pH values. The evolution of the particles in LSPR and **d)** FWHM is shown. Since particles detached during the experiment not the whole evolution could be recorded for all particles.

Ensembles. Initially, we combine all particles measured at the same pH value to an ensemble and compare them with each other before we focus on the development of individual GNRs. In Figure 5.10a one can see the distributions of LSPR energies of single particles sorted by pH value. Every ensemble is shown as a box plot with different colours for dataset 1 and 2. The number of particles measured by the respective pH value is displayed in the corresponding box.
Almost all data are located in the interval of 1.7 to 1.82 eV and the boxes overlap largely. When considering the medians a slight increase of the LSPR energy for a decreasing pH value is suspected. However, using the Mann-Whitney U we can not reject the null hypothesis that all particle spectra originate from the same distribution, since no statistically significant differences can be found. The only exception is the ensemble of dataset 1 at a pH value of 3.57. These data decrease suddenly compared to the other ensembles. This ensemble is with 14 measurements the largest one. Therefore, its behaviour can not be explained due to a single outlier. Since only two datasets were recorded and they differ significantly for a pH value of approximate 3.6 (p =

0.033), it cannot be determined with confidence which of the sets is more reliable. Nevertheless, we assume the lower ensemble to be the exception, because the tendency for no shift or a slight increase shown by the other ensembles is more steadily even though with less measured particles per pH value. This outlier acidic solution can be caused by contamination with chemicals leading to a red shift of the LSPR energy. Since this parameter is highly sensitive to the permittivity of the surrounding medium a contamination maybe due to a dirty vial with remains of other chemicals could lead to a strong effect such as the one observed.
By considering the FWHM in Figure 5.10b there is no steady tendency visible regarding the pH value. Instead a slight difference between the two datasets can be observed. The ensembles of dataset 2 show a greater width compared to the data of set 1. The particles from both datasets originate from the same fabrication batch therefore variations due to different shapes or sizes can be most likely rejected. It is more likely that it was caused by differences during the sample preparation. Even though the samples were produced following the same protocol the time between the plasma cleaning and the application of the GNRs may have differed by a few minutes. After the plasma treatment the surface energy of the substrate is altered which improves the attachment of the GNRs. Since this effect is only temporarily, the hydrophobic recovery is further progressed for an increased time between the plasma cleaning and the application of the nanoparticles. Consequently, the adhesion and the contact between the nanoparticles and the substrate is improved for a shorter waiting time. The FWHM provides information regarding the damping of the plasmons and a broadening as observed for dataset 2 compared to dataset 1 implies an increase of CID due to stronger interaction between the GNRs and the substrate. However, the observed variation could also be caused by a contamination of the acid in one of the samples. All solutions originate from the same stock solution. If there had initially been any contamination, it would have been transferred to all solutions used in the dataset. Since the observed difference appears predominantly in the FWHM and less in the LSPR energy a chemical contamination is unlikely since it would change the permittivity of the solution which has a great impact on the LSPR energy as well.

Individual Particles. The detachment of particles from the substrate between the measurements has a great influence on evaluating the development of individual particles. For both dataset only one single particle was successfully measured at all pH value out of 10 respectively 8 particles recorded at the first pH value. The corresponding shifts of the LSPR energies are shown in Figure 5.10c and the development of the FWHMs in Figure 5.10d. Since the measurements were performed at an decreasing pH value with pH 5.93 respectively pH 5.97 as the initial value the shift is defined accordingly. The following discussion therefore refers to a decreasing pH value and the development of the graphs should be read from right to left.
A blue shift of the LSPR energy with an decreasing pH value is clearly visible for almost all considered particles. It is noticeable that the shift is on average stronger for particles of dataset 2. In dataset 1 the sudden drop at pH 3.57 is observable, which was already discussed in the last paragraph. Considering the development of the FWHM for individual particles, the systematic difference between the datasets which was initially observed in Figure 5.10b can be confirmed. While the pH-dependent shift for particles of dataset 1 is almost negligible, all observed particles of dataset 2 show a significant broadening. Only 3 GNRs of dataset 2 were measured at more than two pH values. 2 of these show a systematic increasing FWHM for lower pH values. The FWHM of the third particle

decreases after an initial broadening. By comparing its behaviour with the corresponding LSPR energy shift, there is also no further blue shift observable for this particle between pH 5.04 and 4.09. This implies a dependency of the blue shift of the LSPR and a broadening of the FWHM. However, not all particles behave similar.

Combined Discussion. Considering the literature an observe shift of the LSPR when changing the pH value is caused by changes in attached ligands [59]. Gold as well as PVP can be assumed to be stable against weak acids as citric acid. Therefore changes due to chemical reactions of these components are unlikely. When decreasing the pH value via adding citric acid several processes may be taking place in parallel. At first, the number of H^+ ion increases but simultaneously the concentration of negatively charged citrate ions rises, which are the conjugate base of citric acid. Furthermore, the protonation of the citrate ions is pH-dependent. Thus, it is difficult to determine one specific process which causes the observed effects. Furthermore, the discrepancies between the results we obtained when considering the behaviour of multiple particles per pH value and the behaviour of individual particles at different pH values are surprising.
When bringing GNRs in solution we expect a formation of an electrostatic double layer around the particles since metal nanoparticles are slightly negatively charged due to excess electrons of the surface atoms. By decreasing the pH value the concentration of H^+ ions in solution is increased as well as the protonation of the citric ions. Both phenomena result in changes of the near field environment of the particle and variations in the electrostatic interaction between the GNR and its surrounding solution. This can cause a shift of the LPSR energy and a decreasing number of plasmon decay channels.
A simpler explanation may be provided by a changing refractive index of the surrounding solution caused by the increasing concentration of citric acid. Such a change can lead to a shift of the LSPR energy. However, this does not fully explain the observed broadening of the FWHM. Therefore, the experimental observations cannot be sufficiently explained by refractive-index effects alone. Additionally, for an increasing citric acid concentration an rising refractive index is expected causing a red shift of the LSPR energy. This contradictory to the observed blue shift.
Due to pores in the PVP layer, citrate ions can potentially reach the GNR's surface and adsorb to the nanoparticle. Because of the negatively charged adjacent molecules the charge of the particles decrease as well [60] leading to a blue shift of the LSPR energy [1, 61] when increasing the number of attached citrate molecules. The broadening could cause by a stronger CID via the adjacent molecules. However, because of the increasing protonation and therefore decreasing negative charge of the molecules for an decreasing pH value, a red shift would be expected for a constant number of attached molecules.
The observed behaviour is likely the result of a combination of these and maybe additional mechanisms rather than a single dominant effect. The results of the experiment described cannot provide a conclusive statement about the extent to which the respective processes contribute. Due to the limited scope of this work, further investigations should be considered in future work.

5.3 Photocharging of Single GNRs

Dark-field and SEM images of the observed particles can be found in the appendix in Figure7.10. For investigating the photocharging effect on single GNRs glass was chosen

as substrate. One advantage of glass is the high contrast between the scattering intensity of the particles and the background especially by comparing it with the contrast on the other substrates used. Accordingly, a good signal to noise ratio could be achieved. A second advantage is the low CID compared to the substrates as discussed in Section 5.1. Since we want to accumulate electrons on the particle, additional decay channels of the plasmon which potentially induce charge transfer to the substrate would weaken and slow down the charging effect.

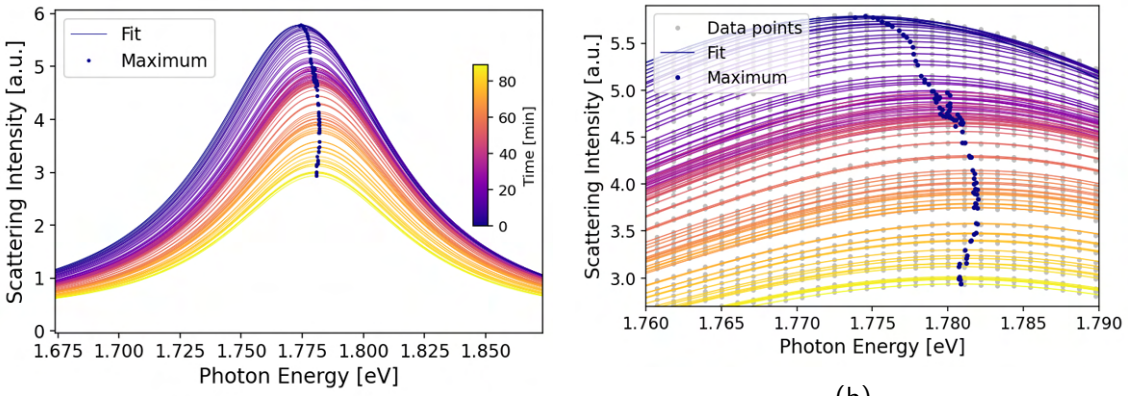

(a) (b)

Figure 5.11: The data were corrected and fitted as discussed in Section 4.1 and 4.2. In this figure the time evolution of data 2 is shown. **a)** The fits of each time step were plotted together with the maximum obtained from the fit as dark blue dot. The time evolution is represented by the colour with the corresponding scalar in minutes displayed by the colour bar. **b)** This detail plot is shows the same data with an increased visibility of the maximum shit. The colour code corresponds to the colour bar in a). In addition to the fits also the real corrected data are shown as underlying grey dots.

As it is shown in Figure 5.11 it was achieved to measure a blue shift of the longitudinal LSPR of single GNRs over time during laser excitation. The colour code corresponds to the time passed since the experiment was started and is equal in both images. Additionally, the maximum is marked with a dark blue dot to highlight the peak shift. However, this effect is small and only hardly visible in the shown images even with the zoom in Figure 5.11b. Therefore it is more beneficial to consider the evolution in time of the pure shift of the LSPR energy instead of the full scattering spectrum.
These shifts can be found in Figure 5.12a. The data are already corrected by the linear focus correction function and plotted together with their corresponding capacitive charging fit and the refocused datapoint. Additionally, the evolution of the FWHMs are shown in Figure 5.12b and 5.12c. The dashed lines highlight the time after which the fitting of the LSPR shift was interrupted. The colour coding for the different datasets is the same in all figures. The FWHM of data 1 is presented separately as it develops in a different direction compared to the FWHMs of the other data. In order to improve the visibility of small broadening or narrowing effects they are plotted using different axes.

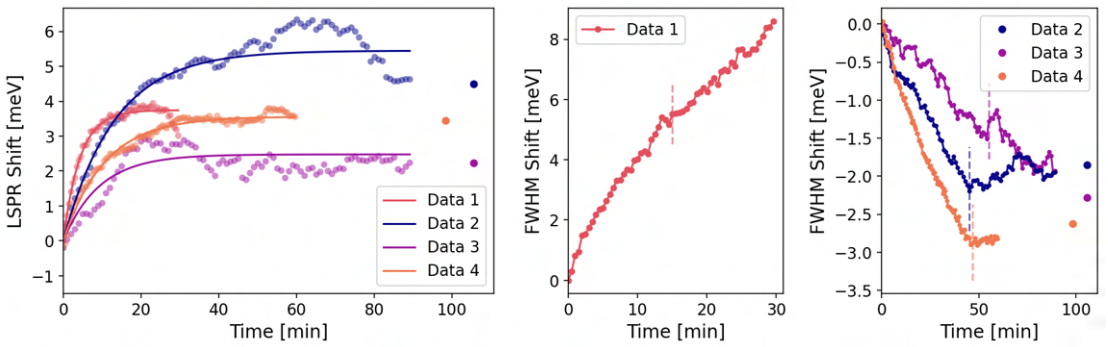

(a) (b) (c)

Figure 5.12: **a)** Observed shift of the LSPR of single GNRs (A12-25-700 on glass). The presented data are corrected by the influence of the focus and plotted together with their capacitive charging fit and the refocused datapoints. **b)** The FWHM shift of data 1 one could not be corrected. **c)** The FWHM sifts of data 2, 3 and 4 were corrected and plotted together with the refocused datapoint. The dashed lines highlight after which time the fitting was interrupted.

All of the shown particles were recorded under different conditions. Therefore, it is reasonable that all of them show a slightly different behaviour.

Discussion Data 1. Data 1 is the only dataset which was recorded on another date and sample than the other measurements. It was irradiated with 480 nm and a power of 0.28 mW. It shows a recognizable capacitive charging behaviour with a saturation at a maximum LSPR shift of approximately 3.7 meV. At the end of the recording a small decrease appears mismatching the expected behaviour. Since the measurement did not last longer and no refocused datapoint was measured at a later time, it cannot be distinguished whether the decrease is only measuring artefact or a consistent behaviour. Although data set 1 indicates a broadening of the FWHM, the lack of a reliable correction procedure hinders a conclusive interpretation of this trend as an intrinsic property of the system.

Discussion Data 2 and 4. Although data 2 and 4 were measured at different wavelengths they behave most similar to one another in both the LSPR energy as well as the FWHM. Both datasets show a clearly identifiable capacitive charging behaviour. Their charging time until they reach a plateau is similar but they saturate at different maximal peak shifts. Data 2 reaches a maximum shift of the LSPR energy of approximately 5.4 meV, while data 4 forms already a plateau for around 3.5 meV. Due to the different excitation wavelengths physical processes contribute to a varying extent. In data 2 the particle was irradiated with light of a wavelength of 480 nm, while data 4 were recorded for an excitation with a wavelength of 520 nm. The number of excited direct interband transitions increases for lower wavelengths and higher photon energy, while a wavelength of 520 nm excites closer to the transversal LSPR at 527 nm. The comparison of data 2 and 4 implies that direct interband transitions are more efficient for generating excited electron-hole pairs than plasmonic absorption and its decay into interband excitations. The FWHM shifts also during the photo-induced charging process. Initially, it narrows

apparently linear for an increasing LSPR shift. Consequently, the number of decay channels decreases. At a certain point the FWHM starts to broaden again but substantially slower and it may stabilize. Parallel to the broadening deviations from the capacitor behaviour appear in the LSPR energy shift. The LSPR rises in both data 2 and data 4 followed by a drop. Afterwards, it appears to stabilize. This effect is much more significant in data 2 than data 4.

Discussion Data 3. Data 3 differs significantly from the other datasets. It is the only measurement, where the observed particle was not located exactly at the centre of the image and consequently, it was not in the centre of the laser beam. The LSPR energy shifts visible to higher energies but does not match the fitted capacitive charging closely. It stabilises at a maximum shift of around 2.5 meV. The corresponding FWHM narrows seemingly linear over time.

Combined Discussion. The theoretical models which were established for ensemble of particles in solution could be successfully reproduced using single particles on a glass substrate, since the same theoretical model for the charging behaviour, which was derived for ensembles, was applied to fit the single particle data [1]. Shifts of the LSPR energy in a similar magnitude were observed.
However, single particle measurements appear to be much more volatile and sensitive to disruptions and noise. Data 3 was not perfectly aligned with the centre of the laser focus and its charging behaviour is less stable and shows much more deviations from the expected trajectory. However, only this single particle was examined at a non centre position, therefore, observations can also be due to artefacts related to this individual particle. Nevertheless, it is recommended to align the GNRs of interest with the laser focus when recording photocharging on single particles. Additionally, due to its displacement the irradiation power was decreased for data 3 resulting in a significantly smaller maximum shift of the LSPR energy compared to data 2 which was recorded in parallel on the same sample but in the centre of the image. A decrease of the maximum charge due to a lower laser power is also supported by considering data 1. It was illuminated with 0.28 mW while for data 2 a power of 0.43 mW was employed. Data 1 saturates already at lower maximum charge than data 2. This is consistent with the behaviour which was observed for ensembles of particles [1]. However, it could not be confirmed, that nanoparticles charge significant slower for a decreased laser power using single particles. Instead, data 1 reaches its maximum charge after the shortest time.
Overall, the single GNRs seem to reach their plateau faster than ensembles with the same maximal shift. This is likely due to the design of the experiment. A single nanoparticle is immobilised on the surface of a substrate therefore it is illuminated for the whole charging time with a continuous power. During the ensemble measurements, the nanoparticles moved freely through the solution and left the laser focus frequently. Thus, several particles were charged at the same time in ensemble experiments, which takes more time compared to the charging of a single particle.
Additionally, to the LSPR energy shifts of single particles, their corresponding FWHM behaviour was determined as well. The FWHM shift of data 1 can not be included in this discussion because we were not able to correct the respective data. When considering the FWHM shifts of the other datasets they all show a narrowing at the beginning but with different rates. The slope is steeper for data 2 and 4 compared to data 3, however, the first two show a broadening after a certain time which does not occur for

data 3. We assume there are different processes contributing to seemingly contradictory behaviour of the FWHM. The narrowing effect for an increased number of accumulated negative charges was already described in literature for a single plasmonic nanoresonator, which was charged via an electric current [61]. This effect was related to nonclassical out-of-plane surface responses of the electrons. Due to repulsion forces between the accumulated charges the electron cloud is pushed out of the centre of the particle. Thus, the interaction of the electrons with the gold lattice is reduced resulting in decreased electron-phonon scattering and less decay of plasmons in inter- and intraband transitions. Consequently, the number of decay channels of the plasmon reduces for an increasing number of charges accumulated on the GNR which is visible as a narrowing of the LSPR [61].
The broadening increases seemingly either over time or with an increasing number of accumulated electrons. The latter is less likely because the intensity of the broadening effect is comparable for data 2 and 4 even though they reach a different maximum charging level. Thus, the broadening is most likely due to a heating of the sample caused by the irradiation with the laser and the tungsten light source. The observed change in the behaviour of the FWHM implies that both mechanisms contribute with a shifting dominance. During the charging process the nonclassical effects increase faster and therefore dominates the observed behaviour at the beginning. When the system saturates the increase of the first effect slows down while the broadening due to heating becomes more significant. This dominance shift appears as a sudden change of the FWHM behaviour. For data 3 the photocharging is less intense and therefore the nonclassical effects increase slower than in data 2 and 4. Thus, both mechanisms apply with a similar contribution already at the beginning. Because they balance each other out, here, the FWHM shift appears as an evenly linear narrowing.

6 Conclusion

Dark-Field Setup. We successfully established a dark-field microscopy setup for the reliable acquisition of single-particle scattering spectra of gold nanorods. This required not only the optimization of the optical setup but also the development of a suitable sample preparation protocol. In particular, the substrates had to be thoroughly cleaned, the particle concentration adjusted to obtain a sparse and homogeneous distribution of single GNRs, and the particles attached on the substrate. Furthermore, the measurement procedure, including secure sample fixation and the optimization of the acquisition parameters, was refined to enable measurements on the single-particle level. By the end it was possible to resolve small peak shifts and changes of the width in the range of sub-millielectronvolt. Thus, the setup is highly suitable to record and detect even slight differences of the LSPR energy caused by changes of the environment or by charge transfer.

Dark-Field and SEM Co-Localization. Furthermore, a technique for rediscovering individual particles using the SEM was developed and improved in such a way that it worked efficiently and reliably for the presented final measurements. It was possible to display particles on all substrates including gold and a sufficient quality was achieved to clearly identify the shape of single nanoparticles.

Contextualisation of the Results. In the first experiment A it was anticipated to observe CID especially on GaN. At a metal-semiconductor interface a major part of CID is expected to proceed via PICT. The observed broadening of the LSPR on GaN is therefore promising as it indicates a direct charge transfer from the GNRs to the substrate, making GaN an attractive material for applications based on charge separation such as photoelectric effects or photocatalysis.
Experiment B was conducted to gain a better understanding of the influence of the electrostatic environment on nanostructures. However, as the effects could not be observed consistently and the origin of any phenomena could not be clearly identified, no conclusions should be drawn and additional research is required to develop research hypotheses.
Experiment C includes both a charge transfer of electrons to the nanoparticle and consequently, a change in the electrostatic interaction with the environment leading to a visible blue shift of the LSPR energy. The elevation of the particle's bandstructure via charging enables to tune it relative to the energetic levels of attached materials. Thus, charge transfer process between the GNR and its environment can be enhanced. By successfully recording the charging effect on single nanoparticles additional insights regarding the evolution of the LSPR width were gained which cannot be measured using ensembles of particles. Even though, the underlying effects could not be completely revealed yet, improving the understanding of the charging effect is essential for enabling its integration into practical applications.

Sample Size. This work is focused on pilot measurements, to gain an idea of which behaviour can be expected, and on proof-of-concept demonstrations. In this regard, the conducted experiments yielded satisfactory results. Nevertheless, all of the phenomena were only investigated for a small sample size. Thus, although trends can be identified conclusions and theoretical considerations should be drawn with care. For the pH value dependency measurements only two datasets were recorded which partially disagree in their behaviour. Due to the lack of additional measurements, it was not possible to confidently identify the reliable dataset. A similar problem appeared for the photocharging measurements. Since it only becomes clear during the analysis which measurements successfully capture the charging effect, the experimental parameters were changed too frequently between measurements and each nanoparticle was recorded under slightly different settings. Therefore, the observed effects cannot be definitively correlated to differences in the settings since the influence of individual variations of the GNRs cannot be excluded. For further investigations it would be beneficial to raise the number of particles measured with the same settings. This way, the significance and reliability of observed phenomena could be increased, while experimental outliers could be identified more reliably. Additionally, statistical evaluations would achieve a higher credibility.

Outlook. The objectives of this work were achieved to a reasonable degree considering the scope of the thesis. A reliable experimental setup was established and a wide range of phenomena were observed. However, further efforts should be exerted to identify the contributing phenomena in greater detail. To this end, an increased sample size is crucial. For time-resolved measurements it would also be useful to include a cooling system or to increase the heat dissipation in order to prevent heating effects of the sample from distorting measurements. Additionally, the reliable recording of scattering spectra of single GNRs with a high intensity is promising for gaining detailed insights about their optical response to various effects. By improving the quality of the electron microscope images up to a level that the dimensions of single particles could be measured individual particles could be simulated using the observed dimensions. Thus, the simulation of the behaviour of a specific nanoparticle could be compared with its dark-field spectra and underlying phenomena can be further revealed. However, the results obtained in this work show promising trends regarding the desired phenomena and highlight the potential of GNRs especially in combination with GaN for photocatalytic applications. Nevertheless, the contributing mechanism are not fully understood yet and require further investigations.

7 Apendix

In the appendix additional images and graphs are shown which were created during the data analysis. Since they supplement mainly the results presented in Section 5 the appendix is organized thematically similar to this chapter. Additionally, in Section 7.1 a short discussion is presented regarding the impact the investigation with a SEM may have on the dark-field scattering spectra.

7.1 Influence of SEM on LSPR Energy and FWHM

The experimental procedure could be simplified by taking the SEM images before recording the dark-field spectra. This way, it could be ensured that only data of single particles were measured and in turn save time. It was therefore investigated at an early stage of the experimental study whether the SEM measurements have an impact on the scattering spectra.

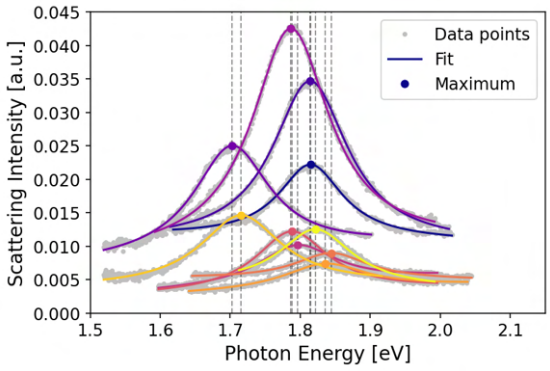

(a) **After 1x SEM** Best Fits

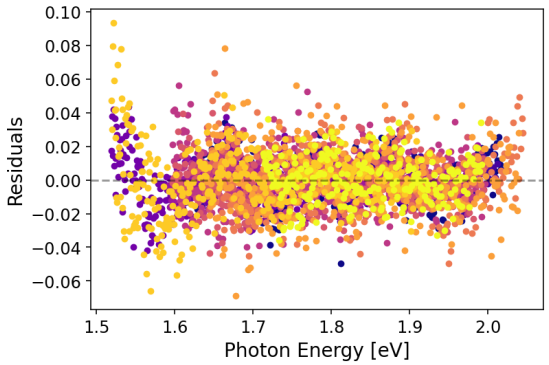

(b) **After 1x SEM** Residuals

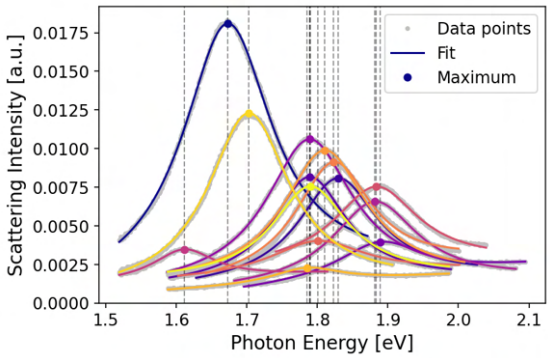

(c) **After 2x SEM** Best Fits

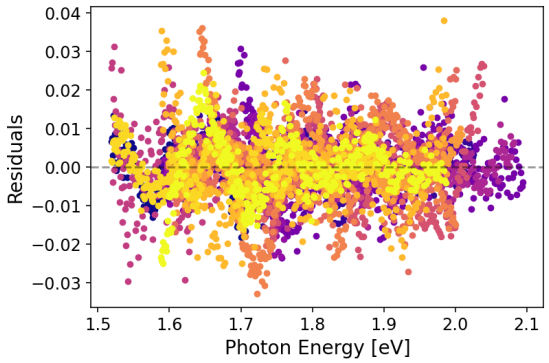

(d) **After 2x SEM** Residuals

Figure 7.1: DH15 on ITO measured after 1x and 2x SEM investigation on the same sample as presented in Section 5.1.2. The data are shown together with their best fits in **a)** after 1x SEM and in **c** after 2x SEM with the corresponding residuals in **b** and **d**.

Throughout this work all mechanism were investigated utilizing the behaviour of the LSPR energy and of the FWHM. Accordingly, these physical quantities were chosen as reference parameters here as well. The measurements were performed with the sample of DH15 GNRs on ITO, which is discussed in Section 5.1.2. The sample was measured three times with dark-field microspectroscopy and after each time it was additionally examined by using the SEM. Some particles were recorded all three times whereas others were only measured once.

In Figure 7.1 the best fits and the corresponding residuals of the datasets "after 1x SEM" and "after 2x SEM" are shown. First, the datasets are going to be discussed as ensembles. Afterwards, the behaviour of individual particles is examined in detail.

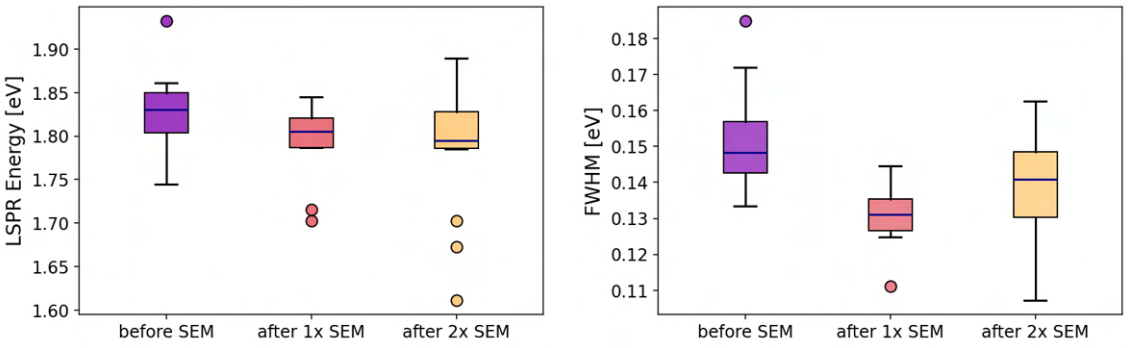

(a) (b)

Figure 7.2: DH15 on ITO before, after 1 1x SEM and after 2x SEM compared regarding the **a** the LSPR energy and **b** the FWHM.

Ensembles. In Figure 7.2 the behaviour of the LSPR energy and FWHM of particles of all three different cases are presented as box plots. When considering the LSPR energy in Figure 7.2a, there are only significant differences between the datasets "before SEM" and "after 1x SEM", which can be identified by the Mann-Whithney U test ($p = 0.084$). Considering the other combinations we can not reject the null hypothesis (with $p > 0.19$). Therefore, the respective null-hypotheses of no significant differences between "before SEM" and "after 2x SEM" and between "after 1x SEM" and "after 2x SEM", need to be maintained Across all three datasets "after 2x SEM" shows the greatest deviations, which partially explains, why it can not be distinguished from both other sets.
When considering the FWHM (Figure 7.2b) there are clear variations visible which can also be confirmed by the Mann-Whitney U test. All corresponding values for p are below the level of 0.1. Therefore, we have to reject the null-hypothesis and assume that all datasets originate from different distributions. The data measured "after 2x SEM" show the strongest variations inside the dataset here as well.

Individual GNRs. Additionally, the evolution of the reference parameters for individual particles was investigated. Eight particles were recorded multiple times, with two particles were only measured twice. Exemplary the scattering spectra of a particle No. 6 for all three cases are shown in Figure 7.3a. Similar graphs for the remaining seven particles can be found at the end of this section in Figure 7.4.
In Figure 7.3b the difference between "before SEM" and "after 1x SEM" (red data), the difference between "before SEM" and "after 2x SEM" (yellow data) as well as the

difference between "after 1x SEM" and "after 2x SEM" (blue data) are shown for each individual particle. If the SEM measurement would have no impact, the plotted datapoints were equal zero. If there were no further change after the first SEM investigation, the blue points were equal zero. The dashed lines connecting the datapoint serve for visualization only and have no physical interpretation.

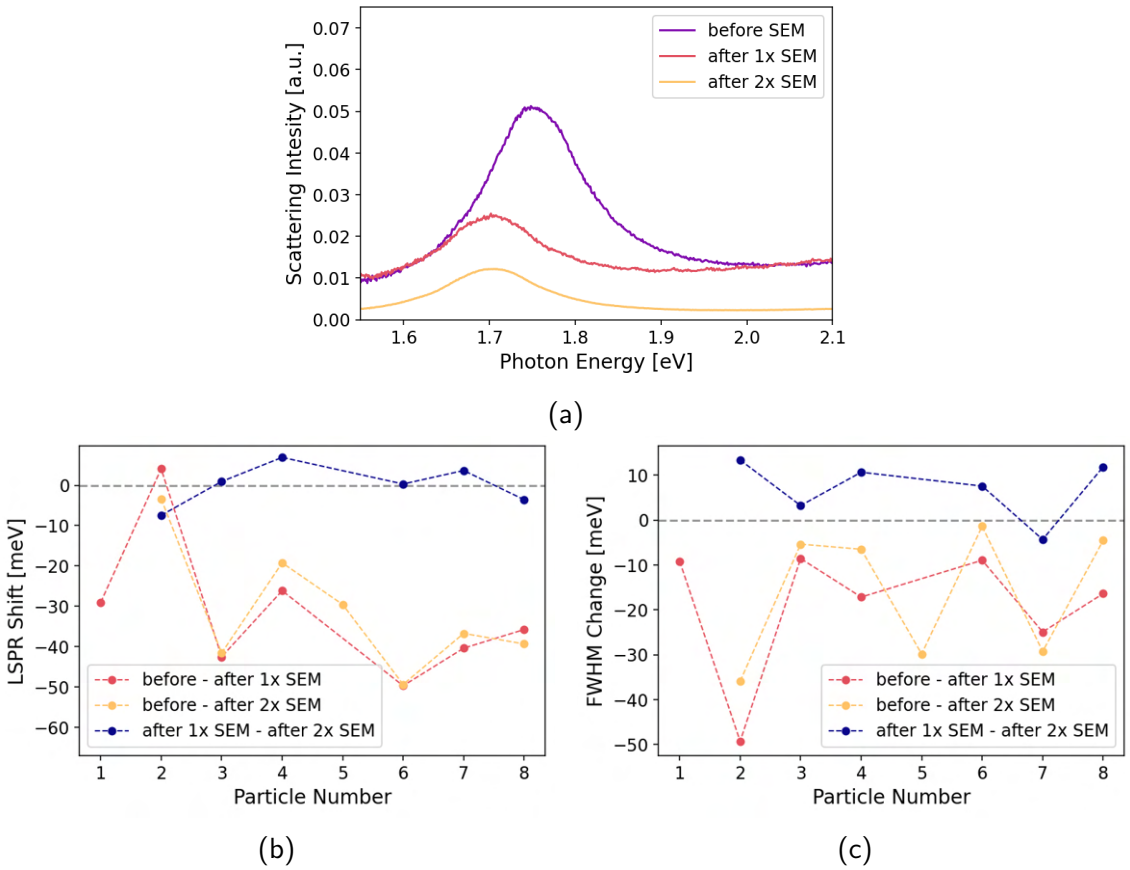

Figure 7.3: **a)** Dark-field scattering spectra of the same particle before (purple line), after 1x (red line) and after 2x (yellow line) observed with the SEM. Exemplarily the data of particle No. 6 are shown. **b)** DH15 on glass and **c)** MS07 on GaN. The dashed lines connecting the data points serve for visualization only and without a physical interpretation.

Differences for both parameters compared to the spectra "before SEM" are recognisable. Since all particles except of one show a red shift of the LSPR after examination with the SEM, a systematic behaviour can be assumed. The visible effect on the FWHM is less intense than the change of the LSPR energy when considering the individual particles. Nevertheless, the FWHM narrows for all particles after the first examination which also suggests a systematic change. After the second examination a slight back shifting is visible for most particles which is in all cases less intense then the initial shift.
Scanning electron microscopy is a highly invasive technique in which the sample is irradiated by a high energy electron beam. A high level of power is exerted on the sample, transferring a large amount of energy. This could cause a variety of changes of the sample such as heating, electrostatic charging which was observed for glass and ITO, degradation, damage via atomic displacement and hydrocarbon contamination [62]. Since the

LSPR is highly sensitive to parameters like the shape of the particle and its coupling to the environment, even small changes could have a significant influence already. The explicit reason was not determined in this work and is only of minor interest to the posed research questions. However, as significant changes were observed caused by the examination with a SEM, the experimental procedure is required to record the scattering spectra before taking SEM images.

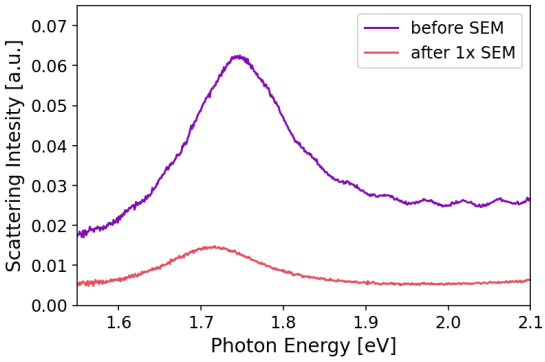

(a) No. 1

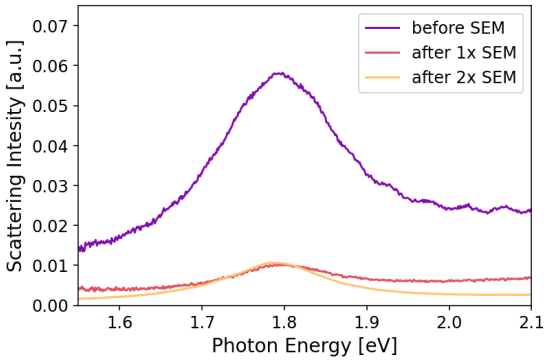

(b) No. 2

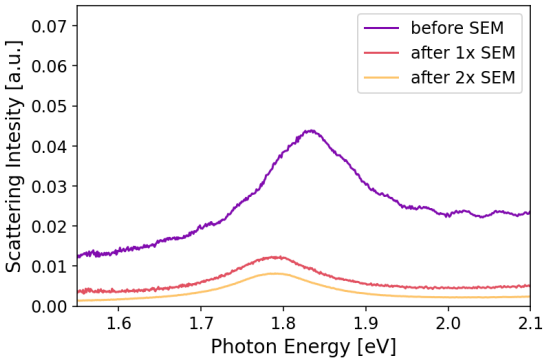

(c) No. 3

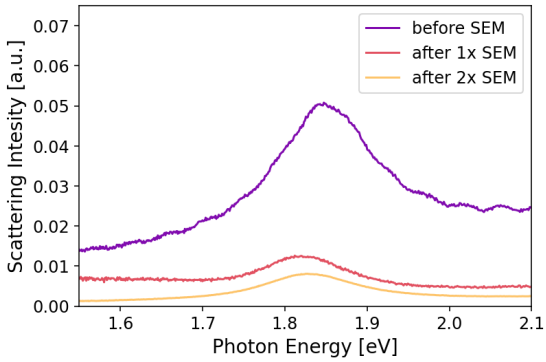

(d) No. 4

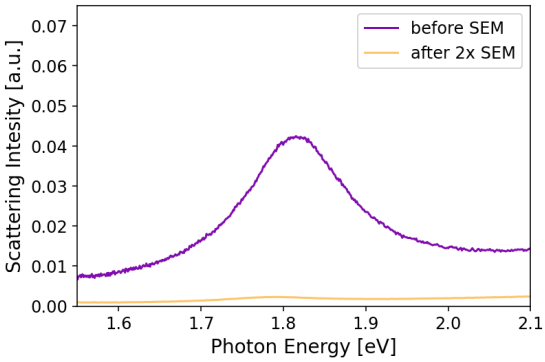

(e) No. 5

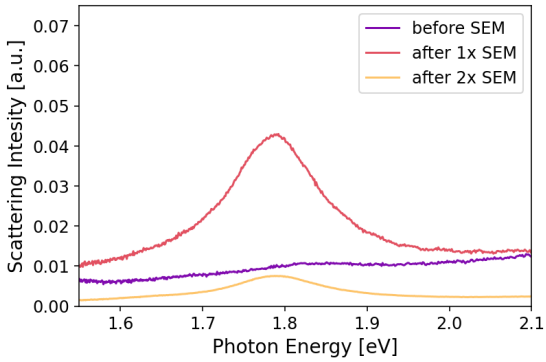

(f) No. 7

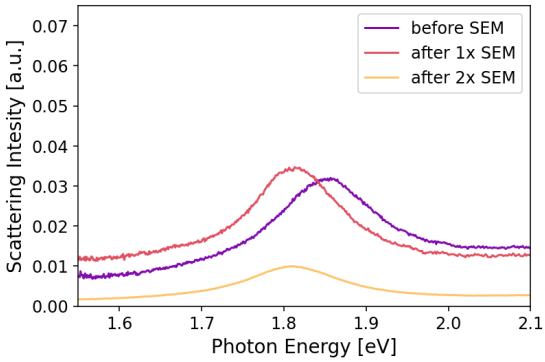

(g) No. 8

Figure 7.4: Individual DH15 particles on ITO, measured before examined with the SEM (purple), after 1x (red) and after 2x (yellow). The particle numbers correspond to the numbers in Figure 7.3b and Figure 7.3c.

7.2 GNRs on GaN

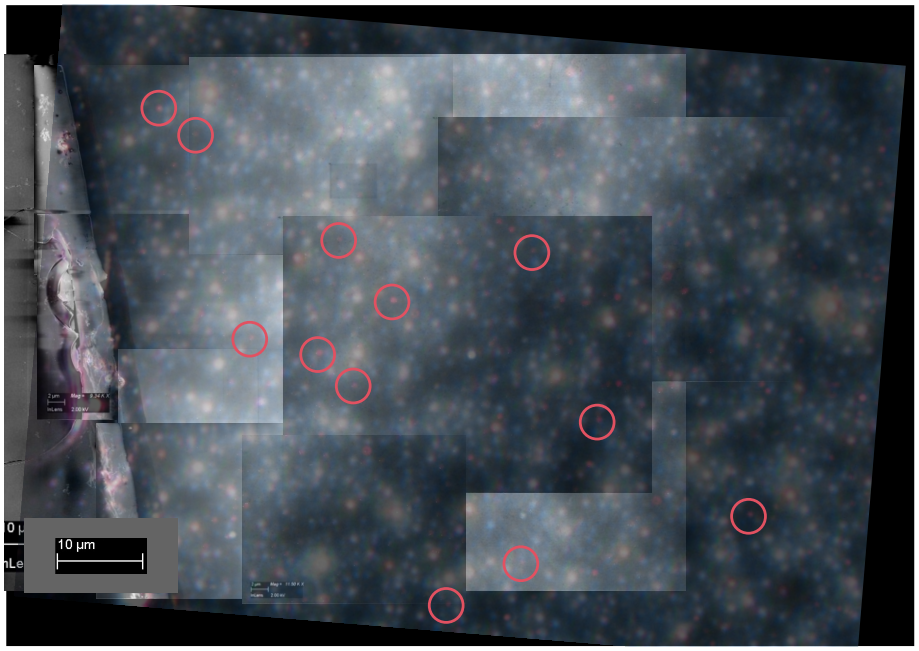

(a)

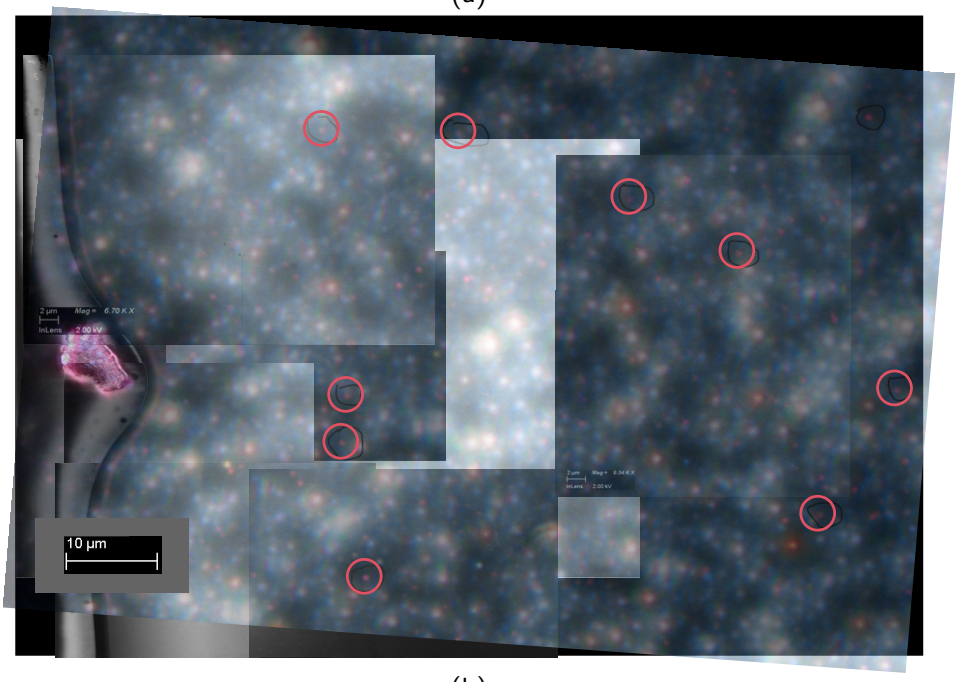

(b)

Figure 7.5: MS07 on GaN: Images of two different spots were the scattering spectra were recorded. The spots are assembled of several SEM images and overlaid by the corresponding dark-field image. The particles measured are highlighted with red circles.

7.3 GNRs at Different pH Values

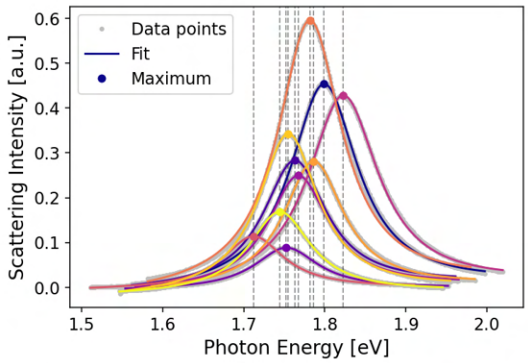

(a) **pH 5.93** Best Fits

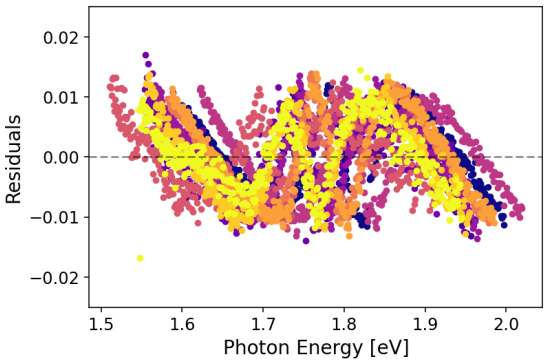

(b) **pH 5.93** Residuals

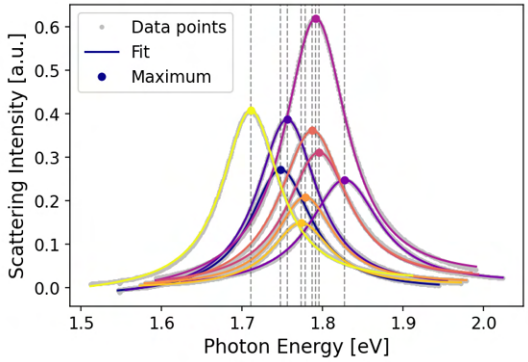

(c) **pH 4.51** Best Fits

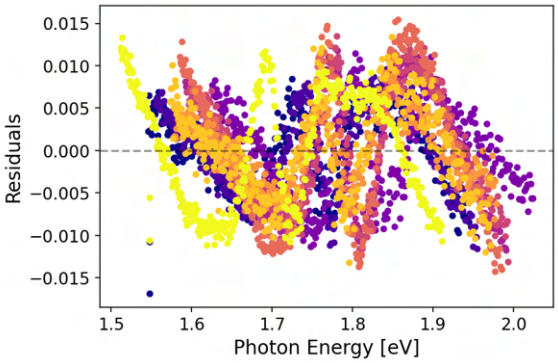

(d) **pH 4.51** Residuals

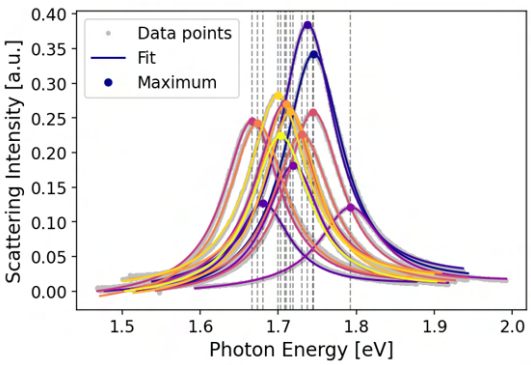

(e) **pH 3.57** Best Fits

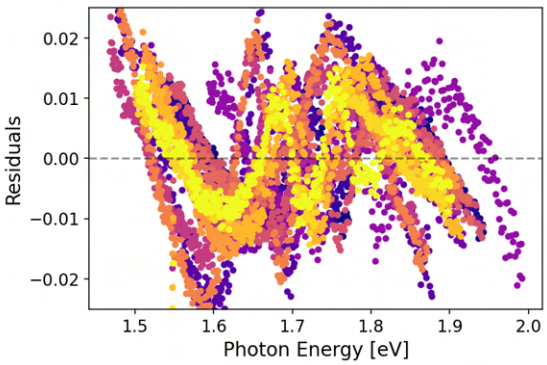

(f) **pH 3.57** Residuals

Figure 7.6: A12-25-700 on glass (dataset 1) measured at different pH values. **a), c), e)** The data are shown together with their best Lorentzian fits and **b), d), f)** the corresponding residuals.

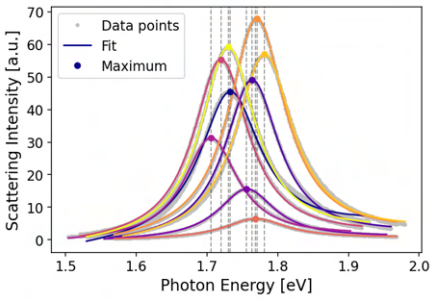

(a) **pH 5.97** Best Fits

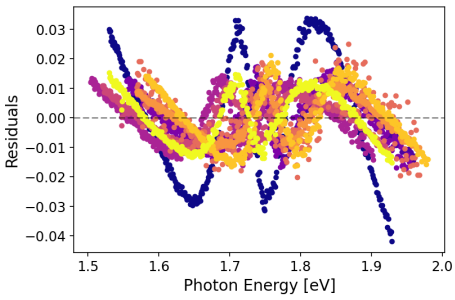

(b) **pH 5.97** Residuals

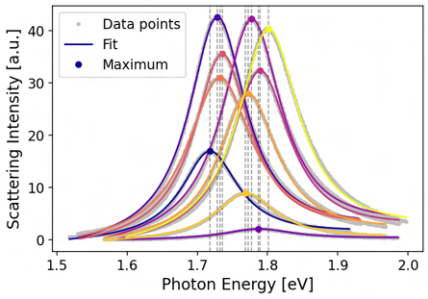

(c) **pH 5.04** Best Fits

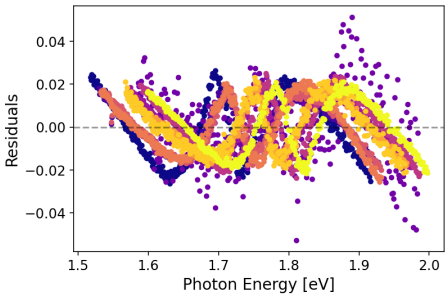

(d) **pH 5.04** Residuals

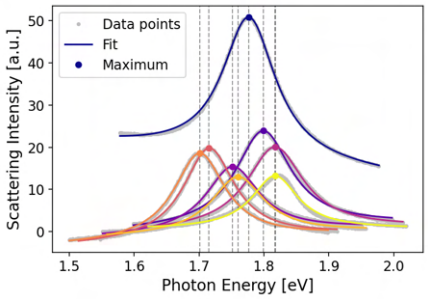

(e) **pH 4.09** Best Fits

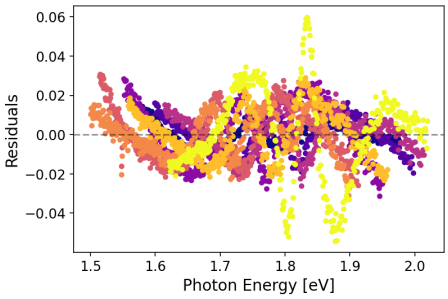

(f) **pH 4.09** Residuals

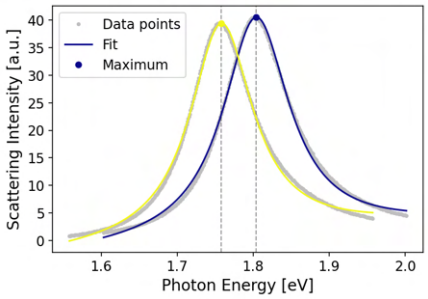

(g) **pH 3.56** Best Fits

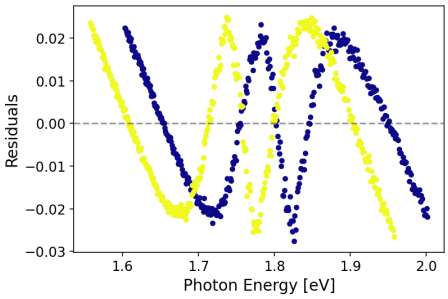

(h) **pH 3.56** Residuals

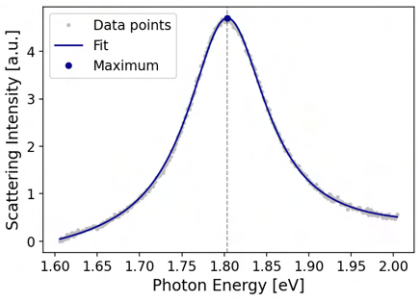

(i) **pH 3.05** Best Fits

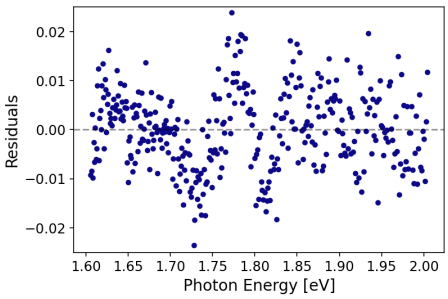

(j) **pH 3.05** Residuals

Figure 7.7: A12-25-700 on glass (dataset 2) measured at different pH values. **a), c), e), g), i)** The data are shown together with their best Lorentzian fits and **b), d), f), h), j)** the corresponding residuals.

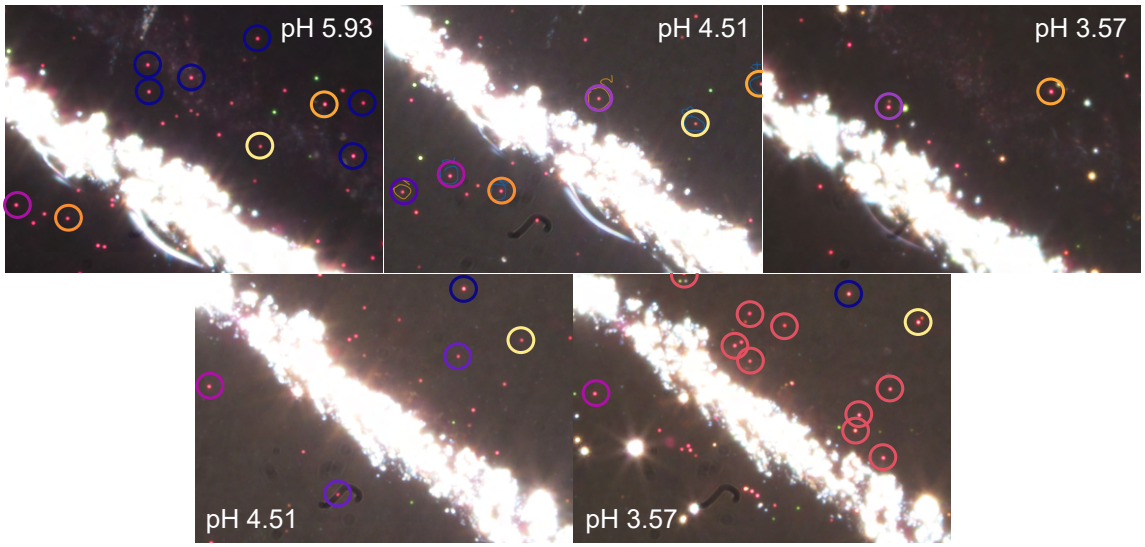

Figure 7.8: The development of two different spots on sample 1 during changing the pH value. Each row corresponds to one spot. All measured particles are marked. Same particles appearing on different images are highlighted with the same colour.

7.4 Photocharging

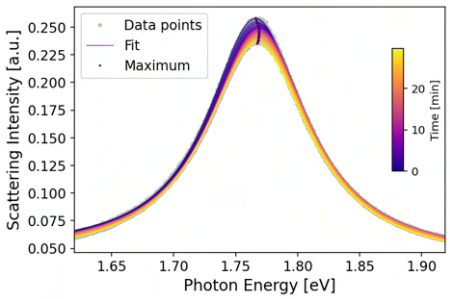

(a) **Data 1** Best Fits

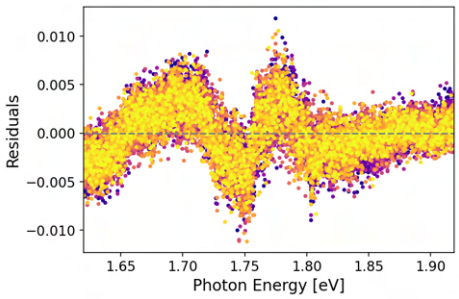

(b) **Data 1** Residuals

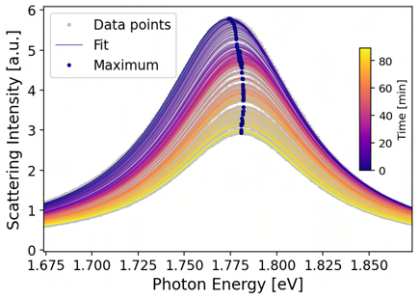

(c) **Data 2** Best Fits

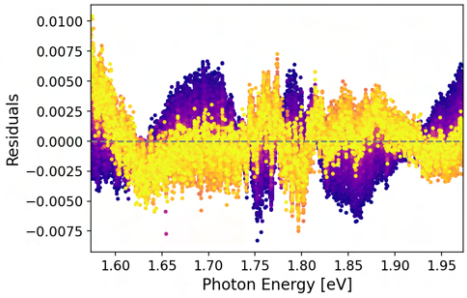

(d) **Data 2** Residuals

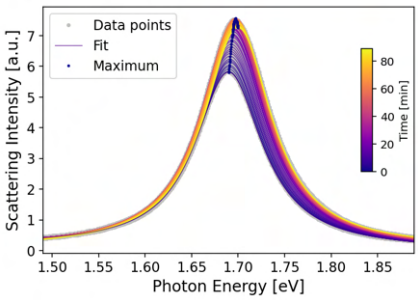

(e) **Data 3** Best Fits

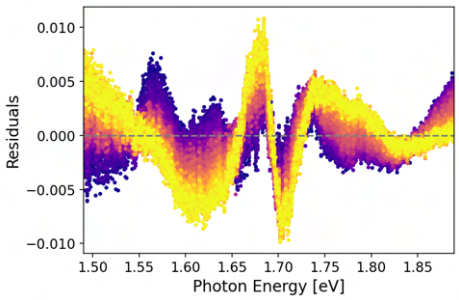

(f) **Data 3** Residuals

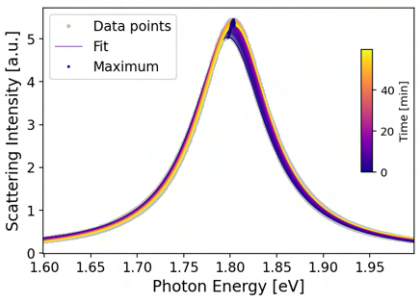

(g) **Data 4** Best Fits

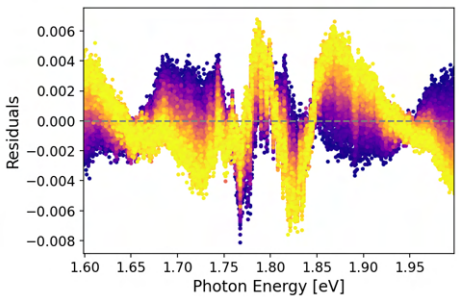

(h) **Data 4** Residuals

Figure 7.9: A12-25-700 on glass for photocharging: **a), c), e), g)** Scattering spectra together with the Lorentz fits and highlighted maximum positions; **b), d), f), h)** corresponding residuals

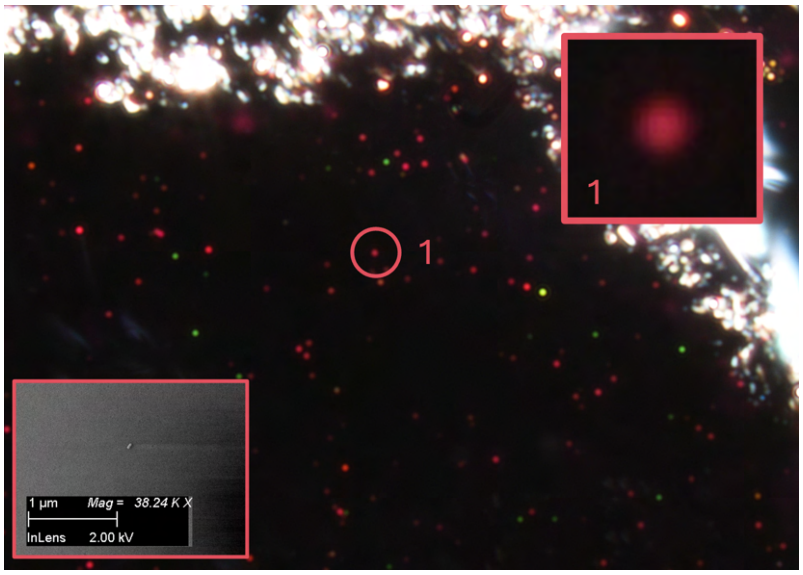

(a) **Particle 1**

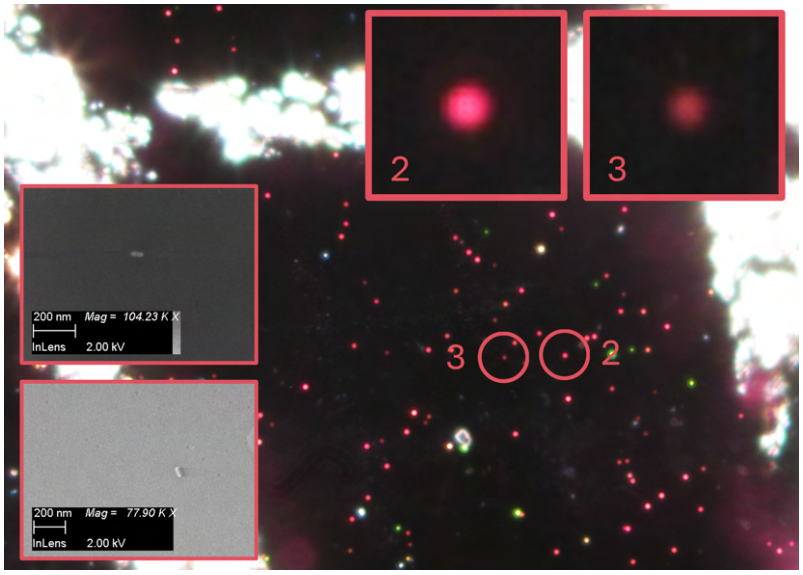

(b) **Particles 2&3**

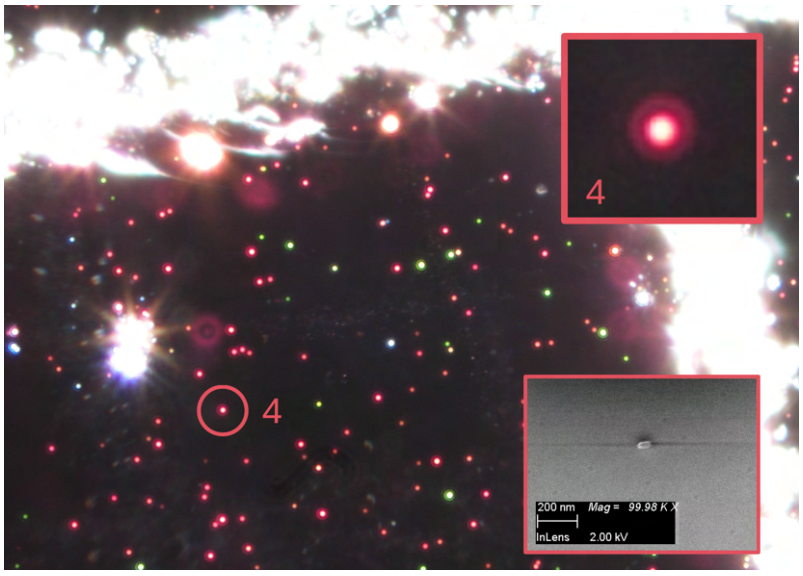

(c) **Particle 4**

Figure 7.10: Dark-field and SEM images of the particles used for photocharging measurements.

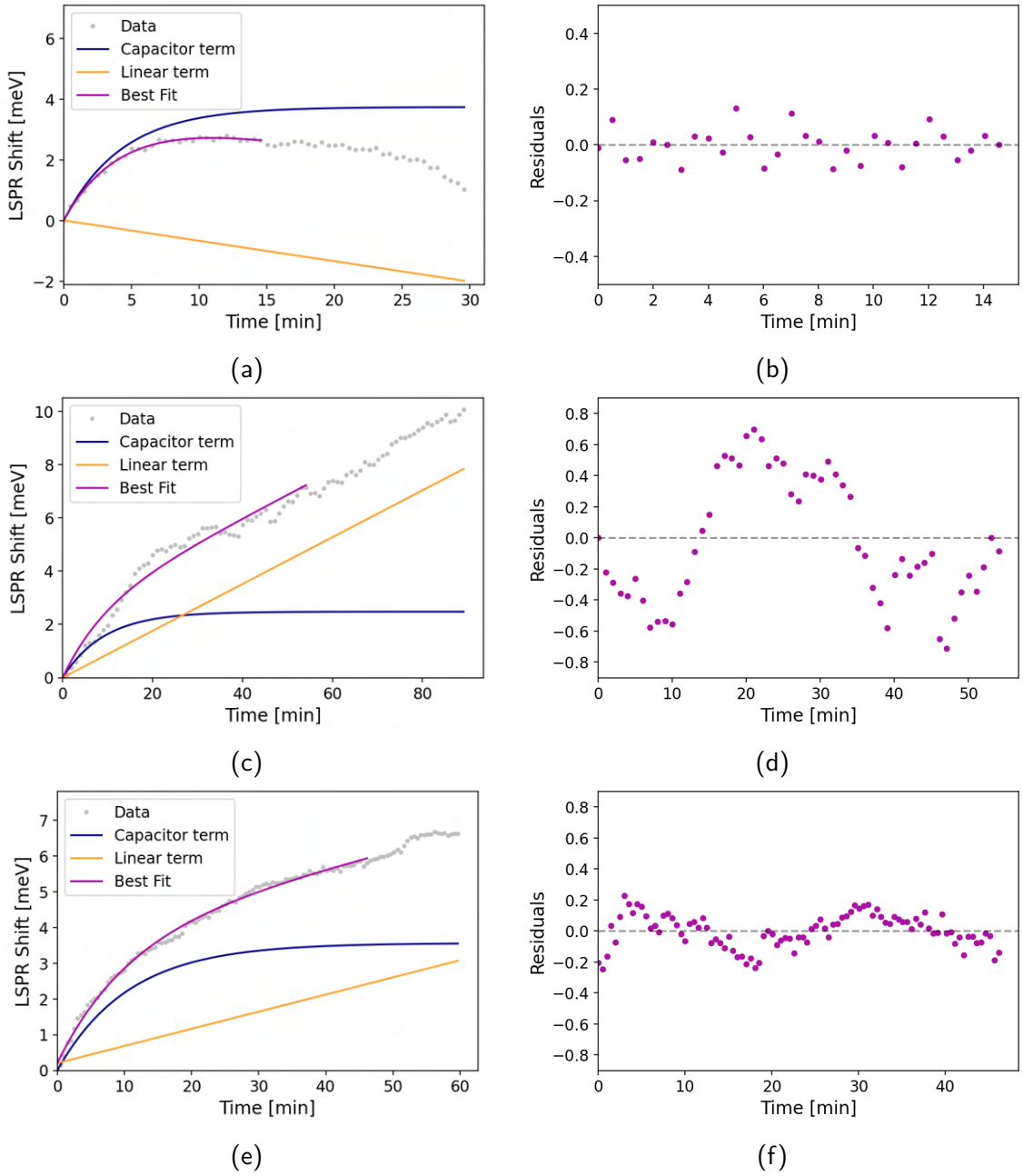

Figure 7.11: **a), c), e)** LSPR energy shifts over time plotted together with the best fits including a linear and a capacitive charging term. **b), d), f)** Corresponding residuals.

Bibliography

[1] Felix Stete, Matias Bargheer, and Wouter Koopman. "Capacitive photocharging of gold nanorods". In: *Nature Communications* (2025).

[2] IPCC. *Climate Change 2023: Synthesis Report. Contribution of Working Groups I, II and III to the Sixth Assessment Report of the Intergovernmental Panel on Climate Change*. Ed. by Core Writing Team, Hoesung Lee, and José Romero. Geneva, Switzerland: Intergovernmental Panel on Climate Change, 2023. DOI: 10.59327/IPCC/AR6-9789291691647.

[3] Suljo Linic, Phillip Christopher, and David B Ingram. "Plasmonic-metal nanostructures for efficient conversion of solar to chemical energy". In: *Nature materials* 10.12 (2011), pp. 911–921.

[4] Phillip Christopher and Martin Moskovits. "Hot charge carrier transmission from plasmonic nanostructures". In: *Annual review of physical chemistry* 68 (2017), pp. 379–398.

[5] Madasamy Thangamuthu et al. "Origin and Promotional Effects of Plasmonics in Photocatalysis". In: *Journal of The Electrochemical Society* 169.3 (2022), p. 036512. DOI: 10.1149/1945-7111/ac5e50.

[6] Phillip Gerald Schoßau. "Dunkelfeldspektroskopie am gekoppelten Plasmon-Exziton-Nanosystem". Arbeitsgruppe Ultrafast Dynamics in Condensed Matter (UDKM). Masterarbeit. Potsdam, Deutschland: Universität Potsdam, 2020. URL: https://www.uni-potsdam.de/fileadmin/projects/udkm/Documents/BaMa_theses/scho2020msc.pdf.

[7] Jana Olson et al. "Optical characterization of single plasmonic nanoparticles". In: *Chemical Society Reviews* 44.1 (2015), pp. 40–57.

[8] Stephen A Lee and Stephan Link. "Chemical interface damping of surface plasmon resonances". In: *Accounts of chemical research* 54.8 (2021), pp. 1950–1960.

[9] Gleb V Petrov et al. "Nanoparticles and nanomaterials: a review from the standpoint of pharmacy and medicine". In: *Pharmaceutics* 17.5 (2025), p. 655.

[10] Lukas Novotny and Bert Hecht. *Principles of Nano-Optics*. 2nd ed. Cambridge University Press, 2012.

[11] Stefan A Maier et al. *Plasmonics: fundamentals and applications*. Vol. 1. Springer, 2007.

[12] Felix Stete. "Photocharging of Single Gold Nanoparticles". Diploma Thesis. Potsdam, Germany: University of Potsdam, 2014. URL: https://www.uni-potsdam.de/fileadmin/projects/udkm/Documents/BaMa_theses/stete2014dipl.pdf.

[13] Wolfgang Demtröder. *Experimentalphysik 2: Elektrizität und Optik*. Springer, 2009.

[14] Neil W Ashcroft, N David Mermin, et al. *Solid state physics*. holt, rinehart and winston, new york London, 1976.

[15] Mildred Dresselhaus et al. "Solid state properties". In: *Alemania: Springer-Verlag* (2018).

[16] Felix Stete. "Gold at the nanoscale: plasmon-exciton coupling and optical heating". PhD thesis. Universität Potsdam, 2020.

[17] John David Jackson and Royce KP Zia. *Classical electrodynamics*. American Institute of Physics, 1977.

[18] Stefan A Maier and Harry A Atwater. "Plasmonics: Localization and guiding of electromagnetic energy in metal/dielectric structures". In: *Journal of applied physics* 98.1 (2005).

[19] Craig F Bohren and Donald R Huffman. *Absorption and scattering of light by small particles*. John Wiley & Sons, 2008.

[20] Aurélien Crut et al. "Optical absorption and scattering spectroscopies of single nano-objects". In: *Chemical Society Reviews* 43.11 (2014), pp. 3921–3956.

[21] Benjamin Foerster et al. "Particle plasmons as dipole antennas: State representation of relative observables". In: *The Journal of Physical Chemistry C* 122.33 (2018), pp. 19116–19123.

[22] H Hövel et al. "Width of cluster plasmon resonances: Bulk dielectric functions and chemical interface damping". In: *Physical Review B* 48.24 (1993), p. 18178.

[23] Carolina Novo et al. "Contributions from radiation damping and surface scattering to the linewidth of the longitudinal plasmon band of gold nanorods: a single particle study". In: *Physical Chemistry Chemical Physics* 8.30 (2006), pp. 3540–3546.

[24] Benjamin Foerster et al. "Plasmon damping depends on the chemical nature of the nanoparticle interface". In: *Science advances* 5.3 (2019), eaav0704.

[25] Peter Zijlstra et al. "Chemical Interface Damping in Single Gold Nanorods and Its Near Elimination by Tip-Specific Functionalization". In: *Angewandte Chemie-International Edition* 51.33 (2012), p. 8352.

[26] Dániel P Szekrényes et al. "Chemical interface damping as an indicator for hexadecyltrimethylammonium bromide replacement by short-chain thiols on gold nanorods". In: *The Journal of Physical Chemistry C* 124.36 (2020), pp. 19736–19742.

[27] Tetsu Tatsuma, Hiroyasu Nishi, and Takuya Ishida. "Plasmon-induced charge separation: chemistry and wide applications". In: *Chemical science* 8.5 (2017), pp. 3325–3337.

[28] Jacob B Khurgin et al. "Direct plasmonic excitation of the hybridized surface states in metal nanoparticles". In: *ACS photonics* 8.7 (2021), pp. 2041–2049.

[29] Fengxia Tong et al. "Photocatalysis on hybrid plasmonic nanomaterials: From catalytic mechanism study at single-particle level to materials design". In: *ACS Catalysis* 14.15 (2024), pp. 11425–11446.

[30] Pedro HC Camargo and Emiliano Cortés. *Plasmonic catalysis: from fundamentals to applications*. John Wiley & Sons, 2021.

[31] Youngsoo Kim, Daniel Dumett Torres, and Prashant K Jain. "Activation energies of plasmonic catalysts". In: *Nano letters* 16.5 (2016), pp. 3399–3407.

[32] Pin Lyu and Son C Nguyen. "Effect of photocharging on catalysis of metallic nanoparticles". In: *The Journal of Physical Chemistry Letters* 12.51 (2021), pp. 12173–12179.

[33] Jenny Schneider et al. "Understanding TiO2 photocatalysis: mechanisms and materials". In: *Chemical reviews* 114.19 (2014), pp. 9919–9986.

[34] Rüdiger Memming. *Semiconductor electrochemistry*. John Wiley & Sons, 2015.

[35] Alexander Al-Zubeidi et al. "Single-particle scattering spectroscopy: fundamentals and applications". In: *Nanophotonics* 10.6 (2021), pp. 1621–1655.

[36] Joseph I Goldstein et al. *Scanning electron microscopy and X-ray microanalysis*. springer, 2017.

[37] Nanopartz Inc. *Bare Gold Nanorods*. 2026. URL: https://www.nanopartz.com/bare_gold_nanorods.asp (visited on 03/11/2026).

[38] Youngsoo Kim, Jeremy G Smith, and Prashant K Jain. "Harvesting multiple electron–hole pairs generated through plasmonic excitation of Au nanoparticles". In: *Nature chemistry* 10.7 (2018), pp. 763–769.

[39] Lu Zhou, Yifeng Jiang, and Dewei Chu. "Synthesis and dielectric properties of printable strontium titanate/polyvinylpyrrolidone nanocomposites". In: *Materials Research Express* 6.9 (2019), p. 0950c6.

[40] Hironori Tsunoyama et al. "Effect of electronic structures of Au clusters stabilized by poly (N-vinyl-2-pyrrolidone) on aerobic oxidation catalysis". In: *Journal of the American Chemical Society* 131.20 (2009), pp. 7086–7093.

[41] Jian Du et al. "Highly transparent and conductive indium tin oxide thin films for solar cells grown by reactive thermal evaporation at low temperature". In: *Applied Physics A* 117.2 (2014), pp. 815–822.

[42] JF Muth et al. "Absorption coefficient, energy gap, exciton binding energy, and recombination lifetime of GaN obtained from transmission measurements". In: *Applied physics letters* 71.18 (1997), pp. 2572–2574.

[43] Mary O'Kane. *UV Ozone Cleaning: Theory and Application*. Ossila. 2024. URL: https://www.ossila.com/pages/uv-ozone-theory (visited on 06/06/2026).

[44] WW Balwanz. "Plasma cleaning of surfaces". In: *Surface Contamination: Genesis, Detection, and Control*. Springer, 1979, pp. 255–269.

[45] Pieter Verding et al. "The influence of UV–ozone, O2 plasma, and CF4 plasma treatment on the droplet-based deposition of diamond nanoparticles". In: *ACS applied materials & interfaces* 16.1 (2023), pp. 1719–1726.

[46] *Hydrophobic Recovery*. ScienceDirect Topics. 2026. URL: https://www.sciencedirect.com/topics/engineering/hydrophobic-recovery (visited on 06/06/2026).

[47] BenchChem Technical Support Team. *An In-depth Technical Guide to the Chelation Mechanism of Citric Acid with Metal Ions*. Online PDF. Accessed: 2026-06-16. 2026. URL: https://www.benchchem.com/product/b115230/docs#an-in-depth-technical-guide-to-the-chelation-mechanism-of-citric-acid-with-metal-ions.

[48] Prof. Dr. J. Gasteiger and S. Spycher. *pH-Wert*. 2001. URL: https://www2.chemie.uni-erlangen.de/projects/vsc/chemie-mediziner-neu/saeuren/ph_wert.html (visited on 06/08/2026).

[49] Universität Kassel. *Scanning Electron Microscope Ultra Plus (Zeiss)*. Institute of Materials Engineering, Department of Mechanical Behavior of Materials. n.d. URL: https://www.uni-kassel.de/maschinenbau/en/institute/institute-of-materials-engineering/departments/mechanical-behavior-of-materials/scientific-equipment/scanning-electron-microscope-ultra-plus-zeiss.html (visited on 07/07/2026).

[50] Niclas S Mueller and Stephanie Reich. "Modeling surface-enhanced spectroscopy with perturbation theory". In: *Frontiers in Chemistry* 7 (2019), p. 470.

[51] Matthew Newville et al. "LMFIT: Non-Linear Least-Square Minimization and Curve-Fitting for Python". In: *Zenodo* (2014). DOI: 10.5281/zenodo.11813.

[52] Regula Forensics. *What is Thin-film Interference?* Document Glossary. n.d. URL: https://regulaforensics.com/glossary/documents/thin-film-interference/ (visited on 07/07/2026).

[53] OpenStax. *3.5: Interference in Thin Films*. 2025. URL: https://phys.libretexts.org/Bookshelves/University_Physics/University_Physics_(OpenStax)/University_Physics_III_-_Optics_and_Modern_Physics_(OpenStax)/03%3A_Interference/3.05%3A_Interference_in_Thin_Films (visited on 06/22/2026).

[54] Harvard Natural Sciences Lecture Demonstrations. *Thin Film Interference*. n.d. URL: https://sciencedemonstrations.fas.harvard.edu/presentations/thin-film-interference (visited on 06/22/2026).

[55] Annette Rudolph, Joachim Krois, and Kai Hartmann. *Kernel smoothing*. Department of Earth Sciences, Freie Universitaet Berlin. 2023. URL: https://www.geo.fu-berlin.de/en/v/soga-py/Advanced-statistics/time-series-analysis/Smoothing/Kernel-smoothing/index.html (visited on 05/18/2026).

[56] Henry B Mann and Donald R Whitney. "On a test of whether one of two random variables is stochastically larger than the other". In: *The annals of mathematical statistics* (1947), pp. 50–60.

[57] Kevin M McPeak et al. "Plasmonic films can easily be better: rules and recipes". In: *ACS photonics* 2.3 (2015), pp. 326–333.

[58] Matplotlib Development Team. *matplotlib.pyplot.boxplot — Matplotlib Stable API documentation*. 2026. URL: https://matplotlib.org/stable/api/_as_gen/matplotlib.pyplot.boxplot.html (visited on 06/01/2026).

[59] Yon-Rui Toh et al. "Induced pH-dependent shift by local surface plasmon resonance in functionalized gold nanorods". In: *Nanoscale research letters* 8.1 (2013), p. 103.

[60] Mao Hamamoto and Hiromasa Yagyu. "Particle size distribution and Au concentration dependence of the refractive-index sensitivity of LSPR sensors based on gold nanoparticles". In: *Journal of Nanoparticle Research* 25.8 (2023), p. 158.

[61] Luka Zurak et al. "Modulation of surface response in a single plasmonic nanoresonator". In: *Science Advances* 10.36 (2024), eadn5227.

[62] Ray F Egerton, Peng Li, and Marek Malac. "Radiation damage in the TEM and SEM". In: *Micron* 35.6 (2004), pp. 399–409.

Eidesstattliche Erklärung

Hiermit versichere ich, dass ich die vorliegende Arbeit ohne Hilfe Dritter und ohne Zuhilfenahme anderer als der angegebenen Quellen und Hilfsmittel angefertigt habe. Alle Stellen der Arbeit, die ich aus diesen Quellen und Hilfsmitteln dem Wortlaut oder dem Sinne nach entnommen habe, sind kenntlich gemacht und im Quellen- und Literaturverzeichnis aufgeführt. Weiterhin versichere ich, dass weder ich noch andere diese Arbeit in der vorliegenden oder einer abgewandelten Form bereits als Leistungsnachweis verwendet haben. Im Rahmen der Arbeit wurde KI-Werkzeuge in Form von OpenAI GPT-5.5 und DeepL als Unterstützung beim Coding, zur Recherche, als Wörterbuch und als unterstützendes Lektorat insbesondere im Abstract und der Introduction verwendet. Ich erkläre, dass ich überprüft habe, dass die mithilfe von KI-Systemen generierten und von mir übernommenen Inhalte faktisch richtig sind. Mir ist bewusst, dass ich als Autorin dieser Arbeit die Verantwortung für die in ihr gemachten Angaben und Aussagen trage.

Markkleeberg, 09.07.2026

Alexandra Faber